LANL Argillite EBS Experimental Program 2014

Fuel Cycle Research & Development

Prepared for
U.S. Department of Energy
Campaign or Program

Florie A. Caporuscio[1], Michael C. Cheshire [1], Michael S. Rearick[1], and Carlos Jove-Colon[2]
[1] Los Alamos National Laboratory,
[2] Sandia National Laboratory

July, 15, 2014

FCRD-UFD-2014-000491
LA-UR-14-25179

SUMMARY

This report addresses the various authigenic minerals occurring within unprocessed Wyoming bentonite, clay/metal interface, clay/host rock reactions during hydrothermal investigations replicating a high temperature repository-like environment. Experiments were pressurized to 150 - 160 bar and were heated following three different temperature profiles: 1) 120°C for 2 weeks, 210°C for 2 weeks, and then 300°C for 1 week, 2) isothermal at 300 °C for 6 weeks and 3) 300°C for 4 months, 210°C for 1 month, and 120°C for 1 month. Unprocessed Wyoming bentonite was saturated with a K-Ca-Na-Cl-rich water at a 9:1 water: rock ratio. Additionally, experiments representing host-rock interaction included Opalinus Clay with associated pore-water chemistry were completed. Mineral alterations associated with cooling experiment yielded similar mineral and geochemical processes observed in the heating and isothermal, 300°C experiments. The pH, K^+, and Ca^{2+} concentrations dropped, while $SiO_{2(aq)}$, Na^+, and SO_4^{2-} concentrations increased throughout the experiments. Illite or illite/smectite was not formed, but significant analcime and silica formation, and pyrite decomposition is observed. Fe-saponite forms at the steel bentonite interface via oxidative leaching of Fe and Ni producing a chromite $(Cr_{1.04},Fe_{0.96})(Fe_{0.69},Ni_{0.31})O_4$ passivation layer on the outer surface of the 316SS plates. Stainless steel corrosion rates are 0.1 $\mu m \cdot d^{-1}$ at 300°C compared to 0.6 $\mu m \cdot d^{-1}$ for low-carbon steel and 0.8 $\mu m \cdot d^{-1}$ for copper. Additionally, no significant retrograde reactions were observed during these reaction conditions.

Many of the chemical reactions observed in the wet system either do not take place or are restricted in the dry system. Pyrite does not undergo decomposition and clinoptilolite undergoes limited dissolution with limited analcime formation. It is evident that reaction kinetics are accelerated under water saturation due to increased ion mobility and minerals' saturation limits.

Alternatively, several mineral alterations were observed in the heating of Opalinus clay. The primary mineral reactions are associated with zeolite formation (i.e., analcime-wairakite, laumontite, and mordenite) at the expense of kaolinite in the host rock. When bentonite is included into Opalinus Clay experiments, the solution chemistry changes significantly forcing the formation of a high-silicon, Ca-enriched analcime. Interpreting clay mineral evolution within Opalinus materials is complicated due to the variety of clay minerals present in the Opalinus experimental systems. However, it does appear that illitization does not occur within the bentonite fraction in the mixed reactions at the current experimental conditions.

CONTENTS

LIST OF FIGURES

LIST OF TABLES

ACRONYMS

CEC - cation exchange capacity
DI – deionized
EBS – Engineered Barrier Systems
EDX – energy dispersive X-ray
EMP - electron microprobe
FY – fiscal year
GW- Giga Watt
IAEA – International Atomic Energy Association
IC - ion chromatography
I-S - illite-smectite
MT – metric ton
NIST –National Institute of Standards and Technology
PWR – pressurized water reactor
SEM - scanning electron microscope
TEM – transmission electron microscope
XRD - X-ray diffraction
XRF - X-ray florescence

LANL Argillite EBS Experimental Program 2014

1. INTRODUCTION

The United States has initiated the Used Fuel Disposition Campaign to evaluate various generic geological repositories for the permanent disposal of used nuclear fuel. The development and evaluation of engineered barrier system (EBS) design concepts and their potential interactions with the natural barrier or with other EBS interfaces are inherently important to the long-term (i.e., tens of thousands of years) safety and performance of geological repositories (Jove-Colon et al. 2011; Nutt et al. 2011). One of the more commonly proposed ideas for high-level nuclear waste repository is to surround waste canisters with bentonite in an underground repository (Pusch 1979; Meunier et al. 1998). There have been numerous investigations on the stability of bentonites under various repository conditions and in contact with various metals replicating possible canister compositions (Pusch 1979; Madsen 1998; Meunier et al. 1998; Guillaume et al. 2003; Wersin et al. 2007; Mosser-Ruck et al. 2010; Ferrage et al. 2011). However, there remain uncertainties regarding the long-term stability of bentonite EBS and corrosion products under potential repository conditions. The focus of this experimental work is to expand our understanding of the stability of bentonite barriers under different geochemical, mineralogical, and engineering conditions than what has been previously investigated. Alteration of smectite to other minerals (i.e., illite, illite/smectite, chlorite), steam-induced swelling loss, and interaction of smectite with metal waste canisters are some of the more prevalent concerns (Couture 1985; Wersin et al. 2007; Mosser-Ruck et al. 2010).

The exact barrier concept has yet to be determined, but the U.S. has considered the possible use of dual purpose canisters for storage and subsequent disposal (Greenburg and Wen 2013). At present, dual purpose canister designs vary greatly, but, in most cases, canisters will be constructed from steel or stainless steel with a steel reinforced concrete overpack (IAEA 2000). In some designs, copper cladding can be added on to the steel canister (Pusch 2008). These canisters can have up to 32 spent fuel assemblies (32 pressurized water reactors or 32-PWR), while many of the European concepts are limited to four spent fuel assemblies (4-PWR) (Pusch 2008; Greenburg and Wen 2013). This increased number of spent fuel assemblies will generate a greater amount of heat radiating into the host rock. High-level modeling suggests a 32-PWR

waste package (at 60 gigawatt-days per metric ton burnup) disposed in a clay/shale host rock, has the potential to reach 299°C after 85 years within 1 meter from the waste package (25 years ventilation; 15 m package spacing; Greenberg and Wen 2013). These results are just one of many models or designs for a U.S. nuclear repository, but, this particular model provides one possible high temperature scenario (Figure 1).

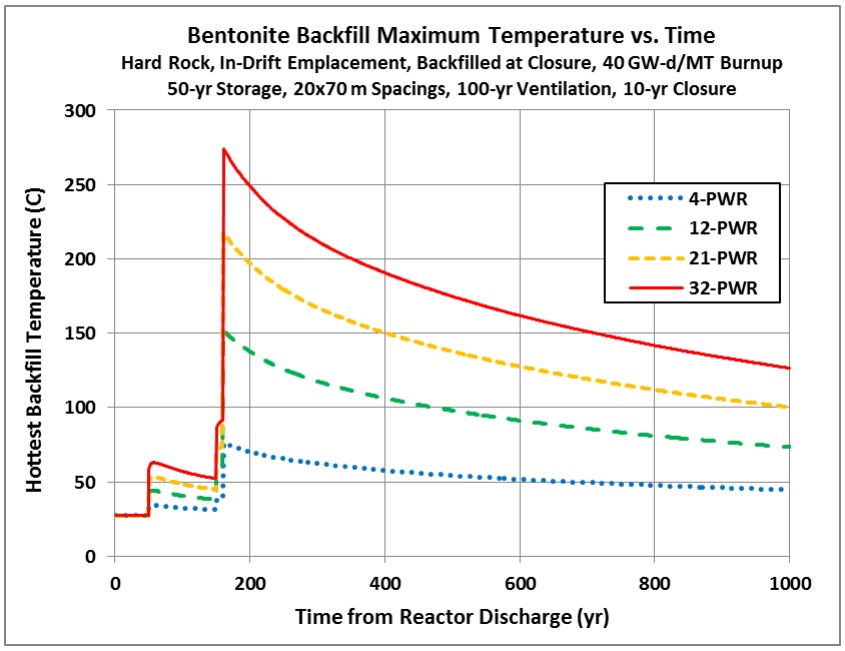

Figure 1. Bounding backfill temperature histories at the waste package surface, for in-drift emplacement in crystalline rock (2.5 W/m-K) with a compacted bentonite backfill (0.6 W/m-K). Backfill rehydration is neglected as a bounding approximation. Waste packages with various capacities are plotted, for fuel with 40 GW-d/MT burnup. For this comparative calculation all packages would be stored at the surface 50 years, then ventilated in the repository 100 years, and finally backfilled over a period of 10 years before permanent closure (personal communication from Ernest Hardin).

One of the more commonly proposed ideas for permanent high-level nuclear waste disposal is to emplace the steel waste canister in a geological repository with a bentonite barrier between the canister and host rock (Pusch 1979; Meunier et al. 1998). Bentonite is used to provide a physical barrier to prevent fluid seeping in from natural surroundings and interacting with the waste package, while acting as a chemical barrier by attenuating actinide migration if a release occurs. Additionally, the bentonite's swelling capacity has the capability of self-sealing if cracks develop within the bentonite due to shrink-swell phenomena. However, there remain

uncertainties regarding the long-term stability of bentonite under potential repository conditions, particularly, under prolonged periods of high thermal loads. There have been numerous investigations on the stability of bentonites under various repository conditions and in contact with various metals replicating possible canister compositions (Pusch 1979; Madsen 1998; Meunier et al. 1998; Guillaume et al. 2003; Wersin et al. 2007; Mosser-Ruck et al. 2010; Ferrage et al. 2011).

This report addresses the various authigenic minerals occurring within unprocessed Wyoming bentonite, clay/metal interface, clay/host rock reactions during hydrothermal investigations replicating a high temperature repository-like environment. Much of the characterization and discussion on the early EBS (1-12) results have been published in Cheshire et al. (2013; 2014a). Further analyses on EBS-1 through -12 have been included to better describe the processes that progress during the hydrothermal reactions. In addition to expanded analyses of the earlier reactions, experiments on host-rock interaction and post-heat cooling were conducted to further our understanding of this complex system.

2. Methods

2.1 Experimental setup

The bentonite used in this experimental work is mined from a reducing horizon in Colony, Wyoming. The bentonite was pulverized and sieved to < 3 mm and used with a free moisture of ~15.5 wt. %. The synthetic groundwater solution was chosen to replicate a deep groundwater composition (Table 1, Stripa sample V2 (69-4), Frape et al. 2003). The groundwater solution was prepared using reagent grade materials dissolved in double deionised water. NaOH and HCl were added to adjust the initial solution pH. This solution was then filtered through a 0.45 μm filter and sparged with He before each experiment. The salt solution was added at 9:1 water: bentonite ratio. Initial components for all experiments have been summarized in Table 3.

A second series of experiments were performed to examine the bentonite system with host rock inclusion. Host-rock experiments focused on Opalinus Clay from the Swiss Underground Research Laboratory located at Mont Terri. The core was collected from BFE-A10 drillcore (interval from 11 to 12 m and interval from 33 to 34 m from the borehole head). A

portion of the Opalinus Clay was crushed and sieved with 10 mesh (~2 mm). Opalinus Clay to be used in experiments was reconstituted at 80 wt.% -10 mesh and 20 wt.% +10 mesh. Synthetic groundwater was chosen to replicate the groundwater composition that represents Opalinus Clay porewater (Table 2, Pearson et al., 2003). The salt solution was added at 9:1 water: rock ratio.

Species	Stripa V2.1 mg/L	Stripa V2.2 mg/L	Stripa V2.3 mg/L	Stripa V2.4 mg/L
Ca^{2+}	93	95	43	61
Cl^{-}	931	455	686	882
K^{+}	583	9	299	559
Na^{+}	171	166	162	201
Si	1	2	2	1
SO_4^{2-}	46	48	31	53
Sr^{2+}	0.05	<0.05	<0.05	0.06
TDS	1863	773	1226	1759
pH	7.35	9.48	6.93	11.2
Experiment Used	EBS 1-5	EBS 6-9	EBS 10-12	EBS 13, 16

Table 1. Synthetic groundwater chemistries used in the hydrothermal experiments. All values were measured at 25°C.

Species	**Type Solution** mg/L	**Actual Solution** mg/L
Ca^{2+}	421	426
Cl^{-}	5672	6470
CO_3^{2-}	162	n.m.
K^{+}	221	225
Na^{+}	3885	3846
Si	5	1
SO_4^{2-}	2305	998
Sr^{2+}	27	0.16
TDS	11502	12153
pH	7.24	7.50
Experiment Used		EBS 14, 15, 17

Table 2. Synthetic groundwater chemistry used in the Opalinus Clay experiments. All values were measured at 25°C. n.m. = not measured

The redox conditions for each system were buffered using a 1:1 mixture (by mass) of Fe_3O_4 and Fe° added at 0.07 wt. % of the bentonite mass. Approximately 7 wt. % (of total solids

mass) 304 stainless steel (NIST SRM 101g), 316 stainless steel (NIST SRM 160b), Cu-foil, and low-carbon steel (provided by Sandia National Laboratory) were added to the experiments to mimic the presence of a waste canister.

Reactants were loaded into either a flexible gold or titanium bag and fixed into a 500 mL Gasket Confined Closure reactor (Seyfried et al. 1987). Experiments were pressurized to 150 - 160 bar and were heated following three different temperature profiles: 1) 120°C for 2 weeks, 210°C for 2 weeks, and then 300°C for 1 week, 2) isothermal at 300 °C for 6 weeks and 3) 300°C for 4 months, 210°C for 1 month, and 120°C for 1 month. Reaction liquids were extracted during the experiments and analyzed to investigate the aqueous geochemical evolution in relationship to mineralogical alterations. The sampled reaction liquids were split three-ways producing aliquots for unfiltered anion, unfiltered cation, and filtered (0.45 μm syringe filter) cation determination. All aliquots were stored in a refrigerator at 1°C until analysis.

2.2 Capsule Experiment Setup

A series of small reactions were run within the pressure media of the major reaction vessels. These reaction series are designed as controls and bounding conditions on the bentonite stability. An advantage of these experiments is that many different geochemical parameters may be tested under the same parent EBS reaction conditions. Reactants listed in Table 4 and 5 were loaded in gold tubes, crimped, and welded shut. Each gold capsule was heated to 105°C for about 1 hour to determine if mass loss occurred. If mass loss was observed, the capsules were not sealed and the setup was repeated until the system was sealed. The sealed capsules were included into the surrounding pressure media for each EBS experiment. Following experiment shut down, each capsule was washed and weighed to determine if they leaked during the experiment. Capsules that did not leak were then cut open and their contents were dispersed in deionized (DI) H_2O and washed 2 – 3 times to remove any soluble salts. Washed samples were then redispersed in DI H_2O and pipetted onto a zero-background quartz plate for X-ray diffraction (XRD) analyses. XRD methods and data interpretations are described below in the XRD methods section below.

	Clay, g	Brine, g	pH	Fe°, g	Fe_3O_4, g	Accessory, g	EBS Component	Run temp, °C	Run time
EBS-1	7.4	79.0	8.59	0.257	0.252	na	na	25/100/200/300/25	4 weeks
EBS-2	7.2	62.0	8.59	0.251	0.253	4.980	304SS	25/100/200/300/25	4 weeks
EBS-3	6.790	59.4	7.56	0.255	0.261	4.245	316SS	25/100/200/300/25	5 weeks
EBS-4	16.207	145.0	7.56	0.574	0.579	9.753	Cu	25/100/200/300/25	5 weeks
EBS-5	15.770	135.9	6.73	0.505	0.505	11.189	304SS	300	6 weeks
EBS-6	12.109	104.2	9.48	0.424	0.424	8.375	Low-C Steel	25/100/200/300/25	5 weeks
EBS-7	14.627	157.9	6.69	0.589	0.586	3.656	Graphite	25/100/200/300/25	5 weeks
EBS-8	15.284	131.9	7.72	0.489	0.489	10.816	Cu	300	6 weeks
EBS-9	15.516	167.6	7.16	0.625	0.625	3.878	Quartz sand	25/100/200/300/25	5 weeks
EBS-10	21.105	182.3	6.36	0.675	0.675	14.937	316SS	300	6 weeks
EBS-11	15.039	129.8	6.74	0.481	0.481	10.643	Cu	300	6 weeks
EBS-12	208.5	41.7	6.74	na	na	na	none	300	7 weeks

	Clay, g	Brine, g	pH	Fe°, g	Fe_3O_4, g	Accessory, g	EBS Component	Run temp, °C	Run time
EBS-13	29.621	245.3	11.0	0.950	0.951	13.304	316 SS	300 to 120	6 months
EBS-16	29.620	248.3	11.2	0.948	0.945	20.936	Cu	300 to 120	6 months

	Clay, g	Brine, g	pH	Fe°, g	Fe_3O_4, g	Accessory, g	EBS Component	Run temp, °C	Run time
EBS-14	14.858	128.1	7.5	0.476	0.476	na	na	300	6 weeks
EBS-15	14.715	158.5	7.6	0.588	0.589	3.679/12.633	Opalinus Clay/316SS	300	6 weeks
EBS-17	14.437	155.2	7.5	0.578	0.575	3.608/12.205	Opalinus Clay/Cu	300	6 weeks

Table 3. Initial components and reaction conditions for EBS experiments. EBS-8 developed a leak during experiment. This experiment was discarded and was repeated as EBS-11.

	Clay, g	Clay Type	Accessory Type	Brine, g	Solution Type	Run temp, °C	Run time	Rxn
CAP-1	0.020	-2 µm, K-Bentonite		0.185	Stripa V2.3 Low-TDS	300	6 weeks	EBS-10
CAP-2	0.020	-2 µm, K-Bentonite		0.220	K-sat Brines	300	6 weeks	EBS-10
CAP-3	0.021	-2 µm, K-Bentonite		0.271	Ca-sat Brines	300	6 weeks	EBS-10
CAP-4	0.019	WY Bentonite		0.186	Stripa V2.3 Low-TDS	300	6 weeks	EBS-10
CAP-5	0.019	WY Bentonite		0.222	K-sat Brines	300	6 weeks	EBS-10
CAP-6	0.018	WY Bentonite		0.276	Ca-sat Brines	300	6 weeks	EBS-10
CAP-11	0.019	-2 µm, K-Bentonite		0.197	K-Al brine	300	6 weeks	EBS-12
CAP-12	0.021	-2 µm, K-Bentonite		0.198	Ca-Al brine	300	6 weeks	EBS-12
CAP-13	0.020	-2 µm, K-Bentonite		0.265	Ca-sat Brines	300	6 weeks	EBS-12
CAP-14	0.018	WY Bentonite		0.199	K-Al brine	300	6 weeks	EBS-12
CAP-15	0.020	WY Bentonite		0.199	Ca-Al brine	300	6 weeks	EBS-12
CAP-16	0.020	WY Bentonite		0.251	K-Al Citric	300	6 weeks	EBS-12
CAP-17	0.020	WY Bentonite		0.254	Ca-Al Citric	300	6 weeks	EBS-12
CAP-18	0.022	-2 µm, K-Bentonite		0.199	Ca-Al brine	300	6 weeks	EBS-12
CAP-19	0.020	WY Bentonite	5% IMt-2 Illite	0.184	Stripa V2.3 Low-TDS	300	6 weeks	EBS-12
CAP-20	0.020	WY Bentonite	15% IMt-2 Illite	0.185	Stripa V2.3 Low-TDS	300	6 weeks	EBS-12
CAP-21	0.020	WY Bentonite	25% IMt-2 Illite	0.185	Stripa V2.3 Low-TDS	300	6 weeks	EBS-12
CAP-22	0.020	WY Bentonite	5% Montana I/S (ISMT)	0.185	Stripa V2.3 Low-TDS	300	6 weeks	EBS-12
CAP-23	0.021	WY Bentonite	15% Montana I/S (ISMT)	0.185	Stripa V2.3 Low-TDS	300	6 weeks	EBS-12
CAP-24	0.020	WY Bentonite	25% Montana I/S (ISMT)	0.215	Stripa V2.3 Low-TDS	300	6 weeks	EBS-12

Table 4. Initial components and reaction conditions for capsule experiments.

	Clay, g	Clay Type	Accessory Type	Brine, g	Solution Type	Run temp, °C	Run time	Rxn
CAP-26	0.020	-2 µm, K-Bentonite		0.234	K-sat Brines	300 to 120	6 months	EBS-13
CAP-27	0.020	-2 µm, K-Bentonite		0.233	K-sat Brines + DI H2O	300 to 120	6 months	EBS-13
CAP-28	0.020	-2 µm, K-Bentonite		0.227	Ca-sat Brines	300 to 120	6 months	EBS-13
CAP-29	0.020	-2 µm, K-Bentonite		0.243	Ca-sat Brines + DI H2O	300 to 120	6 months	EBS-13
CAP-31	0.020	WY Bentonite		0.233	K-sat Brines	300 to 120	6 months	EBS-13
CAP-32	0.021	WY Bentonite		0.233	K-sat Brines + DI H2O	300 to 120	6 months	EBS-13
CAP-33	0.021	WY Bentonite		0.282	Ca-sat Brines	300 to 120	6 months	EBS-13
CAP-34	0.021	WY Bentonite		0.212	Ca-sat Brines + DI H2O	300 to 120	6 months	EBS-13
CAP-36	0.021	-2 µm, Ca-Bentonite		0.232	K-sat Brines	300 to 120	6 months	EBS-13
CAP-37	0.021	-2 µm, Ca-Bentonite		0.234	K-sat Brines + DI H2O	300 to 120	6 months	EBS-13
CAP-38	0.021	-2 µm, Ca-Bentonite		0.275	Ca-sat Brines	300 to 120	6 months	EBS-13
CAP-39	0.021	-2 µm, Ca-Bentonite		0.229	Ca-sat Brines + DI H2O	300 to 120	6 months	EBS-13
CAP-40	0.020	-2 µm, Bentonite	10% K-feldspar	0.185	Stripa V2.4 Low-TDS	300	6 weeks	EBS-15
CAP-41	0.020	-2 µm, Bentonite	20% K-feldspar	0.187	Stripa V2.4 Low-TDS	300	6 weeks	EBS-15
CAP-42	0.019	-2 µm, Bentonite	10% albite	0.186	Stripa V2.4 Low-TDS	300	6 weeks	EBS-15
CAP-43	0.020	-2 µm, Bentonite	20% albite	0.187	Stripa V2.4 Low-TDS	300	6 weeks	EBS-15
CAP-44	0.021	-2 µm, Bentonite	10% muscovite	0.189	Stripa V2.4 Low-TDS	300	6 weeks	EBS-15
CAP-45	0.020	-2 µm, Bentonite	20% muscovite	0.188	Stripa V2.4 Low-TDS	300	6 weeks	EBS-15
CAP-46	0.020	-2 µm, Bentonite	10% Grimsel granite	0.189	Stripa V2.4 Low-TDS	300	6 weeks	EBS-15
CAP-47	0.021	-2 µm, Bentonite	20% Grimsel granite	0.189	Stripa V2.4 Low-TDS	300	6 weeks	EBS-15
CAP-48	0.022	-2 µm, Bentonite	30% Grimsel granite	0.188	Stripa V2.4 Low-TDS	300	6 weeks	EBS-15

Table 5. Initial components and reaction conditions for capsule experiments

2.3 Mineral analyses

X-ray diffraction (XRD) analyses of experimental materials determined mineral compositions. Each sample was ground with 20 wt. % corundum (Al_2O_3) for quantitative XRD analysis of the bulk rock (Chung 1974). XRD measurements were conducted with a Siemens D500 diffractometer using Cu-Kα radiation. Data were collected from 2 to 70 °2θ with a 0.02 º2θ step-size and count times of 8 to 12 seconds per step. To better analyze the non-clay and clay fractions, the < 2 μm particles were separated via sedimentation in DI H_2O. An aliquot of the < 2 μm suspension was dropped on a zero-background quartz plate and dried. This oriented mount was X-rayed from 2 to 40 °2θ at 8 to 12 s per step. The oriented mount was then saturated with ethylene glycol in a 60 °C oven for 24 hours and XRD analysis was repeated. A portion of the > 2 μm particles was ground with a mortar/pestle, deposited on a zero-background quartz plate, and X-rayed under the same parameters as the bulk powder material. The remaining > 2 μm portion was used for electron microscopy. Mineral identification and unit-cell parameters analysis was performed using Jade© 9.5 X-ray data evaluation program with ICDD PDF-4 database. Quantitative phase analysis was performed using FULLPAT (Chipera and Bish 2002). Illite-smectite composition of higher-ordered (R1-3) illite-smectites were modeled via ClayStrat+ (developed by Hongji Yuan and David Bish). Expandable component abundances for the disordered illite-smectites were calculated via the Δ°2Θ method (Środoń 1980; Eberl et al. 1993; Moore and Reynolds 1997). A regression from calculated data were used to calculate the % expandable (%Exp) component in each untreated and reacted bentonite. The equations are:

$$\%Exp = 973.76 - 323.45\Delta + 38.43\Delta^2 - 1.62\Delta^3$$ (Eberl et al. 1993, Eq. 3, R^2=0.99),

with Δ corresponding to Δ°2Θ between the 002 and 003 peak positions for the oriented, ethylene glycol saturated samples.

X-ray florescence (XRF) analysis of the experimental materials was performed using a Rigaku ZSX Primus II. Samples were mixed with Li-metaborate at 36:1 and fluxed at 1100° C for 45 minutes. All reported values exceed three times the reported detection limits. Loss on ignition (LOI) was determined by heating the sample to 1000°C for 30 minutes.

Analytical electron microscopy was performed using a FEI™ Inspect F scanning electron microscope (SEM). All samples were Au/Pd-coated prior to SEM analysis. Imaging with the

SEM was performed using a 5.0 kV accelerating voltage and 1.5 spot size. Energy dispersive X-ray spectroscopy (EDX) was performed at 30 kV and a 3.0 spot size.

Electron microprobe (EMP) analyses were performed at the University of Oklahoma using a Cameca SX50 electron microprobe equipped with five wavelength-dispersive spectrometers and PGT PRISM 2000 energy-dispersive X-ray detector. Petrographic characterization was performed by backscattered electron imaging coupled with energy-dispersive X-ray analysis, using beam conditions of 20 kV acceleration and 20 nA sample current. Quantitative analysis was performed by wavelength-dispersive spectrometry using 20 kV accelerating voltage, 20 nA beam current, and 2 μm spot size. Matrix corrections employed the PAP algorithm (Pouchou and Pichoir 1985), with oxygen content calculated by stoichiometry. Counting times were 30 seconds on peak for all elements, yielding minimum levels of detection (calculated at 3-σ above mean background) in the range of 0.01 to 0.03 wt. % of the oxides for all components except F (0.16 wt. %). All standards for elements in the silicates were analyzed using 30 second count times on peak, using K-alpha emissions. The standards and oxide detection limits are presented in Appendix A, with analytical data presented in Appendix B.

Cation exchange capacity (CEC) determinations followed methods described by Busenberg and Clemency (1973). The < 2 μm fraction used in the XRD analyses was saturated with 1N ammonium acetate overnight. After which, samples were then washed with a 1N NH_4Cl solution followed with multiple DI H_2O/methanol rinses until chloride was not detected with a few drops of a 1N $AgNO_3$ solution. Each sample was air-dried and powered for CEC analyses. Prior to CEC measurements, an ammonia-mV calibration curve was developed for the ammonia probe with 10^{-2}, 10^{-3}, 10^{-4} and 10^{-5} M standard NH_4^+ solutions (Figure 2).

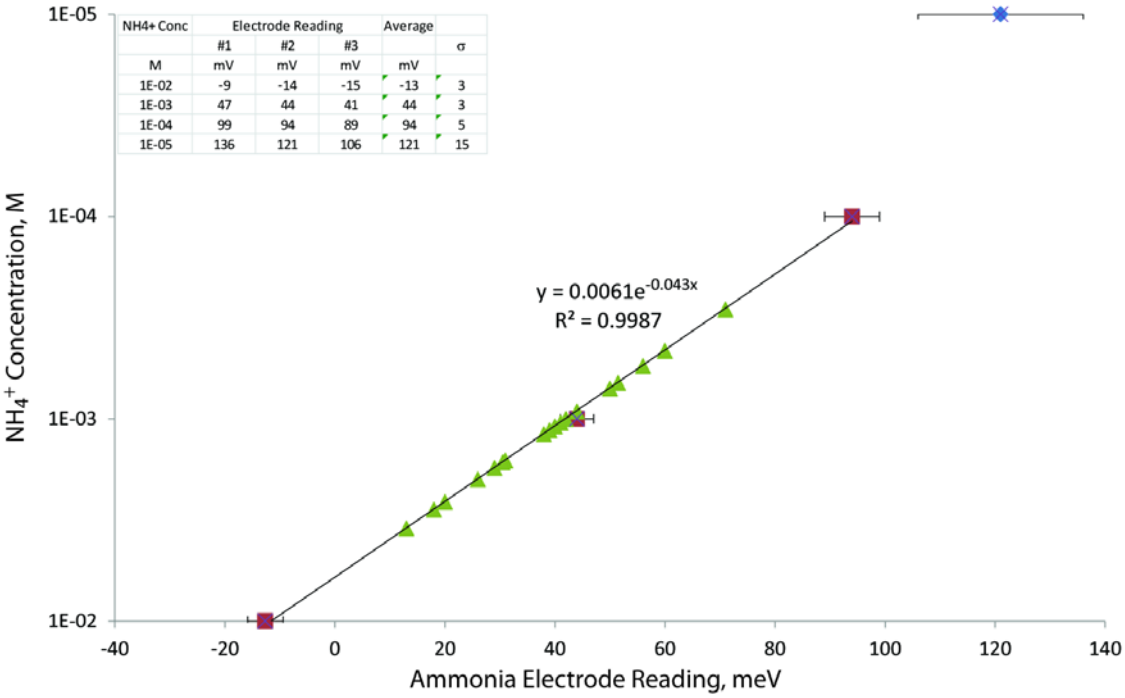

Figure 2. Ammonia-mV calibration curved of an ammonia electrode used for the CEC calculations. Red square data points were used to develop the calibration curve for each sample analysis (green triangles). All sample data points fall within the calibration boundaries.

20 – 200 mg of each NH_4-exchanged sample was dispersed in 50 ml DDI H_2O and constantly stirred with the ammonia electrode inserted into the suspension. Exactly 0.5 ml of 10M NaOH was added to the stirring suspension. Electrode readings were collected upon stabilization of the mV reading. CEC values were then calculated from the following equation:

$$CEC = \frac{(c)(v)}{(w)(f)}$$

where, CEC is cation exchange capacity of sample in mEq/100g of clay, c is concentration of ammonia in M, v is volume of water added, w is mass of sample (mg), f is a conversion factor of 10^{-5}.

To better determine the expandability of the post-reacted montmorillonites, the < 2 µm fractions were separately cation exchanged with Li^+, K^+, and Ca^{2+}. Each of these cations has differing hydration energies and charge densities. These exchanges should show subtle changes

to the layer charge of the montmorillonite upon expansion with ethylene glycol due to the Coulombic interaction between the competing cation-layer attractive forces and interlayer cation hydration energies. About 0.5 g of < 2 μm fraction from starting bentonite and the post reacted bentonite were repetitively washed in 250 ml of 2 M LiCl, 2M KCl, and 1M $CaCl_2$. Following the salt washed, the cation exchanged materials were then washed in DI H_2O/ethanol until chloride was no longer detected with a few drops of a 1N $AgNO_3$ solution. Each sample was then redispersed in DI H_2O and pipetted onto a zero-background quartz plate for XRD analyses. Each cation-exchanged samples was then ethylene glycol saturated to expand the expandable layers and X-rayed. Expandability of each sample was then calculated via ClayStrat+.

2.4 Aqueous geochemical analyses

Major cations and trace metals were analyzed via inductively coupled plasma-optical emission spectrometry (Perkin Elmer Optima 2100 DV) and inductively coupled plasma-mass spectrometry (Elan 6100) utilizing EPA methods 200.7 and 200.8. Ultra-high purity nitric acid was used in sample and calibration preparation prior to sample analysis. Internal standards (Sc, Ge, Bi, and In) were added to samples and standards to correct for matrix effects. Standard Reference Material (SRM) 1643e Trace Elements in Water was used to check the accuracy of the multi-element calibrations. Inorganic anion samples were analyzed by ion chromatography (IC) following EPA method 300 on a Dionex DX-600 system. Aqueous geochemical results are presented in Appendix C.

3. Results

3.1 Analyses performed on samples from FY'12-FY'13

Electron microprobe chemical analyses for silicate constituents from EBS experiments are presented in Appendix B; Tables B1 to B7.

Cation exchange capacity determination was performed on the < 2 µm fraction of EBS-1 through EBS-11, in addition to the starting bentonite. The < 2 µm fraction was determined to be predominantly montmorillonite with minor amounts of opal-CT. Results are summarized in Table 6. There appears to be no significant CEC alteration of treated clays compared to the starting montmorillonite. This is a key parameter in understanding changes in layer charge associated with montmorillonite alteration. Increases in layer charge typically are associated with an increase in CEC to the point when Coulombic attraction dominates over swelling pressure and irreversible collapse occurs lowering the CEC values (based on these methods).

A select number of samples were chosen for cation exchange to quantify post-reacted montmorillonite's expandability. Results are summarized in Table 7. Samples labeled as a Na-exchanged montmorillonite are reaction products without further exchange treatments. Reaction products typically are Na-based montmorillonite, but can have non-trivial amounts of K^+ and Ca^{2+} in the interlayer. Expandability data are consistent with reaction products' CEC values showing no significant alteration to the starting montmorillonite's layer charge.

Interlayer Cation	$\Delta G_{hydration}$ kJ mol^{-1}	% Expandable			
		Bentonite	Ramped	Isothermal	"Dry"
K^+	-337	93	94	96	~*93*
Na^+	-411	100	100	100	100
Li^+	-511	n.d.	98	100	100
Ca^{2+}	-1593	98	96	98	n.d.

Table 6. Expandability from cation-exchanged starting and post-reacted montmorillonite. Hydration energies were from Burgess (1978).

	#1				#2					
	Mass *Mg*	**Reading** *eV*	**NH_4^+ conc** *M*	**CEC** *meq/100g*	**Mass** *mg*	**Reading** *eV*	**NH_4^+ conc** *M*	**CEC** *meq/100g*	**Average CEC** *meq/100g*	**σ**
Bentonite	78	40	0.0011	**70**	168	20	0.002581	**77**	**73**	5
EBS-1	21	71	0.0003	**69**					**69**	
EBS-2	52	51.5	0.0007	**64**					**64**	
EBS-3	145	26	0.0020	**69**	111	30.5	0.0016	**74**	**71**	4
EBS-4	79	41	0.0010	**66**	223	13	0.0035	**78**	**72**	8
EBS-6	127	31	0.0016	**63**	180	20	0.0026	**72**	**68**	6
EBS-7	88	38	0.0012	**68**	70	42	0.0010	**72**	**70**	3
EBS-9	71	44	0.0009	**65**	75	39	0.0011	**76**	**70**	8
EBS-5	129	29	0.0018	**68**	189	18	0.0028	**74**	**71**	5
EBS-10	53	50	0.0007	**67**	37	56	0.0006	**74**	**71**	5
EBS-11	33	60	0.0005	**70**					**70**	

Table 7. CEC from the < 2 μm fraction of the starting bentonite and EBS reaction products. Some samples were run in duplicate.

3.2 "Dry" Bentonite Experiment – EBS-12

Various mineral alterations and textural developments occurred during the water limited experiment of EBS-12 that is significantly different from the fluid dominated experiments. Bentonite compaction produced significant foliation of the montmorillonite particles (Figure 3A). Montmorillonite developed rough edges during the long-term cooling experiments due to what appears to be a partial dissolution, but maintained the typical foily smectite morphology (Figure 3A and B). Additionally, glycol saturated samples yielded d_{001} of 17 Å with higher order $d_{00\ell}$ consistent with integer values of the d_{001} values, suggesting the montmorillonite did not undergo extensive illitization.

Analcime and cristobalite were produced as a result of a partial dissolution/alteration of clinoptilolite and remnant volcanic glass. Clinoptilolite did not undergo complete dissolution yielding clinoptilolite with dissolution features (Figure 3C). Analcime occurs as 5 to 10 μm deformed spheres and cubes primarily from the agglomeration of nanometer-sized analcime particles (Figure 3D and E). Analcime morphology does indicate impeded growth due to the solids-dominated system forcing deformed crystal growth. Previous EBS experiments (i.e., w/r

9:1) displayed analcime with subhedral to euhedral trapezohedrons (Cheshire et al. 2013; 2014a). Growth of analcime appears to have been stopped due to the quenching of the reaction preserving the various stages of analcime ripening.

Silica precipitation was observed primarily as opal-CT or cristobalite forming spherical aggregates along the edges of the montmorillonite particles (Figure 3F). It is difficult to determine if the silica precipitation occurred during the heating phase or the quenching phase as solution chemistry was not able to be monitored during the experiment.

Pyrite did not appear to undergo decomposition or dissolution, with original cubic morphology was (Figure 3B). Much of the pyrite preservation might be due to the water limited environment, thereby restricting pyrite solubility. There is no evidence of other sulfide or sulfate formation.

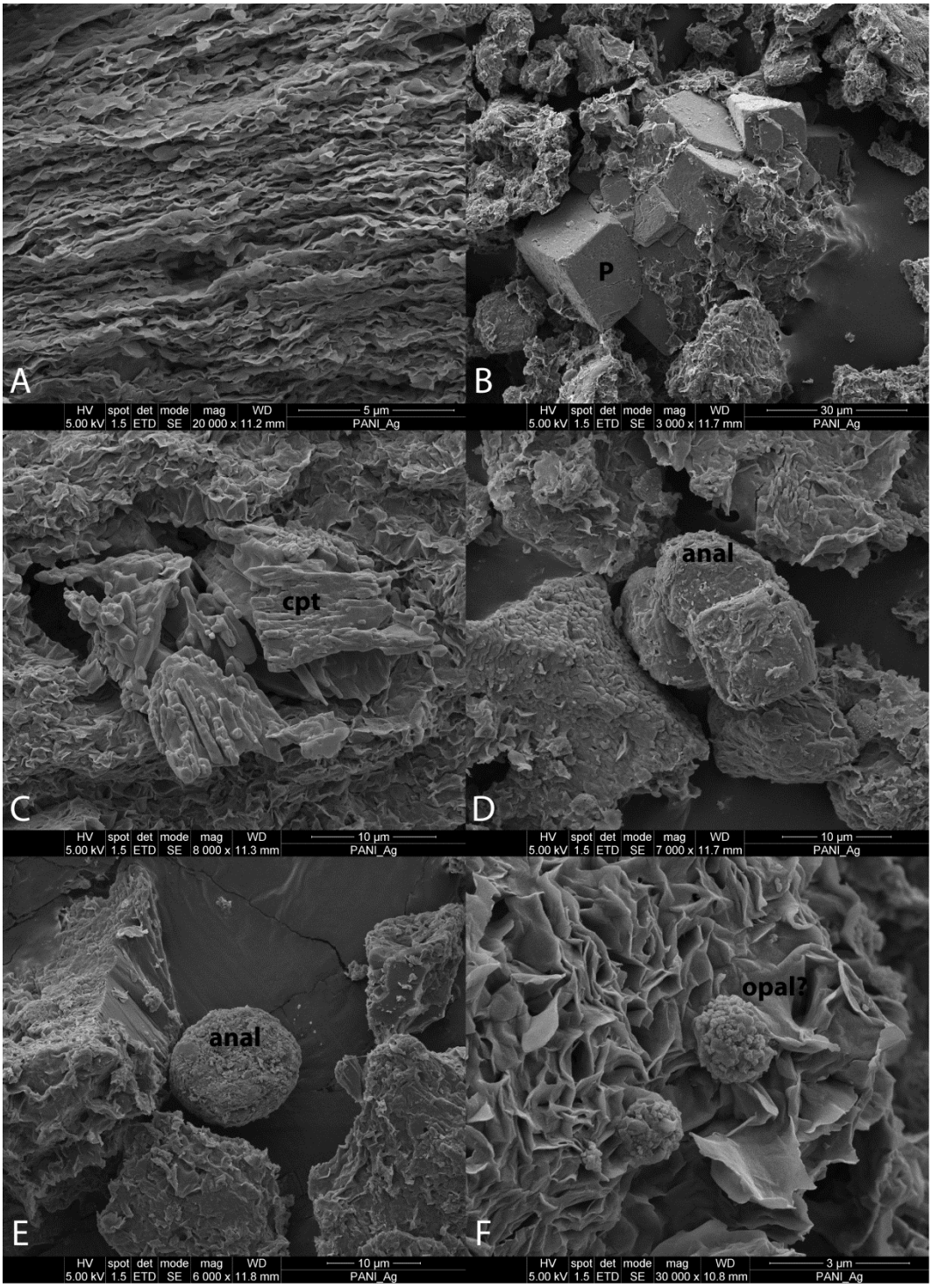

Figure 3. SEM images of reaction products from EBS-12. A) Bedding associated with the montmorillonite foils developed during pressurization in a fluid poor environment. B) Unaltered, cubic pyrite. C) Partially altered clinoptilolite showing dissolution features. D) Poorly formed analcime aggregates next to a partially altered clinoptilolite (lower left). E) Deformed analcime particle. F) Possible opaline nodule precipitated on montmorillonite edges.

3.3 Six-Month Cooling – EBS-13

3.3.1 Mineralogy. Mineral reactions observed in the six-month, cooling experiments are consistent mineral reactions in the ramped and isothermal experiments. Partial dissolution of the montmorillonite developed rough edges during the long-term cooling experiments, but maintained the typical foily smectite morphology (Figure 4A and B). However, the glycol saturated samples yielded d_{001} of 17 Å with higher order $d_{00\ell}$ consistent with integer values of the d_{001} values (Figure 5), suggesting the montmorillonite did not undergoes extensive illitization.

Analcime and cristobalite formation appears to be as a result of clinoptilolite dissolution and silica saturation with respect to cristobalite. 5 to 10 μm analcime particles (Figure 4D) have an average structural composition of $(Na_{0.64},Ca_{0.05})(Si_{2.23},Al_{0.76})O_6{\cdot}nH_2O$. Analcime growth appears to have been stopped due to the quenching of the reaction preserving the various stages of analcime ripening.

Odor of the aqueous samples and loss of pyrite in post-experiment samples suggests pyrite decomposition occurred during the experiments yielding $H_2S_{(aq,g)}$. Experiments containing stainless steel evolved $H_2S_{(g)}$ more readily, limiting sulfide-induced corrosion. Experiments with Cu° plates did not evolve substantial $H_2S_{(g)}$ due to chalcocite (Cu_2S) formation on Cu surfaces.

SEM examination of the bulk material and > 2 μm fraction indicates minor amounts of an authigenic fibrous mineral. These fibers occur as bundles or isolated fibers (Figure 4C). Fiber lengths span from 1.5 μm to 17.4 μm with widths ranging from 0.10 μm to 0.51 μm, producing aspect ratios (l/w) from 15.5 to 55.5. Chemical analyses of the discrete fibers were not collected due to the fiber thicknesses and the chemical contribution from the underlying montmorillonite.

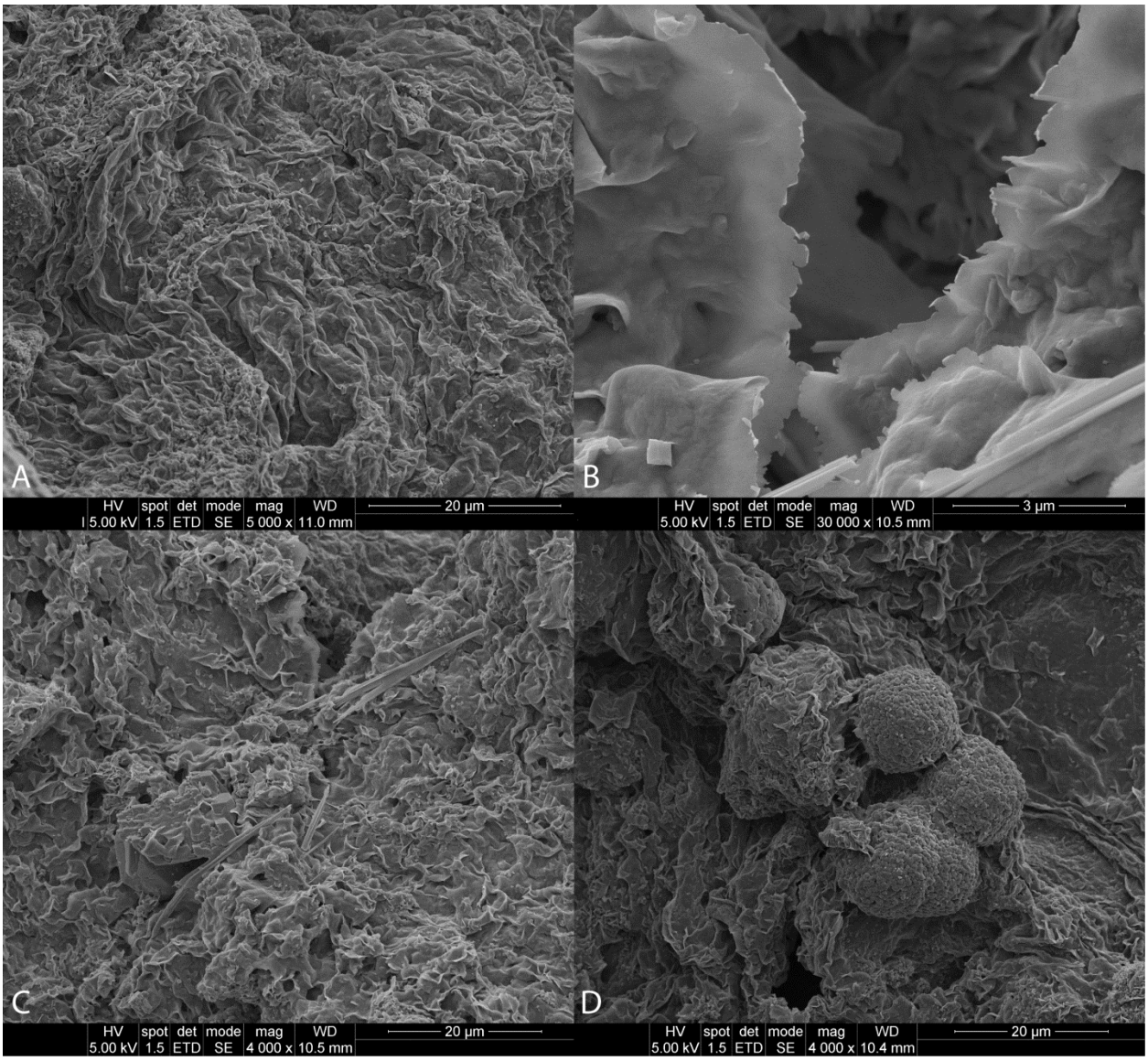

Figure 4. SEM images from EBS-13 bulk samples. A) Typical smectite foily morphology. B) Smectite edges with increased roughness possibly from partial dissolution during experiment. C) Foily smectite with fibrous/acicular minerals. Fiber identity is currently unknown but might be a zeolite or illite. D) Agglomerated nanometer-sized high-silica analcime particles showing spherical morphology.

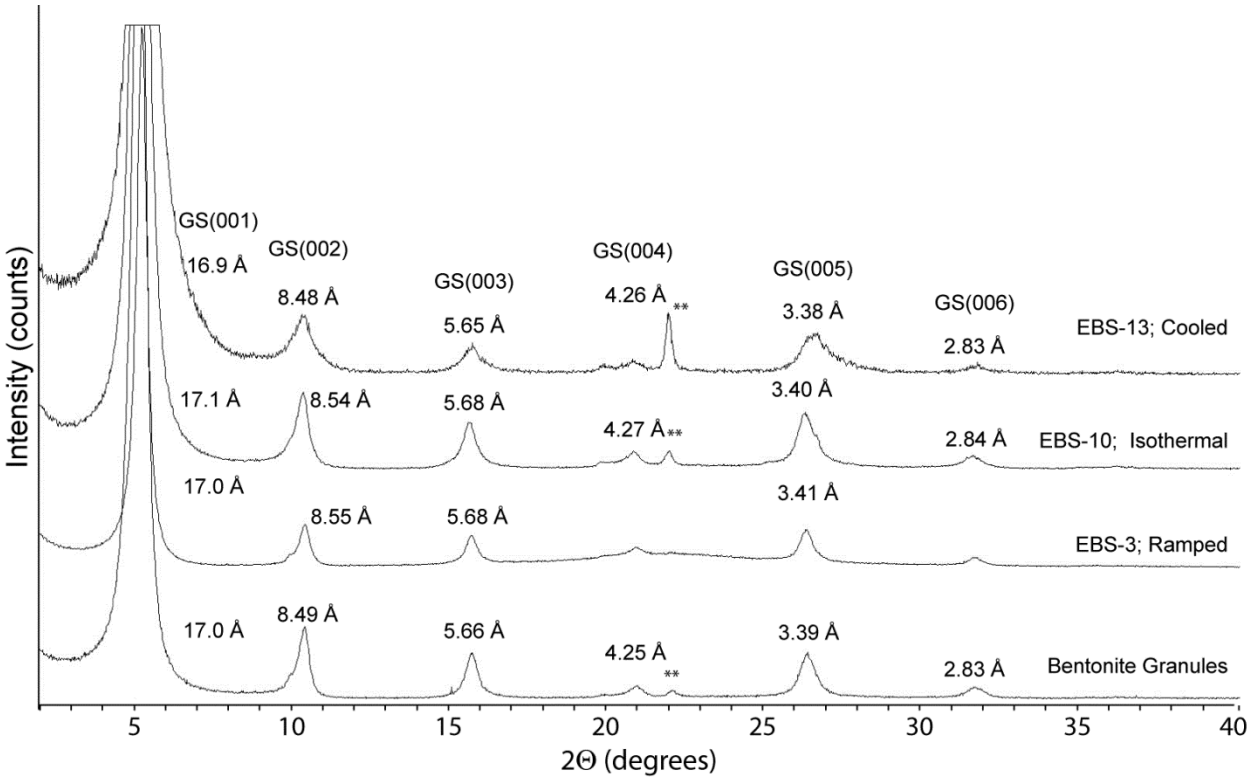

Figure 5. XRD patterns from the ethylene glycol saturated, oriented -2 µm fractions showing the effects of differing heating profile and duration on the montmorillonite fraction. ** represents opal-CT or cristobalite.

3.3.2 Solution Chemistry. Solution chemistry for the six-month (EBS-13) experiment is presented in Appendix C; Table C1 to C2. Changes to the solution chemistry are fairly consistent between the different EBS experiments. There is a Na^+ for K^+ exchange in the solution most likely controlled by the cation exchange capacity of both the Na-montmorillonite and clinoptilolite (Figure 6A). This cation exchange yielded a 274 - 470 mg/L Na^+ enrichment and 491 - 514 mg/L K^+ depletion in solution producing a K^+ enriched montmorillonite. However, this does not replace all Na^+ in the montmorillonite interlayer, thereby maintaining a Na-rich montmorillonite. Additionally, a 55.3 - 59.7 mg/L decline in the Ca^{2+} aqueous concentrations was observed during experiments mostly due to montmorillonite exchange.

Silica activity remained low during the 300°C stage of the six-month long experiment (Figures 6B). However, it is believed that silica precipitation occurred during storage at 1°C forcing an artificially low silica concentration. This is supported by the transparent solids at the bottom of the aqueous samples. Additionally, silica concentrations jumped up to 600 to 700 mg/L upon lowering reaction temperature to 220°C. Based on the other two experiments (EBS-3 and EBS-10); silica concentrations should have and probably reached 1,000 to 1,200 mg/L at 300°C (Figure 6B). Silica concentrations decreased incrementally following the temperature profile during the cooling stages of EBS-13. Partial smectite dissolution and clinoptilolite alteration are likely controls on silica activity.

Sulfur evolution is complicated by the occurrence of multiple redox states and interaction with metal plates (Figure 7). These probably contributed to the mixed results regarding sulfur concentrations. Past experiments showed in ramped experiments sulfur (as sulfate) increased from ~47 mg/L to ~125 mg/L until reactions temperatures reached 300°C, when sulfur values dropped to ~46 mg/L. However, during the 300°C experiments, sulfur concentrations steadily climbed to a ~191 mg/L. In the current experiments, sulfur ranged from 60 – 81 mg/L at 300°C, increased to 142 – 156 mg/L at 210°C, and slightly decreased to 123 - 129 mg/L at 120°C.

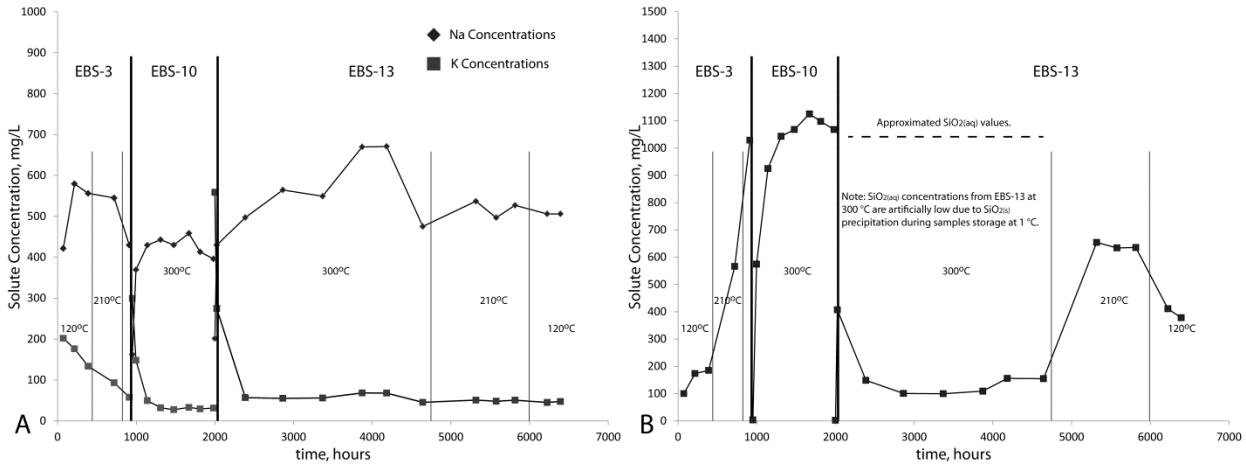

Figure 6. Solution chemistry evolution combining EBS-3, EBS-10, and EBS-13 showing full experimental heating profiles. Each experiment started with a fresh solution therefore slight discrepancies exist between each experimental solution profile. $SiO_{2(aq)}$ concentrations from EBS-13 at 300 °C are artificially low due to $SiO_{2(s)}$ precipitation during sample storage at 1 °C.

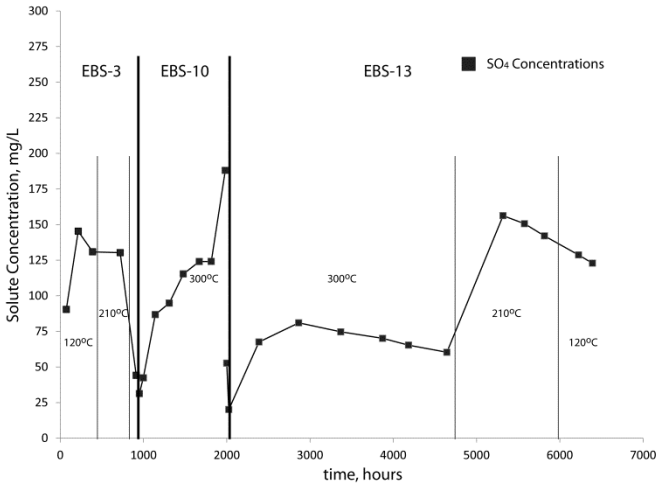

Figure 7. Sulfur (presented as sulfate) evolution combining EBS-3, EBS-10, and EBS-13 showing full experimental heating profiles. Each experiment started with a fresh solution therefore slight discrepancies exist between each experimental solution profile.

3.3.3 316 SS Corrosion. Chemical analyses for steel (EBS-5 and EBS-10) and copper (EBS-4 and EBS-11) corrosion products are presented in Appendix B; Tables B8 to B19. The initial 316 SS (NIST SRM 160b) is an iron alloy primarily with 18.37 wt. % Cr, 12.35 wt. % Ni, 2.26 wt. % Mo, 1.619 wt. % Mn, 0.5093 wt. % Si, and 0.175 wt. % Cu.

All systems containing stainless steel (304SS or 316SS) seem to behave similarly. Results from the six-month, 316SS experiment are indistinguishable from the previous two 316SS experiments (EBS-3 and EBS-10). Corrosion products associated with 316 SS were primarily smectite with minor occurrences of pentlandite ($(Ni, Fe)_9S_8$) (Figure 8). Smectite expands to 16.8 Å (with 002 at 8.44 Å) upon ethylene glycol saturation suggesting no significant amount of mixed-layering is present. XRD data (06l diffraction bands) and chemical analysis suggest that the smectite associated with 316SS corrosion is a Fe-saponite (Figures 9 and 11). The smectite morphology tends to be fairly consistent producing a bladed to micaceous habit with a rose-like texture (Figure 10). Chemical analyses of post-reaction 316SS and corrosion products indicates there was significant Fe and Ni leaching from the 316SS forming a chromite-like film on the stainless steel surface (Figure 11). Nickel leached from the stainless steel is partitioned into the sulfide phase. Fe-saponites were precipitated most likely from the iron leached from the 316 SS and the silica-rich fluid from the bentonite system. Fe-rich phyllosilicates that formed on steel plates in the ramped experiments have 06ℓ diffraction bands 1.535 Å (9.210 Å b-parameters), corresponding to a Fe-saponite (Figure 9; Kohyama et al. 1973; Moore and Reynolds 1997).

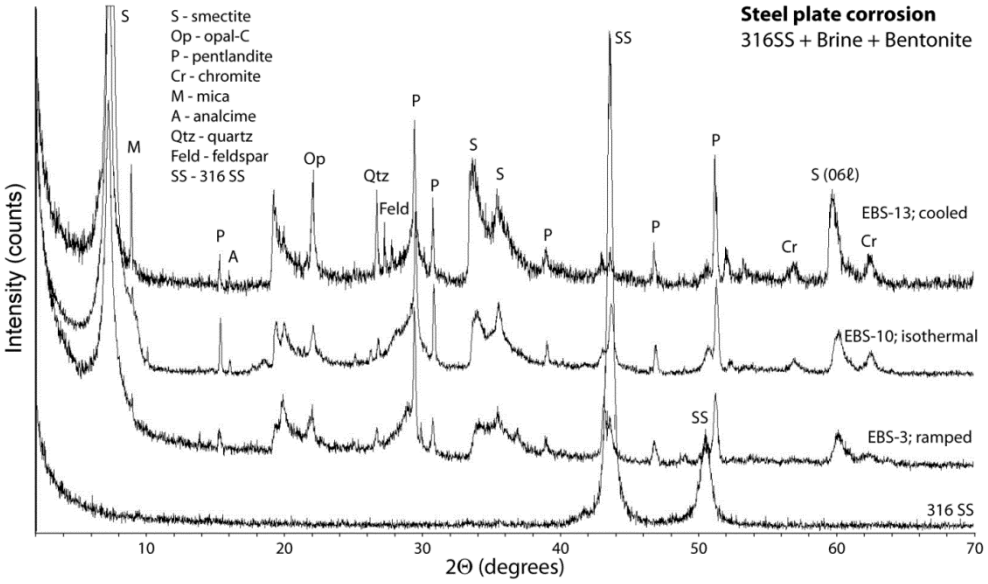

Figure 8. XRD patterns of the starting 316SS and corroded 316SS plates from EBS-3; -10; and -13. Fe-saponite is the dominate corrosion product associated with steel. Sulfide is the primary sink for leached Ni forming both pentlandite and millerite. Mica, analcime, quartz, and feldspars are from residual bentonite coating the steel plates.

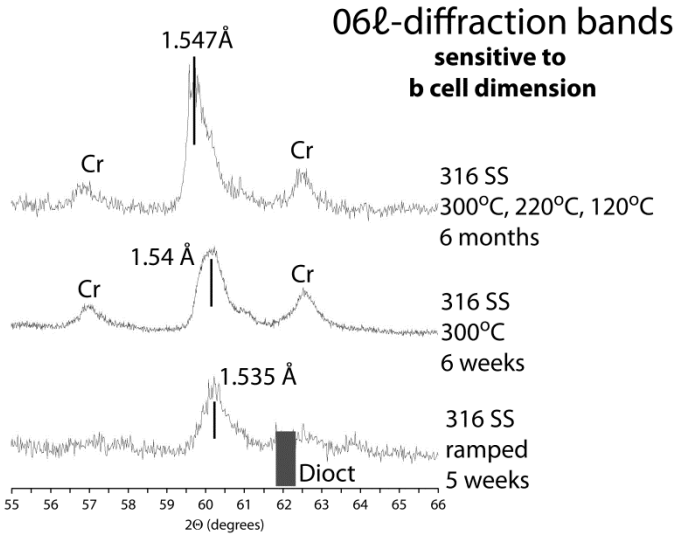

Figure 9. XRD plots of the showing the 06ℓ diffraction bands or Fe-rich smectite formed during EBS-3, EBS-10, and EBS-13. d-spacings ranging from 1.535 – 1.547 Å (9.210 - 9.282 Å *b* unit cell dimension) corresponding to trioctahedral phyllosilicates. Montmorillonite (dioctahedral) typically has a 1.492 – 1.504 Å (8.952 – 9.024 Å *b* unit cell dimension) 06ℓ band (red box). The smectite principally is a Fe-saponite with varying amounts of Ni and Cr substitutions. Chromite (Cr) signal is derived from the passivation layer developed on the 316SS surface from preferential Fe and Ni leaching.

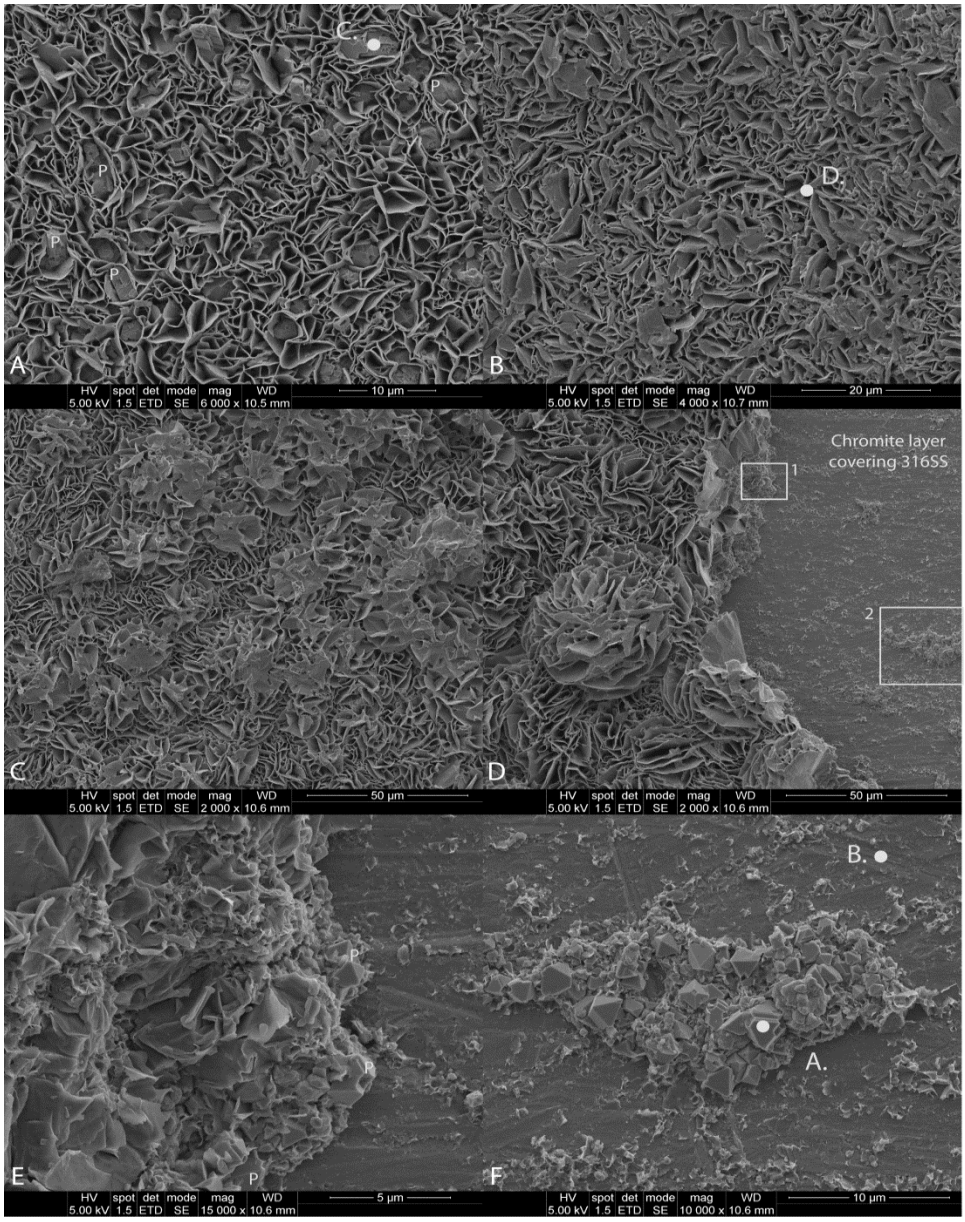

Figure 10. SEM image of corrosion products from 316 SS in EBS-13. A) Typical Fe-saponite morphology associated with 316SS surfaces with intergrowths of pentlandite (P) and without pentlandite intergrowths (B). Energy dispersive X-ray (EDX) analyses at points C. and D. are presented in Figure 11 C and D. C) Start of the two-layer corrosion layers previously seen in 316SS corrosion. First-layer characteristics are represented in A and B, but the second-layer has a rose-like and botryoidal texture. Change in textures might be due to changing substrates for Fe-saponite growth. D) Interface between Fe-saponite and the chromite surface associated with 316SS. E) Close up of the Fe-saponite-chromite interface (Box #1) with extensive pentlandite growths at the interface. F) Pentlandite cluster (from Box #2) directly in contact with the chromite surface associated with the 316SS. EDX analyses at points A. and B. are presented in Figure 11 A and B.

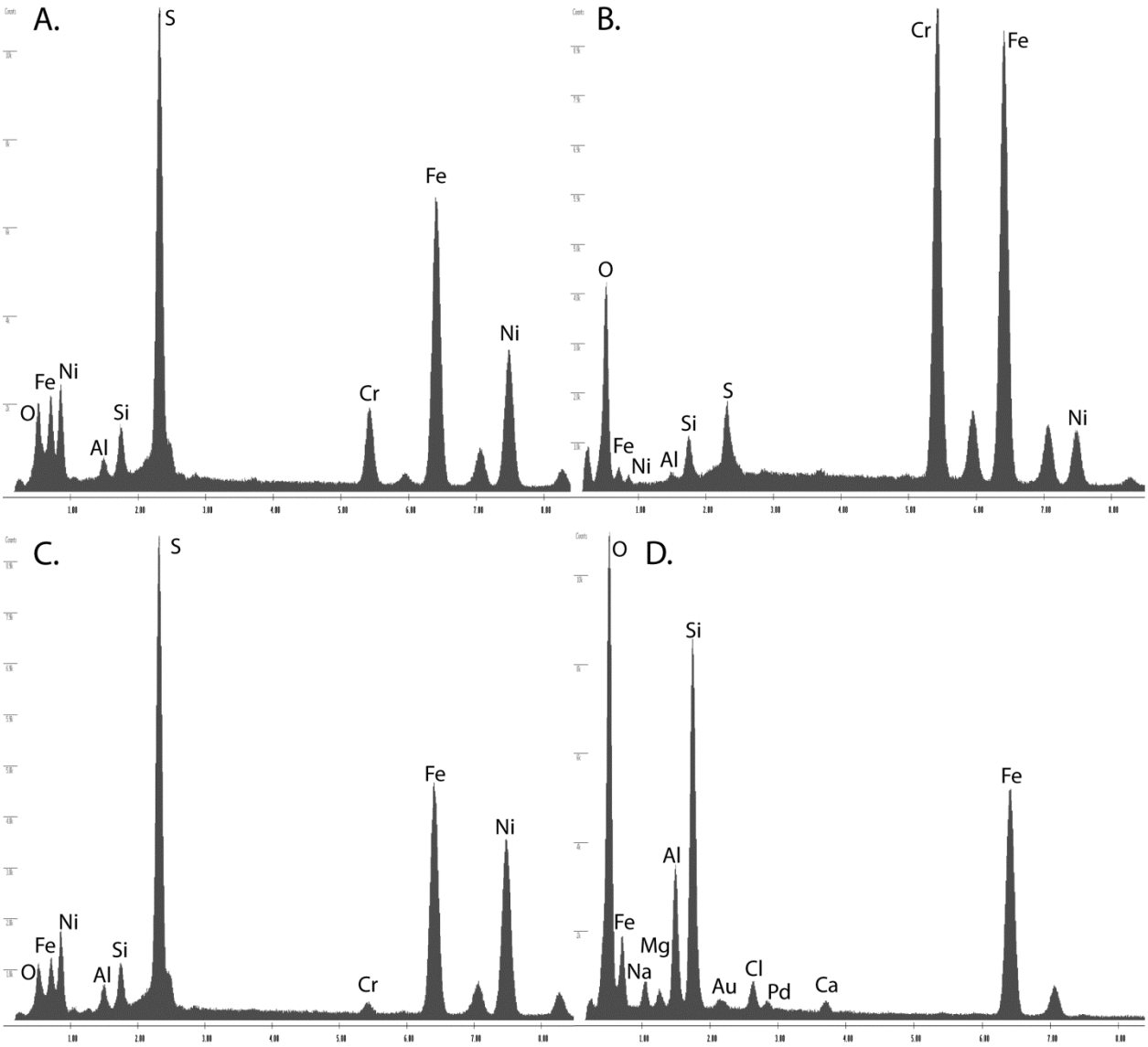

Figure 11. EDX analyses of 316SS corrosion products associated with EBS-13 in Figure 10. Letters correspond to locations described in Figure 10. A) Octahedral pentlandite immediately in contact with the chromite passivation layer. B) Clean surface of the 316SS indicating much of the surface corresponds to the chromite passivation layer. C) Pentlandite surrounded by saponite foils. D) Fe-saponite on edge to minimize underlying contamination. Chloride is primarily from NaCl formation upon drying.

3.4 Chemical Mapping from EBS-10.

Figure 12 is an EDX chemical map from a cross-section of a 316SS plate from EBS-10. It is evident from the mapping Ni and S are strongly associated with little correlation to Fe.

Based on the fibrous morphologies in the previous report (Caporuscio et al., 2013) and a Ni-S correlation, it is evident that millerite (NiS) also is a corrosion product not previously identified. Sulfide minerals appear to form early in the corrosion process, most likely due to very low Fe and Ni solubility in the presence of sulfide. Fe-saponite growth seems to become the primary corrosion product as sulfide crystallization tapers off, either from sulfide or Ni depletion. However, there appears to be a second pulse of sulfide formation developing a secondary layer of sulfide-saponite products. The oxide passivation layer (chromite) is evident by the bright green zone at the 316SS surface in the O-K chemical map.

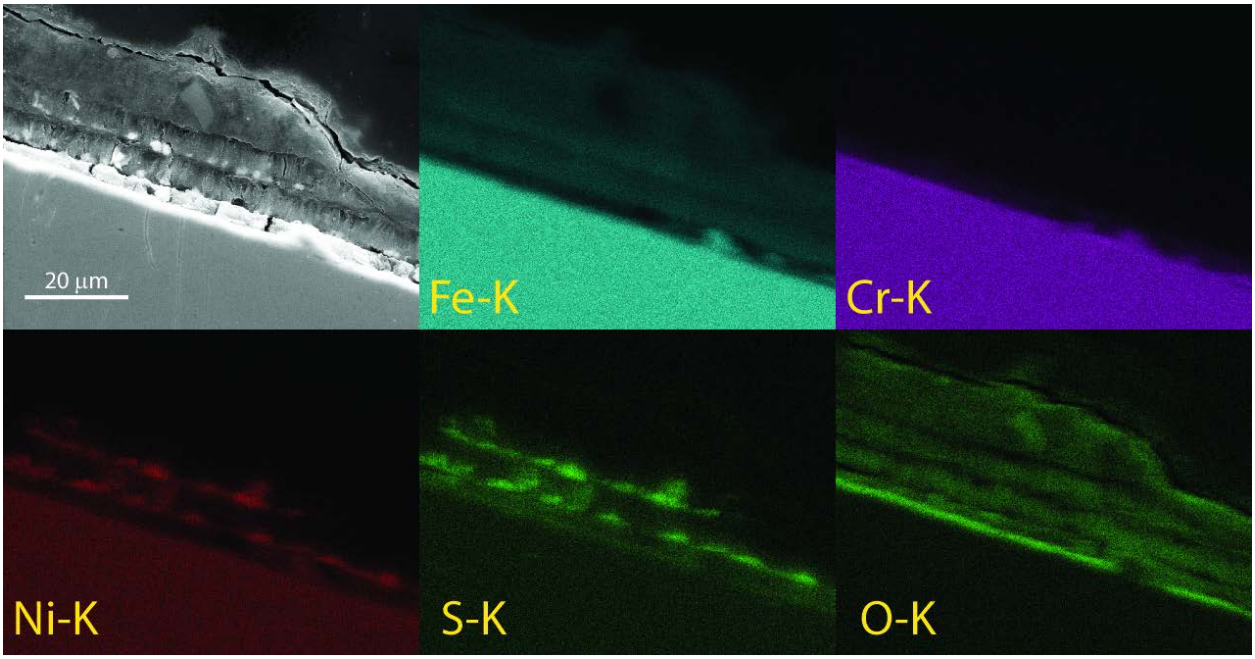

Figure 12. Chemical mapping of the 316SS from EBS-10 showing the distribution of Fe, Cr, Ni, S, and O at the metal-bentonite boundary dominated by corrosion products.

3.5 Opalinus Clay Experiments

3.5.1 Original Opalinus Clay. Opalinus Clay is thinly-laminated, dark grey shale with dry density of 2.2–2.4 g/cm^3 and water content of 6.5–8.0% (Pearson et al., 2003). This shale is dominated with 69 wt. % illite, illite-smectite mixed layers, and discrete smectite (Table 8, Figure 13). These phases were quantification together due to difficulty of quantifying these mineral phases when they are mixed. The illite-smectite appears to be a low expandable with a

R3 illite (0.92)-smectite composition. Other clay minerals present in significant quantities include kaolinite (12 wt. %) and chlorite (1 wt. %) (Table 8, Figure 13). These clay minerals are intimately mixed making them indistinguishable in the SEM investigation (Figure 14A and B). The exchangeable cations present within the clay fraction are listed in Table 9 (Pearson et al., 2003). Na^+ is the dominant exchangeable cation in the Opalinus Clay followed by Ca^{2+}, Mg^{2+}, K^+, and Sr^{2+}, however, the bulk composition is dominated with CaO (7.96 wt. %), K_2O (3.05 wt.%), MgO (2.38 wt. %), and Na_2O (0.481 wt. %). These exchangeable cations should be in equilibrium with the pore water described above (Table 2). Other minerals present include calcite, ankerite, dolomite, quartz, and biotite. Well-preserved pyrite occurs primarily as < 2 µm octahedral crystals, filling fractures and/or along bedding planes. Calcite primarily occurs as pocket filling agglomerates showing layered structures with alternating calcite and clay layers (Figure 14E and F). Ankerite and dolomite were not observed in SEM analyses.

	Opalinus Clay Switzerland	Bentonite Wyoming	EBS-14 Opalinus	EBS-15 Bent-Opalinus
Illite, I-S, S	69		78	72
Smectite		72		
Chlorite	1	b.d.l.	3	+
Kaolinite	12	b.d.l.	b.d.l.	b.d.l.
Clinoptilolite	b.d.l.	13	b.d.l.	14
Analcime/Wairakite	b.d.l.	b.d.l.	3	1
Quartz	8	1	8	4
Cristobalite/Opal-C	b.d.l.	2	b.d.l.	b.d.l.
Biotite	0.5	3	0.8	0.5
Pyrite	+	0.4	0.7	b.d.l.
Plagioclase	b.d.l.	9	b.d.l.	8
K-feldspar	b.d.l.	b.d.l.	b.d.l.	+
Calcite	6	b.d.l.	5	b.d.l.
Dolomite	+	b.d.l.	b.d.l.	b.d.l.
Ankerite	2	b.d.l.	b.d.l.	b.d.l.

Table 8. Mineralogical composition of starting Opalinus Clay, Wyoming Bentonite, and reaction products from EBS-14 and EBS-15. + represents material detectable but below 0.5 wt. %. b.d.l. represents material below detection limits. Illite, illite-smectite, and smectite were combined in the analyses due to difficulty quantifying each phase when a physical mixture of two or three are present.

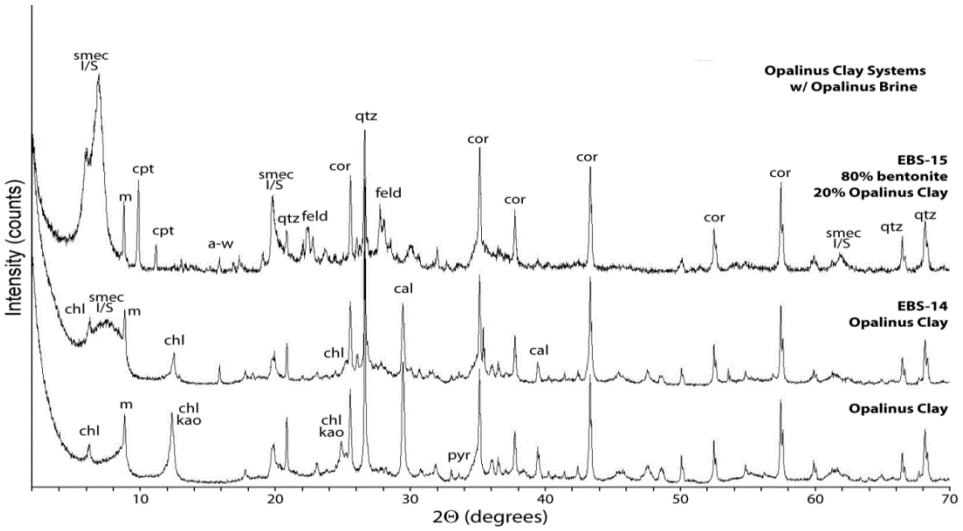

Figure 13. XRD patterns of bulk samples from starting Opalinus Clay and EBS-14 and EBS-15 reaction products.

Sample	Laboratory	Na	K	NH_4	Mg	Ca	Sr	Sum	Na	K	NH4	Mg	Ca	Sr
		meq/Kg_{rock}							% cation occupancy					
E2-Ni	Uni Bern	27.8	9.3		21.3	29.1	3.6	91.1	30.5	10.2	0.0	23.4	31.9	4.0
E3-Ni	Uni Bern	27	8.6		22	22.5	3.5	83.6	32.3	10.3	0.0	26.3	26.9	4.2
A4	CIEMAT	31.3	8.8		25.4	59.1	0.8	125.4	25.0	7.0	0.0	20.3	47.1	0.6
A5	CIEMAT	26	7.9		23.3	53.3	0.7	111.2	23.4	7.1	0.0	21.0	47.9	0.6
A5-Ni	Uni Bern	50.1	6.9		18.9	26.7	1	103.6	48.4	6.7	0.0	18.2	25.8	1.0
A1-C12	PSI case I	48.1	5.4		15.6	25.4		94.5	50.9	5.7	0.0	16.5	26.9	0.0
A1-C12	PSI case II	44.4	5.4		15.6	29.1		94.5	47.0	5.7	0.0	16.5	30.8	0.0
A6-Ni	Uni Bern	63.7	9		23.9	35.9	1.2	133.7	47.6	6.7	0.0	17.9	26.9	0.9
A6/MIN1	BRGM	58.2	15.2	23.7	28.9	36.6		162.6	35.8	9.3	14.6	17.8	22.5	0.0
A6/TEM1	BRGM	54.9	15.7	46	25.9	33.2		175.7	31.2	8.9	26.2	14.7	18.9	0.0

Table 9. Exchangeable cation populations for the Opalinus Clay associated with the Mont Terri Rock Laboratory (modified from Pearson et al., 2003).

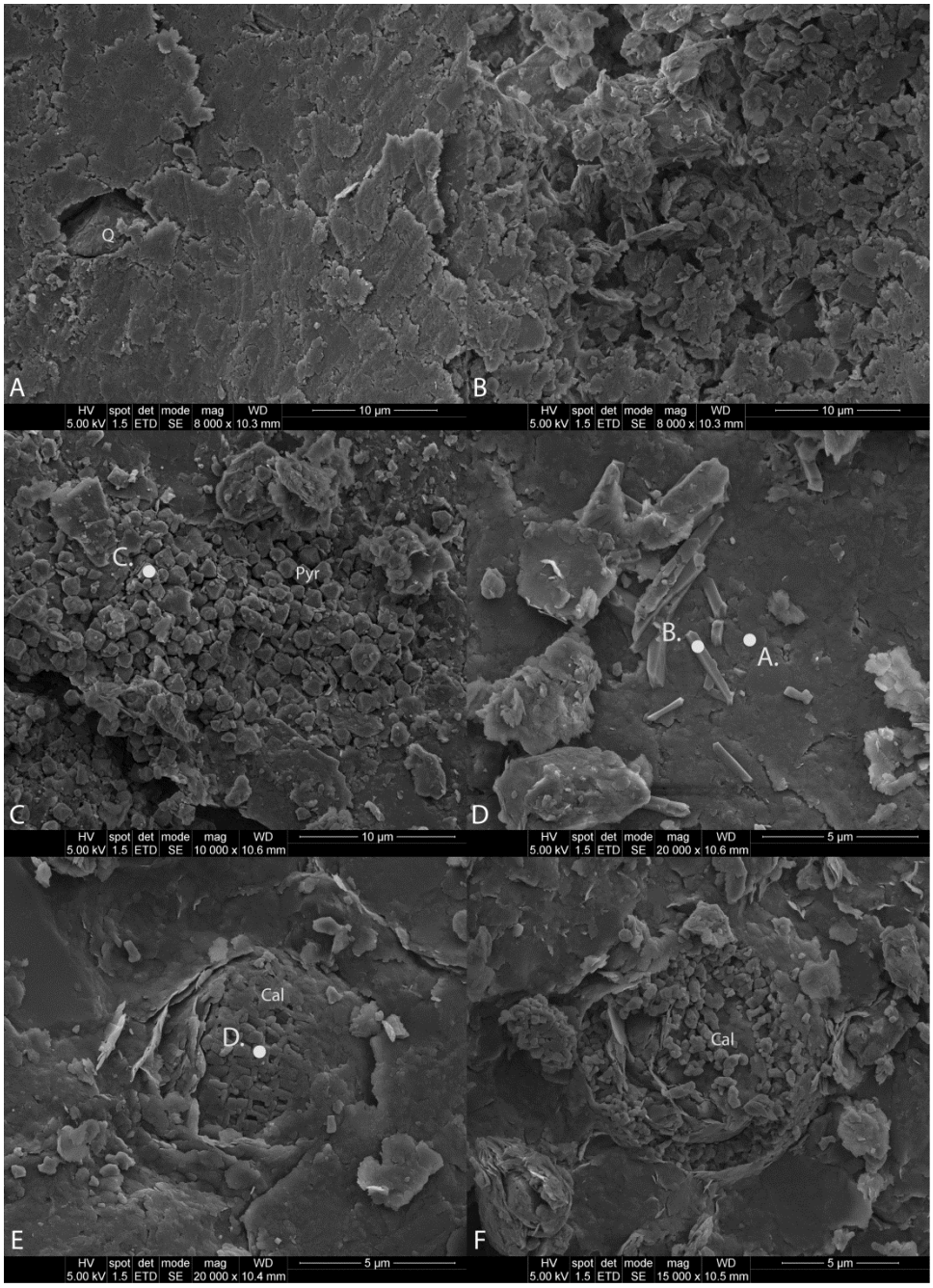

Figure 14. SEM images from Opalinus Clay. A) Opalinus Clay bedding planes formed from the aggregation of smaller particles. Quartz (Q) particle is imbedded in the matrix. B) Pore spaces within Opalinus Clay. C) Cluster of < 2 µm octahedral pyrite (Pyr) fill void spaces or are disseminated throughout samples. EDX analyses at point C. are presented in Figure 15C. D) Opalinus Clay bedding plane with platy-bladed mineral embedded in illite, illite-smectite, and chlorite matrix. EDX analyses at points A. and B. are presented in Figure 15A and B. E) Biogenic calcite (Cal) filling a pocket with in the Opalinus Clay matrix. EDX analysis at point D. is presented in Figure 15D. F) Disturbed pocket-filling calcite showing layered structure with alternating calcite and clay layers.

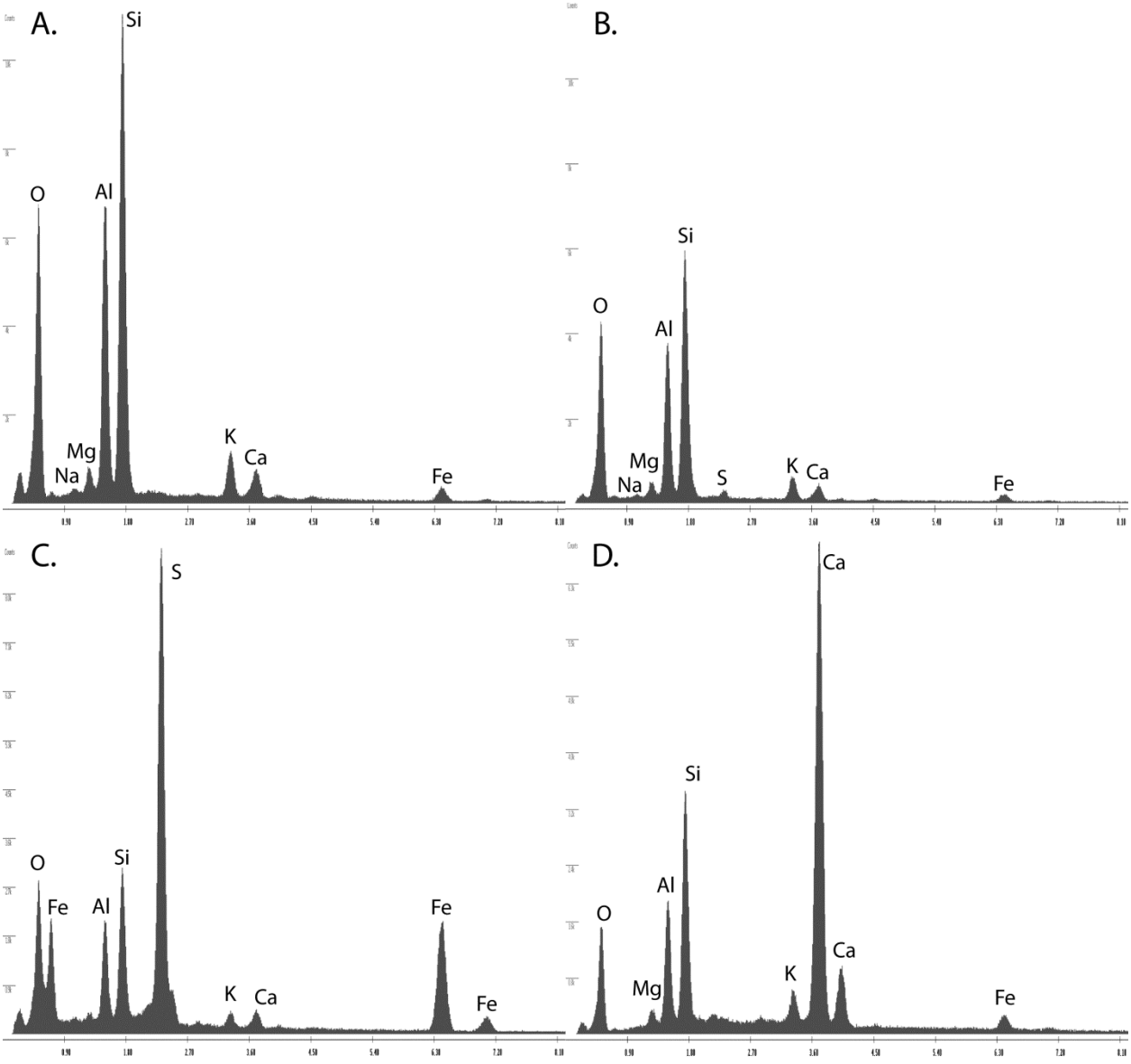

Figure 15. EDX analyses from Opalinus Clay starting material in Figure 14. A) Bulk compositions from the illite, chlorite, and illite-smectite matrix. B) Composition from the bladed structure. Composition is essentially indistinguishable from the clay matrix possible due to the zone of interaction during analysis gain strong influence from clay matrix. C) Composition from the octahedral pyrite clusters. Other non-pyrite elements are present from the clay matrix or clay mixing between pyrite particles. D) Elemental composition from the biogenic calcite filled pockets. Clay matrix is intimately mixed within the calcite crystals.

3.5.2 Post-reacted Opalinus. Clay mineral evolution in the Opalinus experiments is more diverse compared to the EBS experiments with bentonite as the only geomaterial due to the clay diversity in the Opalinus Clay. The starting Opalinus Clay is dominated with illite-smectite (I-S) mixed-layers and discrete illite with minor amounts of smectite. Reaction product from EBS-14 shows three different major clay fractions: two different I-S mixed layers and one illite fraction (Figure 16). It would appear that the two I-S fractions are an R3 illite (0.9)-smectite and a R1 illite (0.7)-smectite. Exact quantification is not possible, but it appears that the R3 I-S is the dominant phase in the EBS-14 reaction products.

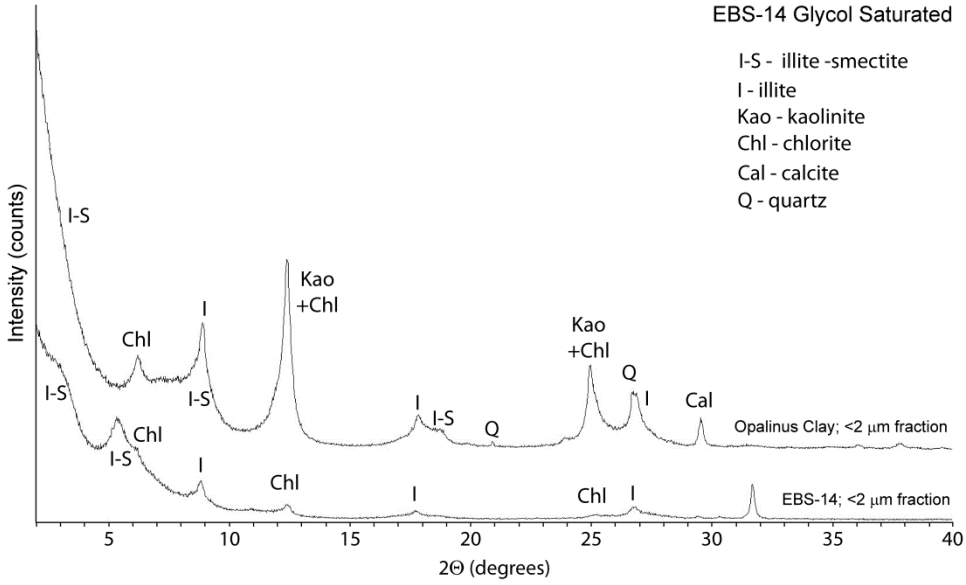

Figure 16. XRD patterns from the ethylene glycol saturated, oriented < 2 µm fractions from original Opalinus Clay and EBS-14 reactions products showing the effects of heating Opalinus Clay to 300°C for six weeks.

EBS-15 reaction products vary depending on the various < 2 µm fractions examined. In the bulk < 2 µm size fraction, all clay products show 100% expandability with minor occurrences of illite (Figure 17). It is evident from the bulk < 2 µm fraction, that (1) it is montmorillonite from the bentonite component that dominates this fraction and (2) this montmorillonite has not experienced significant illitization (i.e., > illite (0.05)/smectite). Montmorillonite expands to 16.8 – 16.9 Å with a Δ2θ (002/003) values of 5.25 – 5.25°, corresponding to 100% expandability (Figure 17). Post-reacted Opalinus Clay fragments from EBS-15 showed a composition more characteristic of the starting Opalinus Clay. It was

dominated with illite (possibly two), I-S, chlorite, and quartz. Illite could potentially be deconvoluted into a well-crystalline illite and a poorly-crystalline illite displaying a low, broad reflection superimposed on a sharp 10 Å illite reflection. The I-S appears to be a R0 illite (0.1)/smectite and expands to 16.8 Å with a Δ2θ (002/003) values of 5.44°, corresponding to 91% expandability. R1-3 ordered I-S were not detected.

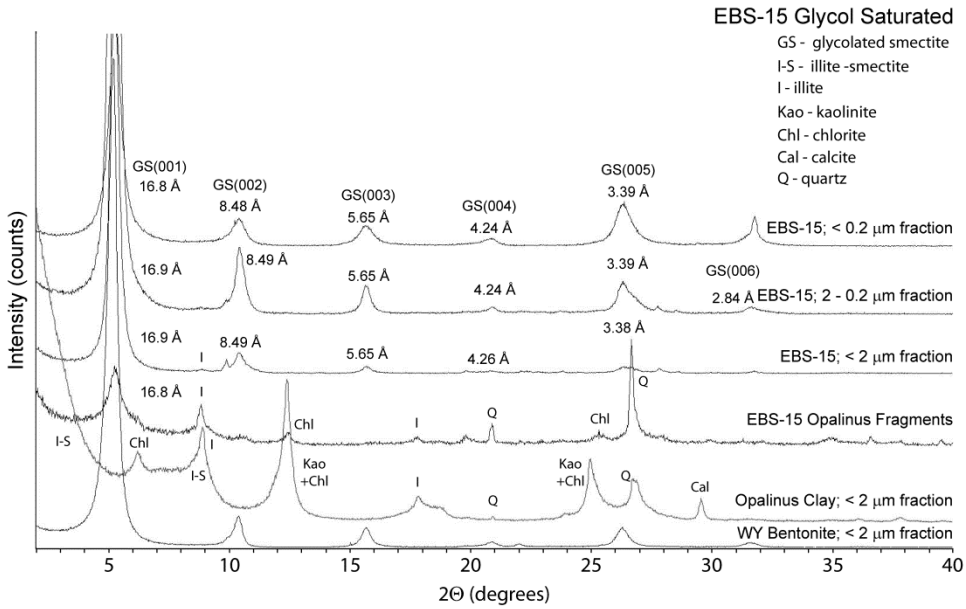

Figure 17. XRD patterns from the ethylene glycol saturated, oriented fraction from original Opalinus Clay, WY bentonite, EBS-15 Opalinus fragments, and various size fractions from EBS-15 reaction products.

There was significant analcime-wairakite formation with the addition of Opalinus Clay and brine. EBS-14 produced 22 – 53 µm analcime-wairakite particles (Figure 18B and C). Compositionally, these particles resemble wairakite with a high Ca/Na ratio (1.52 – 2.91) and a relatively low Si/Al (2.16), compared to the high-silicon analcime from the EBS experiments with Stripa solution and no Opalinus material (Figure 19A). EBS-15 produced spherical 10 - 20 µm analcime-wairakite particles with terraced surfaces from crystallization (Figures 19C and D; 21A and B). Compositionally, these analcime-wairakite particles have an intermediate composition with a Ca/Na ratio (0.206) and a relatively higher Si/Al ratio (2.70) compared to EBS-14, but lower Si/Al ratio compared to bentonite EBS experiments (Figure 21A). The analcime-wairakite material formed even though clinoptilolite was not present in EBS-14 and was preserved during EBS-15 (Table 8, Figure 13).

Other than the analcime-wairakite formation, is appears that a series of other zeolite were produced during EBS-14 and EBS-15. EBS-14 produced 2 – 5 µm fibers and a couple of 12 – 40 µm fibers throughout the samples (Figure 18A). Positive identification of these fibrous materials was not completed, but it would appear that the short prismatic fibers with a Si/Al (2.09) and Ca/Na ratio (0.472) are consistent with Na-rich laumontite ($CaAl_2Si_4O_{10}{\cdot}4H_2O$) (Figure 18C). The long fibers have 3.89 Si/Al and 0.371 Ca/Na ratios, along with a fibrous morphology suggests that these are either mordenite ($(Ca,Na_2,K_2)Al_2Si_{10}O_{24}{\cdot}7H_2O$) or erionite ($(K_2,Na_2,Ca,Mg)_4Al_8Si_{28}O_{72}{\cdot}28H_2O$) (Figures 20; 21C and D; and 22). These same bimodal fibrous populations were also present in EBS-15, with a greater concentration of the long fibers. There are no new XRD peaks that provide clues as to what the new phases are, but, morphology and composition suggests the long fibers are either mordenite or erionite and the short fibers are laumontite.

Kaolinite is the only mineral to undergo complete decomposition. The starting Opalinus Clay had 12 wt. % kaolinite, but EBS-14 and EBS-15 reaction products do not appear to have kaolinite (Table 8, Figure 13). EBS-15 kaolinite may have been diluted below detection limits with the addition of 80 wt. % bentonite (which does not have kaolinite). However, kaolinite if preserved should be around 2-3 wt. %, which is above detection limits for XRD.

It would appear from SEM data that pyrite was unaltered during the reactions. The octahedral pyrite still occupies fractures and/or between bedding planes and displays not signs of corrosion (Figure 18F). Also, there appears to be a partial calcite loss from 6 wt. % to 5 wt. % (EBS-14) to below detection limits (EBS-15), but SEM analyses show several pore-filling calcite nodules present throughout EBS-14 and EBS-15 reaction products (Table 8; Figure 18C). However, dolomite and ankerite does appear to have completely decomposed. Even though these carbonates were not observed in SEM, XRD data shows dolomite's and ankerite's complete removal. These carbonate mineral losses corresponds with excess gas evolution during fluid sampling. In most cases, 50 vol. % of the sampled volume was a mixed gas phase (most probably CO_2 and H_2S).

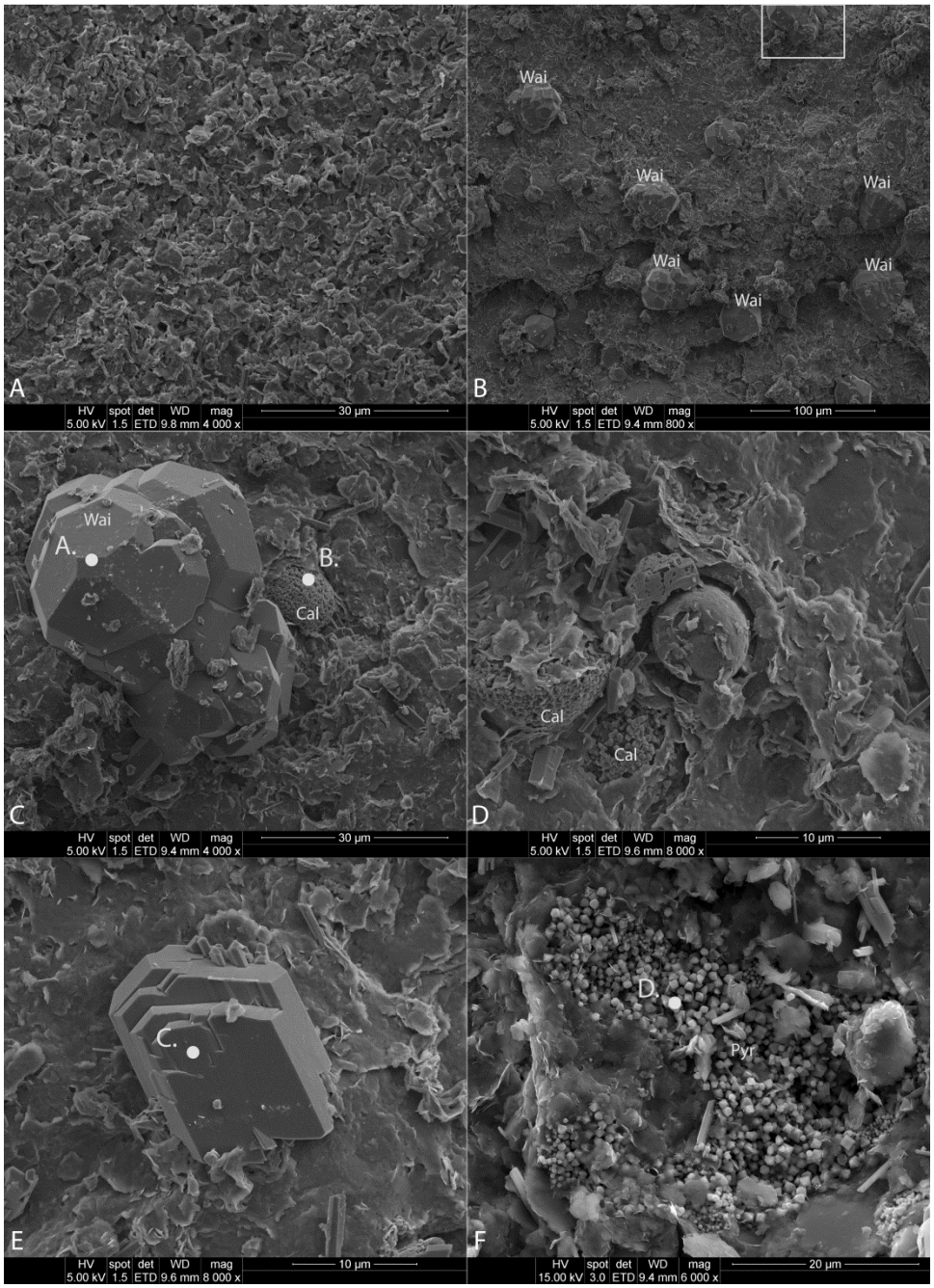

Figure 18. SEM images from EBS-14 Opalinus Clay. A) Fine grained illite, illite-smectite, chlorite matrix associated with post-reacted Opalinus Clay granules. 2 - 5 µm zeolite (?) fibers are dispersed throughout Opalinus Clay granules. B) 22 – 53 µm Na-bearing wairakite (wai). C) Close up of a euhedral wairakite crystal from Figure 18B boxed area. EDX analyses at points A. and B. are presented in Figure 19A and B. D) Remnant clay matrix associated with a nodule that underwent dissolution during EBS-14. Pockets typically have a clay rind preserved. Calcite (cal) is still preserved in this granule. E) Particle that might be associated with the 2 - 5 µm fibers. EDX analysis at point C is presented in Figure 19C. Composition suggests this particle is either a zeolite or feldspar. F) Cluster of 1-2 µm octahedral pyrite (Pyr) fill void spaces or are disseminated throughout samples. EDX analysis at point D. is presented in Figure 19D.

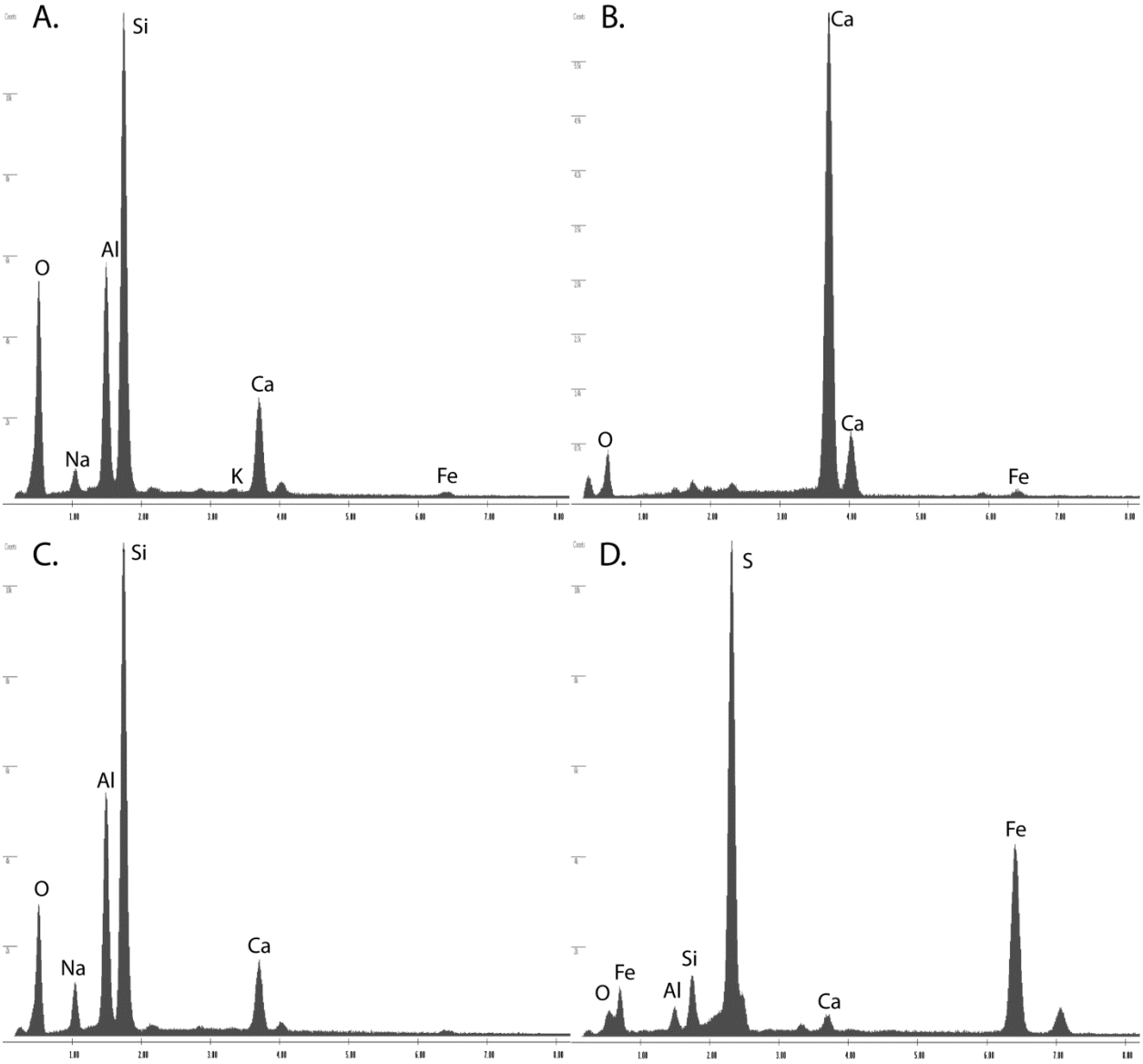

Figure 19. EDX analyses from EBS-14 reaction products in Figure 18. A) Composition of the Na-bearing wairakite particle (Si/Al = 2.16). B) Fine grained pocket filling calcite. C) Particle with a composition (Si/Al = 2.09) and morphology similar to laumontite or mesolite. However, positive identification of laumontite is not complete. D) Composition from the octahedral pyrite clusters. Other non-pyrite elements are present from the clay matrix or clay mixing between pyrite particles.

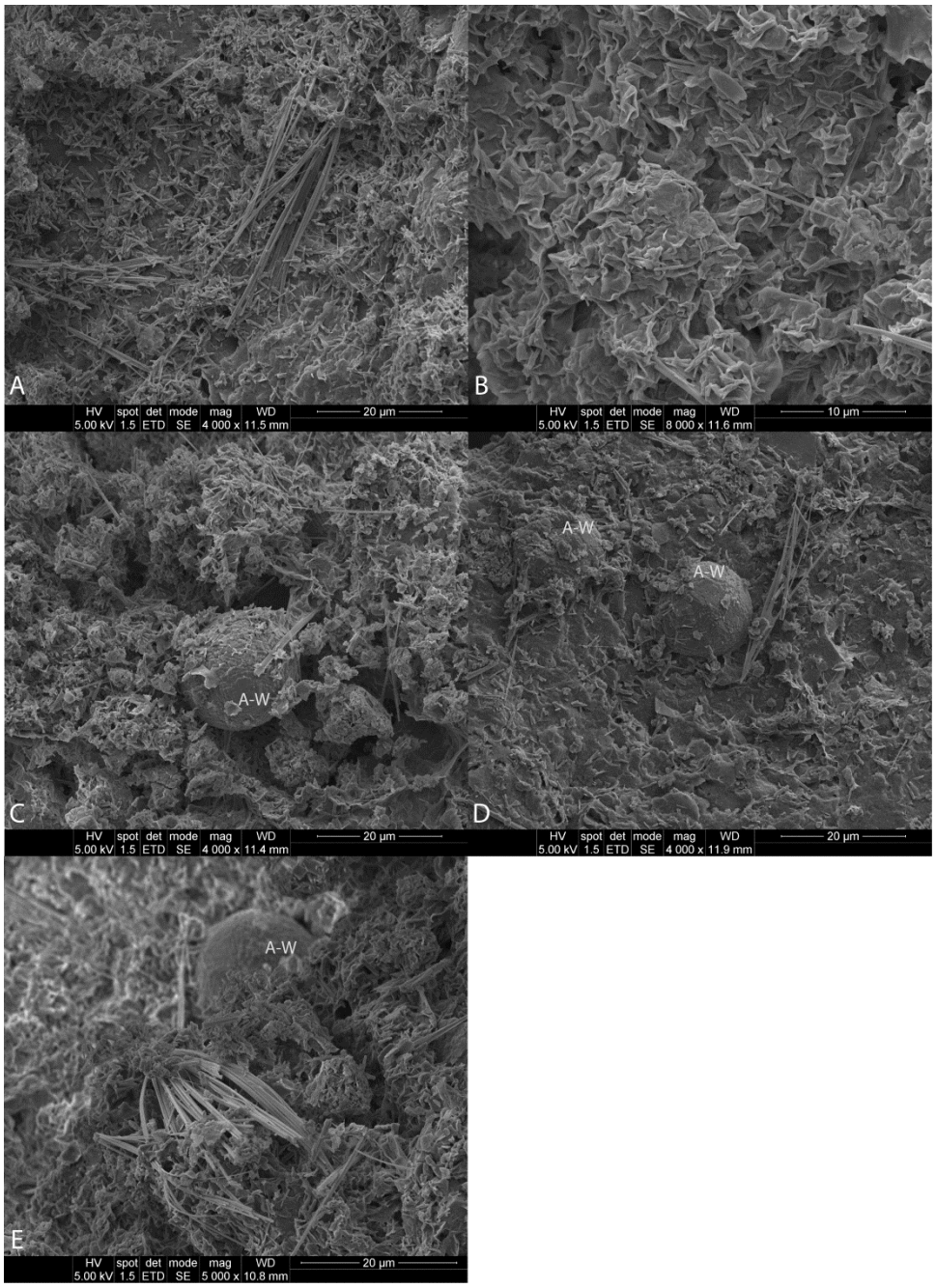

Figure 20. SEM images from EBS-15 bulk reaction products. A) A bimodal population of fibers ranging from 2 - 5 µm and 12 – 40 µm in length are dispersed throughout EBS-15 reaction products. EDX analyses on other fibrous material from EBS-15 suggest these fibers are either mordenite or erionite. B) Typical smectite foily morphology associated with WY bentonite mixed with fibers. C) Analcime-wairakite (A-W) crystal mixed within the clay matrix showing well developed growth terraces on the particle surfaces. EDX composition from separated analcime-wairakite is presented in Figure 21A. D) Analcime-wairakite crystal imbedded within the low porous clay matrix indicating analcime-wairakite grew within the clay matrix. Clay matrix in this image appears to be the Opalinus Clay. E) Fibers growing from a central substrate.

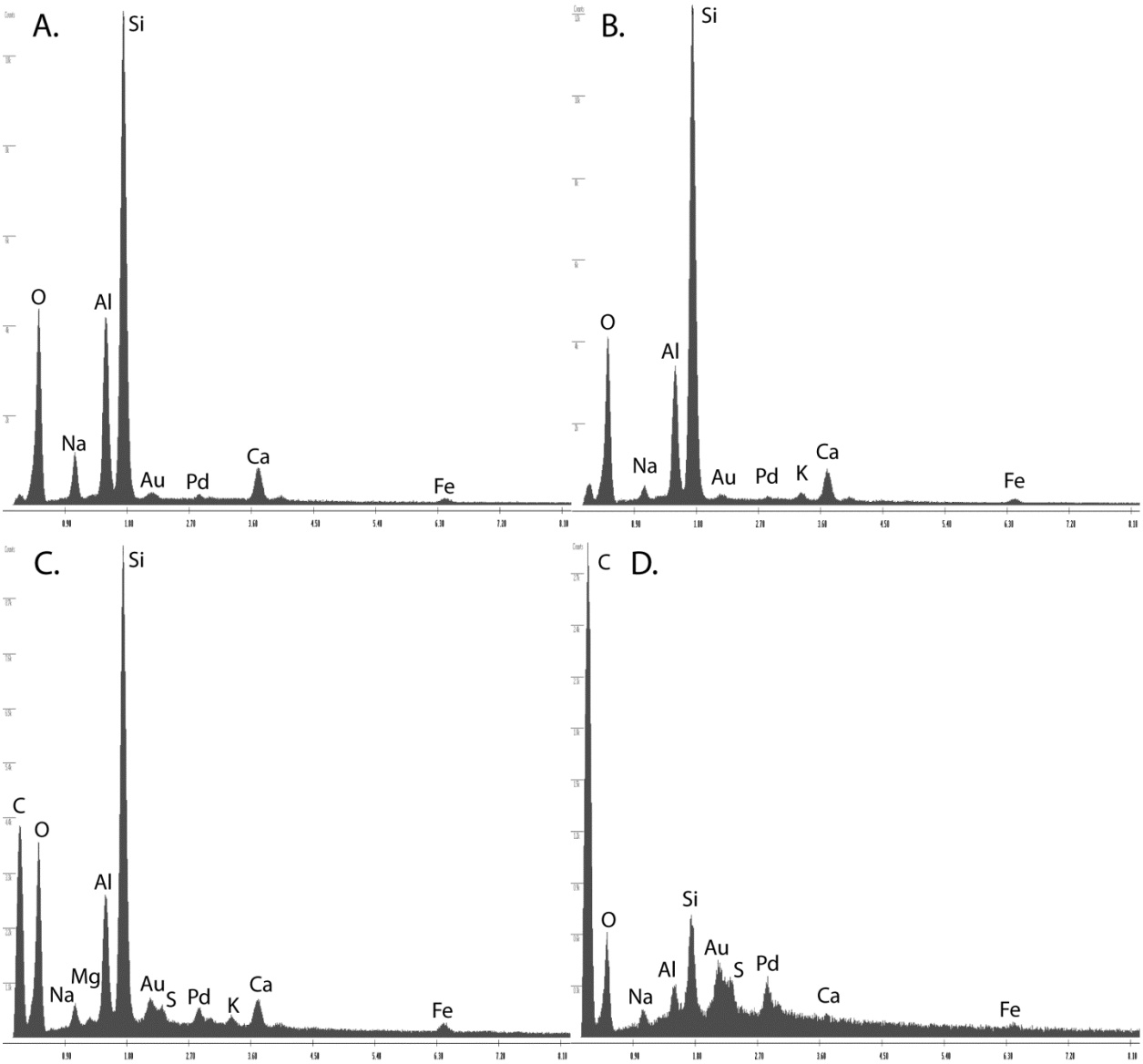

Figure 21. EDX analyses from > 2 µm grain mounts of EBS-15 reaction products. A) Analcime-wairakite product with an intermediate analcime-wairakite composition. Si/Al ratio is 2.70 is typical for a high-silica analcime-wairakite. B) Bladed material with a feldspar composition. C and D) Composition of the fibrous materials observed throughout the EBS-15 reaction products. Si/Al ratio is 3.85 suggesting the fibrous material could be either mordenite or erionite. Carbon peak is from the carbon tape in which the fibrous/acicular particles are affixed.

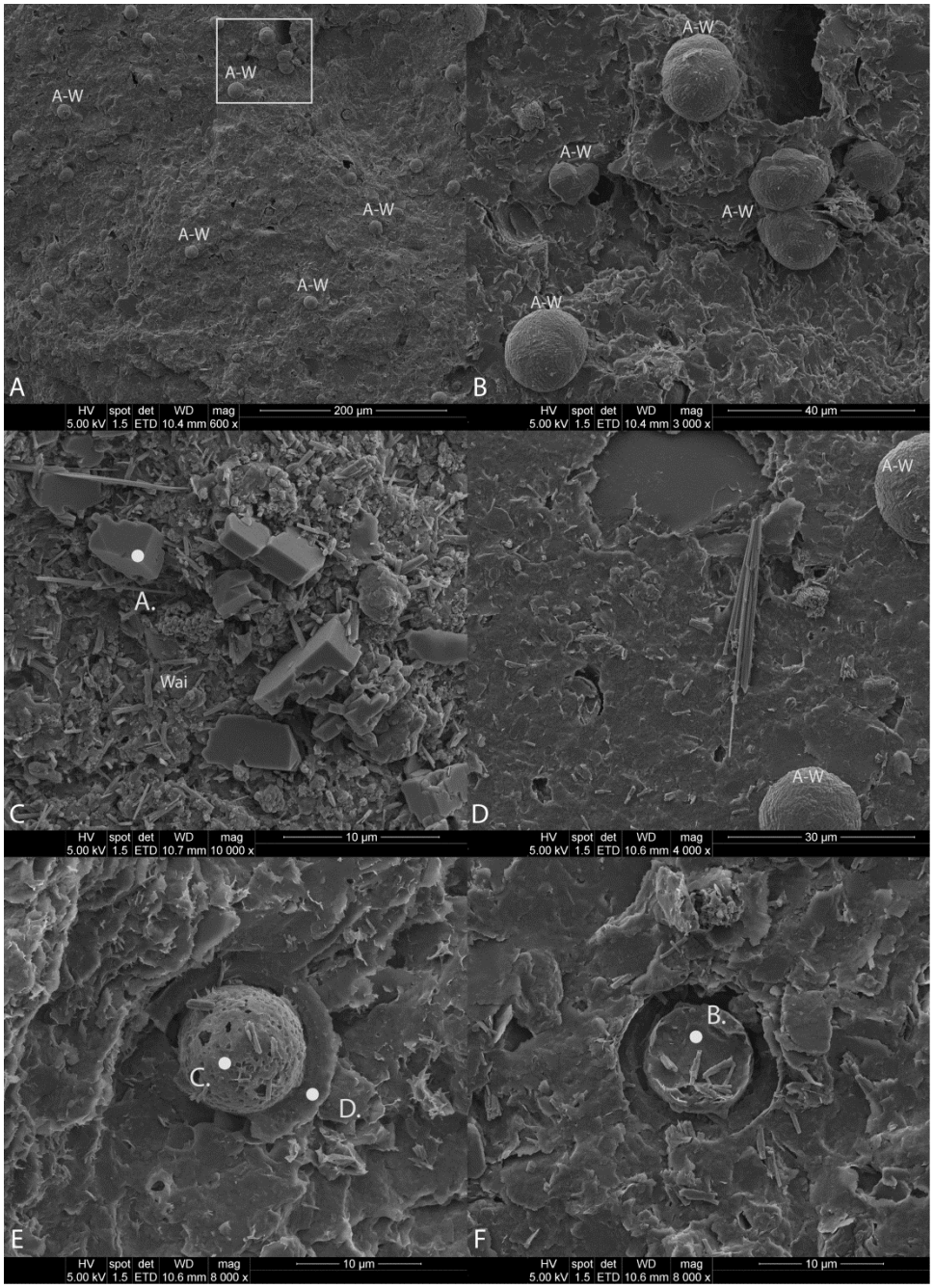

Figure 22. SEM images from EBS-15 Opalinus Clay fragments. A) 10 – 20 µm analcime-wairakite (a-w). B) Spherical analcime-wairakite crystal from Figure 22A boxed area. C) Possible feldspar crystals. EDX analysis at point A. is presented in Figure 23A. D) Possible mordenite or erionite fibers. E) Remnant clay matrix associated with a nodule that underwent dissolution during EBS-15. It is unclear what the original material in the pocket. Pockets typically have a clay rind preserved with a similar composition to the clay matrix, but enriched in Ti. EDX analyses at points C. and D. are presented in Figure 23C and D. F) Cleaved remnant clay matrix associated with a nodule that underwent dissolution during EBS-15. It is unclear what the original material in the pocket. Pockets typically have a clay rind preserved. EDX analysis at point B. is presented in Figure 23B.

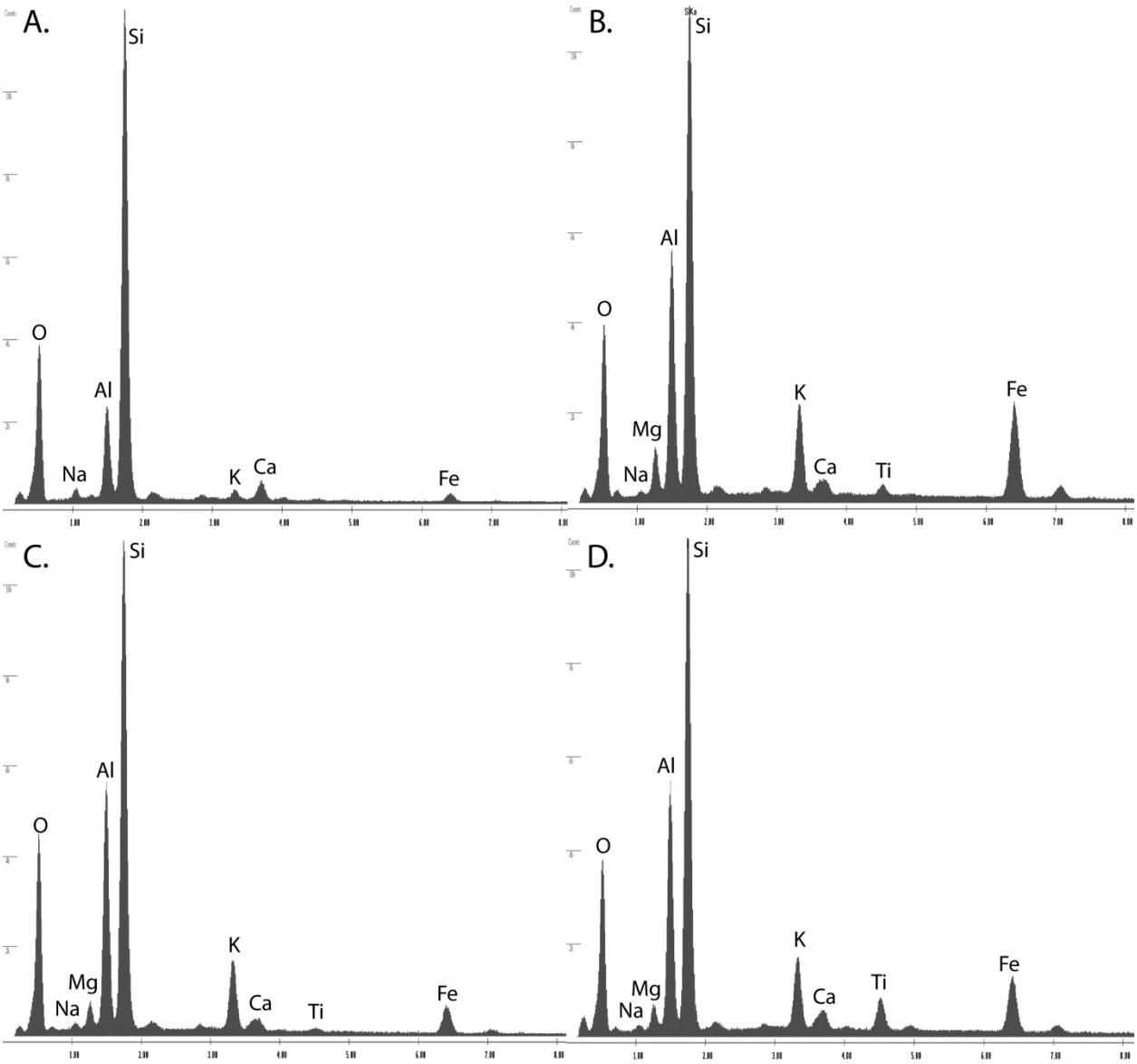

Figure 23. EDX analyses from EBS-15 Opalinus Clay fragments in Figure 22. A) Unknown, high-silicon material (Si/Al = 5.52) that displays dissolution. B) Cleaved spherical cavity filling clay material. This is probably the averaged composition between the illite, illite-smectite, and chlorite matrix. C) Spherical cavity filling clay material which probably is residual from the dissolution of the primary cavity filling mineral(s). D) Composition from the clay rind around the cavity. These Ti-enriched rinds are consistently associated with these spherical cavities. Composition from C and D are probably an average between the illite, illite-smectite, and chlorite matrix.

3.5.3 Solution Chemistry. Solution chemistry associated with the Opalinus Clay experiments are significantly different compared to solutions use in traditional EBS experiments (1-13). The fluid composition used in the experiment was derived from reported Opalinus Clay pore fluids. It is unknown whether the reported fluid composition is in equilibrium with the solid phases associated with the Opalinus Clay. Unlike experiments with Na-montmorillonite, there was not a major shift in the solution chemistry upon contact with solids during heating. Na, Ca, and K concentrations show fairly consistent concentrations during the experiment duration (Figure 23A). Sodium concentration ranged from 3400 to 4000 mg/L, calcium ranged from 300 to 600 mg/L, and potassium ranged from 100 to 250 mg/L. Silica also remained fairly constant even though there was a slight decline upon reaching 180 mg/L $SiO_{2(aq)}$ (Figure 24B). Chloride concentrations (Figure 24B) did not change significantly suggesting the experiment system remained sealed and no mass loss/gain developed. Sulfate concentrations dropped from 988 mg/L to below detection limits (1 mg/L; Appendix C; Table C3). Magnesium concentrations also experienced a drop from 197 mg/L to ~ 1 mg/L (Appendix C; Tables C3 and C4). Original solution pH (7.8) dropped immediately to 4.6 to 5.4 (Appendix C; Tables C3 and C4).

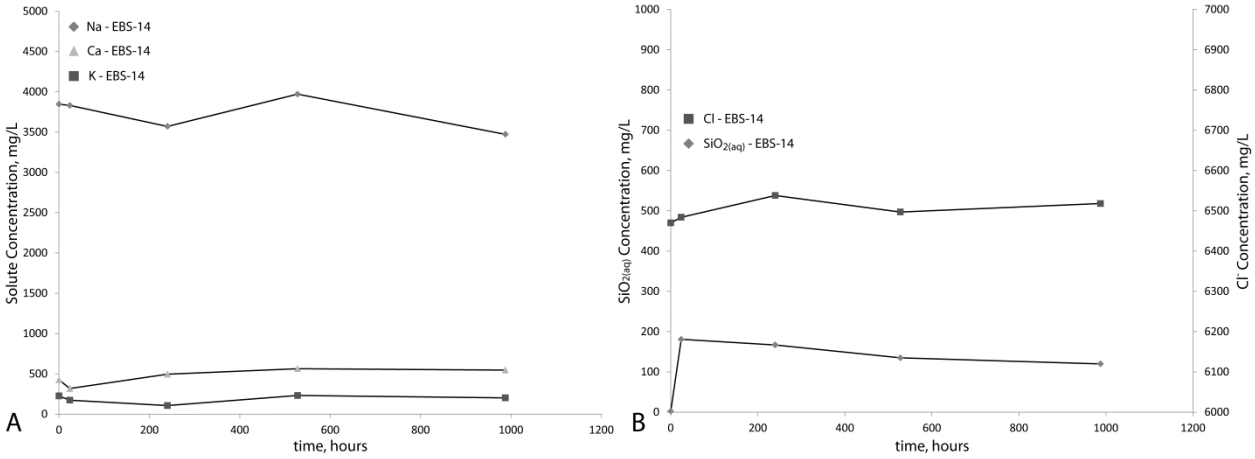

Figure 24. Solution chemistry associated with EBS-14. This reaction setup is Opalinus Clay with Opalinus brine. A) There appears to be no significant Na, K, and Ca exchange as each remains fairly constant during the experiment lifetime. B) Silica concentrations rapidly increase at the start of the experiment and stabilize around 150 mg/L. Chloride concentration does not change indicating no mass gain/loss during experiments.

3.5.4 Corrosion under Opalinus Clay conditions. Initial 316 SS (NIST SRM 160b) is an iron alloy primarily with 18.37 wt. % Cr, 12.35 wt. % Ni, 2.26 wt. % Mo, 1.619 wt. % Mn, 0.5093 wt. % Si, and 0.175 wt. % Cu. 316SS underwent uniform corrosion during the 80% bentonite/20% Opalinus Clay isothermal, 300 °C experiments. Post-reaction 316SS formed a smectite dominated interface product (Figure 25). The primary type smectite associated with the steel surface appears to be an Fe-saponite. Smectite expands to 16.8 Å (with 002 at 8.44 Å) upon ethylene glycol saturation suggesting no significant amount of mixed-layering is present. Pentlandite ($(Ni,Fe)_9S_8$) also formed concurrently with the smectite phase (Figure 25). The smectite morphology tends to be fairly consistent producing a bladed to micaceous habit with a rose-like texture (Figure 26). Chemical analyses of post-reaction 316SS and corrosion products indicate there was significant Fe leaching from the 316SS forming a Cr-enriched steel outer layer. Smectite coatings were enriched in iron most likely from the iron leached from the 316SS (Figure 27). Fe-rich phyllosilicates that formed on steel plates in the ramped experiments have 06ℓ diffraction bands 1.535 (9.210 Å b-parameters), corresponding to a trioctahedral phyllosilicate (Figure 25; Kohyama et al. 1973; Moore and Reynolds 1997). Ni is preferentially sequestered into the sulfide phase. There was no Ni observed in any of the silicate fractions.

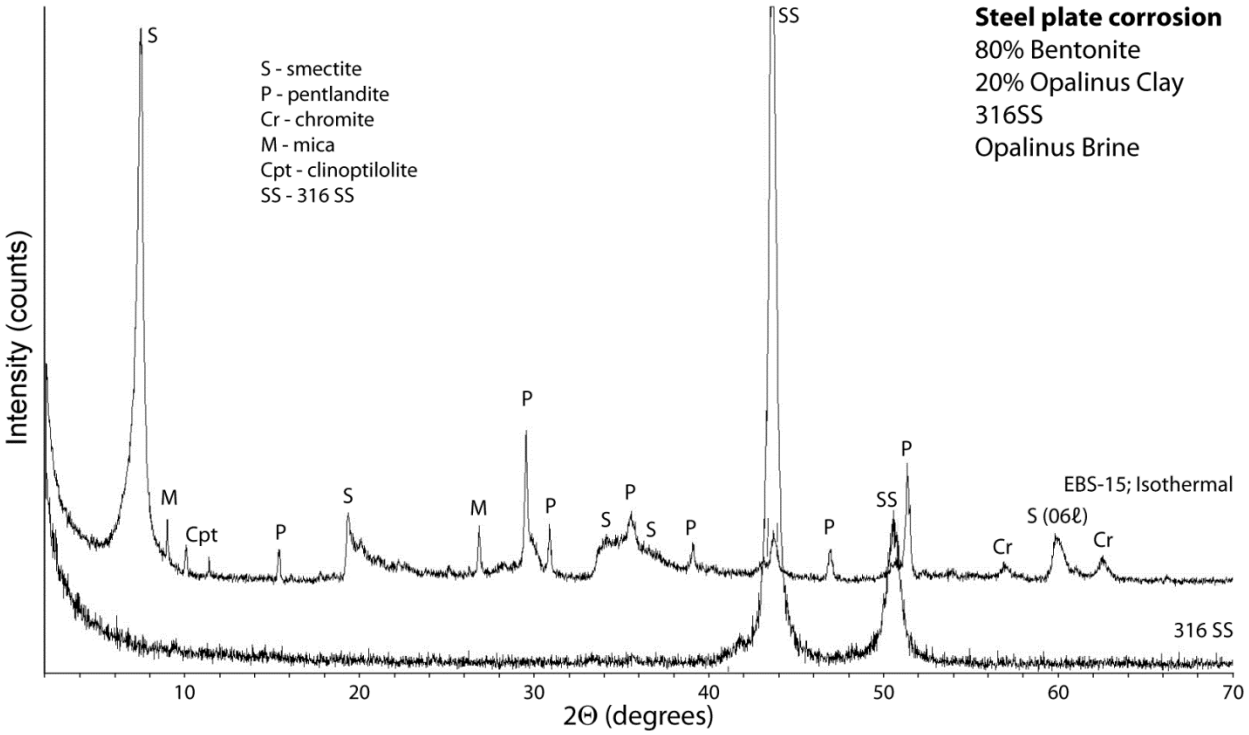

Figure 25. XRD patterns of starting 316SS and corroded 316SS associated with EBS-15. Fe-saponite is the dominate corrosion product associated with steel. Sulfide is the primary sink for leached Ni forming pentlandite. Mica and clinoptilolite are from residual bentonite coating the steel plates.

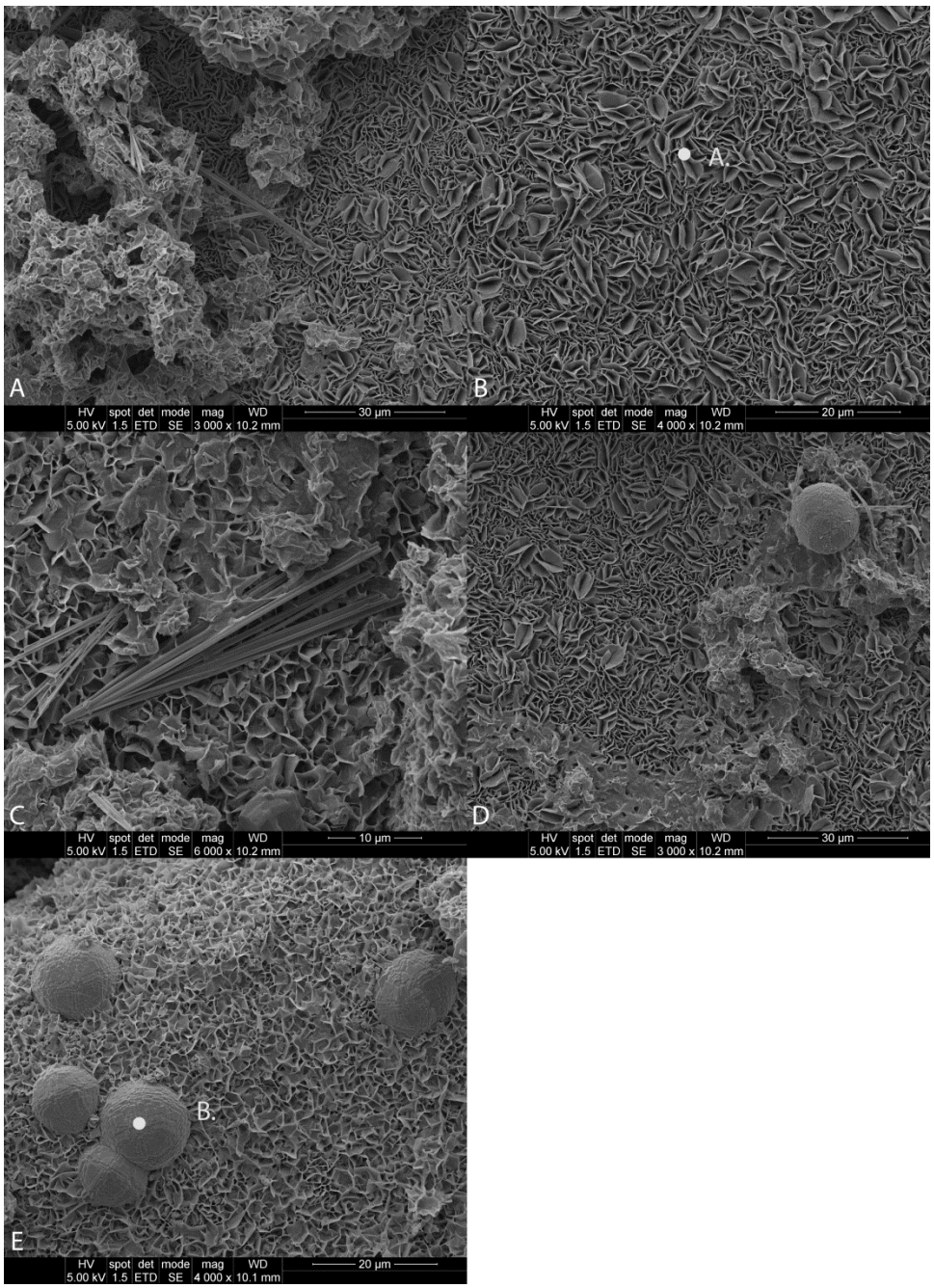

Figure 26. SEM image of 316SS corrosion products associated with Opalinus Clay in EBS-15. A) Fe-saponite corrosion product associated with the 316SS surface partially covered with clay matrix from the bulk system. B) Fe-saponite corrosion product showing typical morphology associated with this type of corrosion. EDX analysis at point A. is presented in Figure 27 A. C) Possible zeolite fibers from the bulk system laying on Fe-saponite. D) Analcime-wairakite particle lying on top of Fe-saponite. E) Analcime-wairakite grown within the Fe-saponite corrosion products suggesting they utilized the 316SS surface as a growth substrate. EDX analysis at point B. is presented in Figure 27 B.

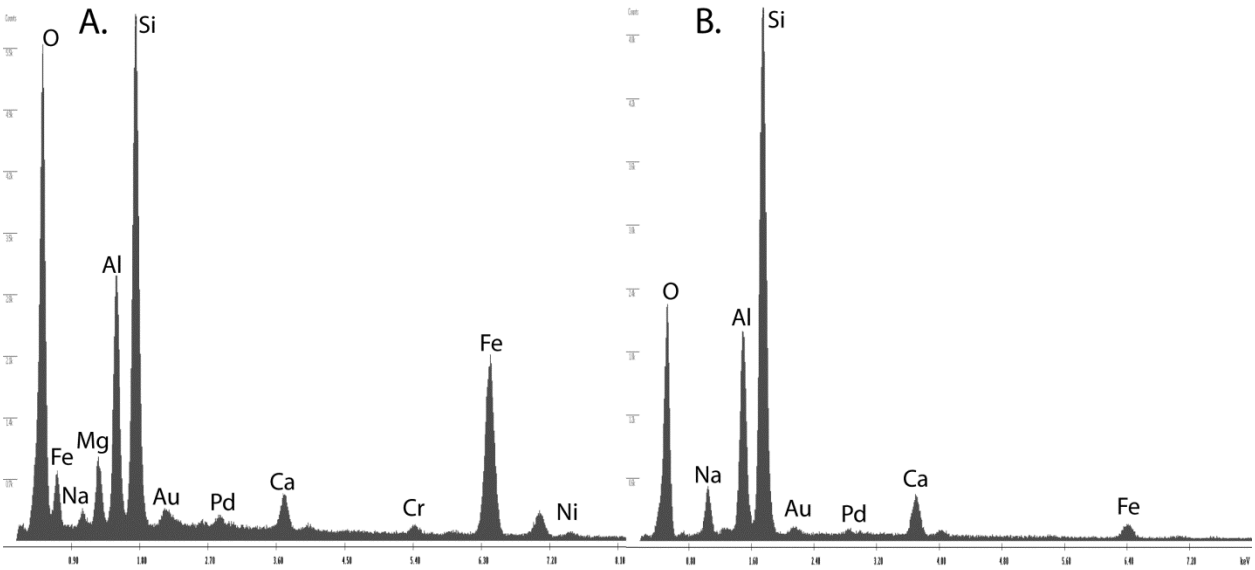

Figure 27. EDX analyses of 316SS corrosion products associated with EBS-15 in Figure 25. A) Fe-saponite on edge to minimize underlying contamination. B) Analcime-wairakite particle imbedded within the Fe-saponite corrosion coating. Many analcime-wairakite particles utilized the 316SS as a growth substrate.

3.6 Capsule Experiments

Mineralogical results from the various capsule experiments are summarized in Tables 10 and 11.

Initial experiments were setup to have an excess of potassium as the primary interlayer cation and a KCl solution to force montmorillonite illitization under the same EBS thermal conditions. Under these conditions a poorly-crystalline R3 illite (0.90-0.95)-smectite was produced with no R0-1 I-S observed. Decreasing potassium to 300 - 559 mg/L (Stripa solution) yielded similar results to the all K system by producing a R3 illite (0.90-0.95)-smectite. Interestingly, none of the K-dominated experiments yielded pure illite even with excess K and experimental times up to 6 months at temperature above 120°C.

Adding a K-saturated montmorillonite to a saturated $CaCl_2$ solution significantly slowed the illitization process. After 6 weeks at 300°C, no smectite illitization was observed, but after six

months an R0 illite (0.36)-smectite was produced. Lowering the $CaCl_2$ concentration, does little to the illitization rates, but does produce mordenite in addition to the R0 illite (0.37)-smectite.

Alternatively, adding a Ca-saturated montmorillonite to a saturated KCl solution does not significantly alter the illitization rates compared to the K-dominated system by producing a R3 illite (0.95)-smectite. Diluting the $CaCl_2$ concentration by a third produced a less ordered illitized product (R1 illite (0.72)-smectite).

Experiments with WY bentonite without any processing yielded similar results to the other EBS experiments. WY bentonite in contact with Stripa or $CaCl_2$ solutions yielded no illitization producing 100% expandability. However, using a KCl solution, R3 illite (0.95)-smectite is produced.

$AlCl_3$ and citric acid additions to the KCl and $CaCl_2$ solutions completely dissolved the montmorillonite fractions and precipitated kaolinite, halloysite, and amorphous materials. Adding various types of host rock components (i.e., Montana illite, Montana illite-smectite, Grimsel granodiorite, K-feldspar (orthoclase), albite, and muscovite) had a negligible effect on smectite illitization.

	Clay Type	Solution Type	Run temp, °C	Run time	°2θ 001	002	003	005	Δ°2θ 002/003	Expandable %	Mineralogy
CAP-1	-2 µm, K-Bentonite	Stripa V2.3	300	6 weeks		ClayStrat+					R3 illite(0.95)-smectite
CAP-2	-2 µm, K-Bentonite	3,550 mg/L KCl	300	6 weeks		ClayStrat+					R3 illite(0.95)-smectite
CAP-3	-2 µm, K-Bentonite	8,130 mg/L $CaCl_2$	300	6 weeks	5.20	10.31	15.62	26.15	**5.31**	97	R0 illite(0.03)-smectite R0 illite(0.16)-smectite
CAP-4	WY Bentonite	Stripa V2.3	300	6 weeks	5.20	10.39	15.70	26.30	**5.31**	97	R0 illite(0.03)-smectite
CAP-5	WY Bentonite	3,550 mg/L KCl	300	6 weeks		ClayStrat+					R3 illite(0.95)-smectite
CAP-6	WY Bentonite	8,130 mg/L $CaCl_2$	300	6 weeks	5.19	10.37	15.61	26.08	**5.24**	101	smectite
CAP-11	-2 µm, K-Bentonite	K-Al brine	300	6 weeks							kao, halloy, amph
CAP-12	-2 µm, K-Bentonite	Ca-Al brine	300	6 weeks							kao, halloy, amph
CAP-13	-2 µm, K-Bentonite	8,130 mg/L $CaCl_2$	300	6 weeks							kao, halloy, amph
CAP-14	WY Bentonite	K-Al brine	300	6 weeks							kao, halloy, amph
CAP-15	WY Bentonite	Ca-Al brine	300	6 weeks							kao, halloy, amph
CAP-16	WY Bentonite	K-Al Citric	300	6 weeks							kao, halloy, amph
CAP-17	WY Bentonite	Ca-Al Citric	300	6 weeks							kao, halloy, amph
CAP-18	-2 µm, K-Bentonite	Ca-Al brine	300	6 weeks							kao, halloy, amph
CAP-19	WY Bentonite; 5% IMt-2	Stripa V2.3	300	6 weeks	5.16	10.33	15.59	26.2	**5.26**	100	smectite
CAP-20	WY Bentonite; 15% IMt-2	Stripa V2.3	300	6 weeks	5.15	10.32	15.60	26.16	**5.28**	99	smectite
CAP-22	WY Bentonite; 5% ISMT	Stripa V2.3	300	6 weeks	5.21	10.38	15.7		**5.32**	97	R0 illite(0.03)-smectite
CAP-23	WY Bentonite; 15% ISMT	Stripa V2.3	300	6 weeks							n.d.
CAP-24	WY Bentonite; 25% ISMT	Stripa V2.3	300	6 weeks							n.d.

Table 10. Mineralogical results from capsule experiments with a brief reaction condition summary. Expandability was determine by the Δ°2θ method, but more complicated illite-smectite was model using ClayStrat+.

	Clay Type	Solution Type	Run temp, °C	Run time	°2θ 001	°2θ 002	°2θ 003	°2θ 005	Δ°2θ 002/003	Expand %	Mineralogy
CAP-26	-2 µm, K-Bentonite	3,550 mg/L KCl	300 to 120	6 months		ClayStrat+					R3 illite(0.95)-smectite
CAP-27	-2 µm, K-Bentonite	1,183 mg/L KCl	300 to 120	6 months		ClayStrat+					R3 illite(0.95)-smectite
CAP-28	-2 µm, K-Bentonite	8,130 mg/L $CaCl_2$	300 to 120	6 months	5.32	10.11	16.19		**6.08**	64	R0 illite(0.36)-smectite
CAP-29	-2 µm, K-Bentonite	2,710 mg/L $CaCl_2$	300 to 120	6 months	5.32	10.14	16.12	26.66	**5.98**	67	R0 illite (0.37)-smectite; mord
CAP-31	WY Bentonite	3,550 mg/L KCl	300 to 120	6 months		ClayStrat+					R3 illite(0.95)-smectite
CAP-32	WY Bentonite	1,183 mg/L KCl	300 to 120	6 months		ClayStrat+					R3 illite(0.95)-smectite
CAP-33	WY Bentonite	8,130 mg/L $CaCl_2$	300 to 120	6 months	5.25	10.55	15.89	26.7	**5.34**	96	R0 illite(0.04)-smectite
CAP-34	WY Bentonite	2,710 mg/L $CaCl_2$	300 to 120	6 months	5.27	10.56	15.91	26.69	**5.35**	95	R0 illite(0.05)-smectite; mord
CAP-36	-2 µm, Ca-Bentonite	3,550 mg/L KCl	300 to 120	6 months		ClayStrat+					R3 illite(0.95)-smectite
CAP-37	-2 µm, Ca-Bentonite	1,183 mg/L KCl	300 to 120	6 months	7.08	9.53	16.96	26.98	**7.43**	28	R1 illite(0.72)-smectite
CAP-39	-2 µm, Ca-Bentonite	2,710 mg/L $CaCl_2$	300 to 120	6 months	5.26	10.53	15.89	26.69	**5.36**	95	R0 illite(0.05)-smectite; mord
CAP-40	-2 µm, Bentonite;10% Kspar	Stripa V2.4	300	6 weeks	5.20	10.37	15.60	26.42	**5.23**	102	smectite
CAP-41	-2 µm, Bentonite20% Kspar	Stripa V2.4	300	6 weeks	5.21	10.40	15.65	26.29	**5.25**	100	smectite
CAP-42	-2 µm, Bentonite;10% alb	Stripa V2.4	300	6 weeks	5.21	10.39	15.62	26.27	**5.23**	102	smectite
CAP-43	-2 µm, Bentonite; 20% alb	Stripa V2.4	300	6 weeks	5.19	10.37	15.62	26.24	**5.25**	100	smectite
CAP-44	-2 µm, Bentonite; 10% musc	Stripa V2.4	300	6 weeks	5.21	10.39	15.66		**5.27**	99	smectite
CAP-45	-2 µm, Bentonite; 20% musc	Stripa V2.4	300	6 weeks	5.22	10.39	15.68		**5.29**	98	smectite
CAP-46	-2 µm, Bentonite; 10% Grimsel	Stripa V2.4	300	6 weeks	5.21	10.40	15.69	26.27	**5.29**	98	smectite
CAP-47	-2 µm, Bentonite; 20% Grimsel	Stripa V2.4	300	6 weeks	5.23	10.38	15.74		**5.36**	95	R0 illite(0.05)-smectite
CAP-48	-2 µm, Bentonite; 30% Grimsel	Stripa V2.4	300	6 weeks	5.19	10.36	15.65	26.34	**5.29**	98	smectite

Table 11. Mineralogical results from capsule experiments with a brief reaction condition summary. . Expandability was determine by the Δ°2θ method, but more complicated illite-smectite was model using ClayStrat+.

4. Discussion

4.1 Bentonite Experiments

4.1.1 Layer Charge. To better determine if any layer charge increase took place during the EBS experiments, a series of cation exchanges was performed followed by ethylene glycol saturation. Smectite swelling is the competing effects between the interlayer cation hydration energy (hydration-repulsion) and the Coulombic attractive forces between negatively-charged 2:1 layers and positively-charged interlayer cations (Laird, 1996; 2006). When Coulombic attractive forces dominate over hydration-repulsion collapse of the interlayer spaces occurs. Collapse can be cause by several possible scenarios, increased layer charge (i.e., illitization), increased interlayer cation charges (i.e., interlayer exchange reactions), or decreased interlayer cation hydration energy (i.e., interlayer exchange reactions). Alternatively, swelling occurs when the hydration-repulsion dominates over the Coulombic attractive forces.

The purpose of these cation exchanges was to exchange in different cations with differing hydration energies. If there was an increase in layer charge, but the Coulombic attraction is not enough to overcome the hydration energy of the dominant interlayer cation (Na^+ @ -411 kJ mol^{-1}), then the material should fully expand upon ethylene glycol saturation. However, performing exchanges with the same reaction material with cations that have lower hydration energies (i.e., K^+ @ -337 kJ mol^{-1}) or with cations that have a higher valence charge (i.e., Ca^{2+} -1,593 kJ mol^{-1}) and the interlayers do not fully expand upon ethylene glycol saturation, then there was an increase in the 2:1 layer charge.

Upon saturation with K^+, the montmorillonite peaks broadened and lost about 4 – 7 % expandability. Compared to the starting K-exchanged montmorillonite, there was no significant difference in expandable material. This suggests that the starting montmorillonite has about 7% of the interlayer spaces with a high-layer charge. This same trend is observed with the Ca^{2+} and Li^+ saturated reaction products. It is evident that there is variation in the layer charge within the starting montmorillonite, but the current EBS reaction conditions do not significantly alter the layer charges or charge distribution. This is also confirmed by the CEC measurement showing no change in CEC values between all reaction products and the starting montmorillonite.

4.1.2 Mineral Evolution. There was no evidence of illite-smectite mixed-layering during the six-month cooling experiment where montmorillonite was heated to 300°C for four months. This is consistent with the other EBS experiments in our Na-dominated hydrothermal systems. Much of the illitization concepts related to a Na-rich systems have been previously discussed (Caporuscio et al., 2013; Cheshire et al., 2014a; 2014b), but is repeated here as it applies to the six-month system.

Smectite-to-illite transformation is not well understood and probably follows several different reaction pathways, i.e. solid-state transformation and dissolution-precipitation (Güven 2001; Dong 2005; Zhang et al. 2007). These different reaction mechanisms may be due to different geological or experimental conditions, including variables such as water/rock ratio, fluid composition, redox state, occurrence of microbial organisms, and presence or absence of organic matter (Small et al. 1992; Small 1993; Güven 2001; Dong 2005; Zhang et al. 2007). Solid-state transformation may be operative in closed systems with a low water/rock ratio, whereas, dissolution-precipitation may be the dominant mechanism in open systems with high water/rock ratios (Zhang et al. 2007). In the current experiments, it appears that two major parameters are preventing smectite-to-illite alteration: alkali and silica solution compositions.

Current experimental results are consistent with other experimental data showing that a limited supply of K^+ along with a relatively high Na^+ activity significantly decreases dioctahedral smectite illitization rates (Eberl and Hower 1977; Eberl 1978, Eberl et al. 1978; Roberson and Lahann 1981; Mosser-Ruck et al. 1999). Their studies also show that, in general, dioctahedral smectites with low hydration-energy interlayer-cations (e.g., K^+, Rb^+, Cs^+) are more susceptible to smectite-to-illite alteration reaction compared to dioctahedral smectites with higher hydration-energy interlayer-cations (e.g., Na^+, Ca^{2+}, Mg^{2+}). These results are consistent with capsule experiments from the current work. However, the presence of a Na-rich system does not preclude smectite illitization. There have been numerous occurrences of illite and illite/smectite occurring in natural or experimental systems that are Na-dominated (Bannister 1943; Frey 1969; Eberl and Hower 1977; Eberl et al. 1978; Whitney and Velde 1993; Mosser-Ruck et al. 1999; Środoń 1999). But, in all these cases, either the temperatures exceeded 300°C or there was a significant potassium source from groundwater or coexisting minerals. Temperatures beyond 300°C exceed the upper temperature limits expected for a repository environment and the experimental

temperature from this investigation (Greenburg and Wen 2013). Additionally, Na-bentonites are currently the bentonite of choice for a repository backfill, thereby, providing a K-depleted and Na-enrich system. Even though the aqueous solutions in the current experiments were K-rich, the overall system (bentonite + water) was Na^+ dominant (~ 2,400 mg Na/L) and K^+ poor (~ 1,000 mg K/L). Include Ca^{2+} (~750 mg/L, bentonite + water) in the discussion, the overall (Na^+ + Ca^{2+})/K^+ ratio is greater than 3.0. It is evident that the dominance of Na^+ and Ca^{2+} along with the low abundance of K^+ does not facilitate illite-smectite formation after 45 days at 300°C.

Silica activities in these experiments appear to be controlled partially by silicate mineral dissolution and precipitation, in addition to clinoptilolite to analcime alteration. Solutions saturated with respect to cristobalite probably contributed to illitization retardation in these current experiments. Systems with silica concentrations higher than quartz saturation have been shown to significantly retard illitization rates (Eberl et al. 1978; Lahann and Roberson 1980; Abercrombie et al. 1994). Abercrombie et al. (1994) has shown that a K-smectite to be the stable phase, potentially up to 200°C, provided silica activity is higher than ~10^{-2}. It was noted by Abercrombie et al. (1994) that as silica levels decreased, due to quartz precipitation, illitization progressed within the system. Therefore, an environment with silica concentrations saturated with respect to cristobalite at temperatures less than 300°C, such as the current experiments, smectite-to-illite alteration should further be inhibited. However, it is important to consider differences between closed, experimental systems versus geological or repository environments that open to the surrounding environment. Many processes that are observed in a closed, experimental system might be mitigated in an open system where solutes can freely move in and out of the environment.

We have shown that at higher silica activities (i.e., cristobalite saturation) clinoptilolite is altered to a high-silicon analcime under the current experimental conditions. Again, these reactions were observed in the other EBS experiments with extended periods at 300°C. Previous studies (Smyth 1982; Wilkin and Barnes 1998; 2000; Cheshire et al., 2013; 2014a) have linked changes in Na, Al, and Si activities with the alteration of clinoptilolite by analcime. However, experimental work (T < 300°C) from Wilkin and Barnes (1998) indicate silica activity influences clinoptilolite alteration by affecting the reaction affinity rather than controlling the reaction equilibrium. Wilkin and Barnes (1998) also show that analcime can form in an environment

saturated with respect to cristobalite provided there is a sufficient change in the Na and/or Al activities.

The effect on the repository due the changes in the system's silica phases and concentrations appears to be a significant issue regarding the repository stability and physical properties. Cementation via silica precipitation is believed to pose the greatest risks to the repository stability and isolation capability compared other mineral reaction (Pusch et al. 1998). Silica precipitation has the potential to weld the smectite lamellae together and reduce the smectite expandability (Pusch et al. 1998; Pusch 2001). The primary mechanism for silica liberation includes smectite illitization, silica/silicate dissolution/saturation, and zeolite alteration.

Production of $H_2S_{(aq,g)}$ is most likely related to pyrite solubility in a chloride-bearing solution (Crerar et al. 1978; Ohmoto et al. 1994). The highly reducing nature of the experimental system easily preserves the $H_2S_{(aq,g)}$ species. Sulfide-induced corrosion of the waste canisters is the primary concern in repository systems (Börjesson et al. 2010). The Swedish Nuclear Fuel and Waste Management Company (SKB) have emplaced fairly strict sulfur specifications (sulfide content < 0.5 wt. %; total sulfur < 1 wt. %) for the bentonite buffer used in their repositories (Börjesson et al. 2010).

4.1.3 Wet vs. Dry Experiments. Dry system kinetics and mineral solubility are highly restricted. Many of the chemical reactions observed in the wet system (9:1 water: rock systems) either do not take place or are restricted in the dry (~ 15 wt. %) system. Pyrite does not undergo decomposition and clinoptilolite undergoes limited dissolution with limited analcime formation. These conditions are more realistic to a repository at 300 °C, because bentonite blocks or pellets typically have ~10 – 20 wt. % H_2O and would be compressed during the repository lifetime. It is evident that reaction kinetics are accelerated under water saturation due to increased ion mobility and minerals' saturation limits.

4.1.4 Heating profile. As stated above mineral evolution and geochemical processes are consistent between all three reactions with differing heating profiles. These profiles were designed to mimic the maximum heating profile during a repository's lifetime, with exception to

the duration of each stage: (1) heating from 120°C (2 weeks); 220°C (2 weeks); 300°C (1 week); (2) isothermal, 300°C (6 weeks); (3) cooling from 300°C (16 weeks), 220°C (4 weeks); 120°C (4 weeks). There were no retrograde reactions observed during the cooling phase. Essentially EBS-10 and EBS-13 show no significant differences between the two reaction products.

It would be expected during the early emplacement of the waste canister that silica saturation, exchange reaction will take place under limited conditions. The relatively dry environment of the early bentonite would significantly restrict the mineral reactions due to the limited ion mobility and early saturation. It is possible that sulfide gas could be generated, but as shown in the 15 wt. % free moisture experiment (EBS-12) pyrite decomposition was not readily observed due to the restricted solubility. As temperatures increase to peak temperature (currently unknown and will be determine during repository design), various possible zeolite reactions (mordenite, laumontite, analcime, wairakite formation) will occur due to the precursor clinoptilolite and volcanic glasses. These zeolite reactions, along with silica saturation reactions, will control the porewater solution chemistry and determine any further mineral alteration. Illite formation can still progress, if a K-source is available, but, K-source stability with respect to the repository conditions will determine the illitization rates. As shown in the capsule experiments, adding K-bearing minerals does not necessarily force illitization; dissolution of those mineral phases has to take place. Illitization thermodynamics and kinetics are strongly tied to the alkali, alkaline earth, silica, and hydrogen (pH) activities; therefore, it is difficult to predict whether illitization will occur in a repository. After the high temperature pulse passes and temperatures begin to decrease, retrograde reaction have the potential to further change the high temperature mineralogy. As observed in current work, no significant retrograde reactions took place, but as with any experimental work slow kinetics of such reactions make them difficult to show experimentally. It would be expected silica saturation is maintained at continuing lower temperatures by releasing silica from solution. This in turn should partially cement and fill pores in the bentonite. Retrograde zeolite reactions are expected, but currently the extent of such reaction and types are unknown.

4.1.5 Corrosion in bentonite. Results from these experiments have shown the more dynamic environment associated with this system is at the bentonite-metal interface.

Trioctahedral, Fe-rich saponite are crystallized on steel surfaces forming a reactive substrate with a high surface area compared to the original steel surfaces. Partial dissolution of the steel plates contributing ferrous iron into a fluid phase with silica and aluminum facilitates Fe-saponite (smectite) crystallization (Figure 28). Liberated Ni is preferentially is crystallized in the sulfide phases forming pentlandite ($(Fe,Ni)_9S_8$) and millerite (NiS). Oxidative leaching of Fe and Ni forms a chromite $(Cr_{1.04},Fe_{0.96})(Fe_{0.69},Ni_{0.31})O_4$ passivation layer on the outer surface of the 316SS plates, restricting corrosion rates (0.1 $\mu m \cdot d^{-1}$ stainless steel) compared to non-alloyed metals (0.6 $\mu m \cdot d^{-1}$ low-carbon steel and 0.8 $\mu m \cdot d^{-1}$ copper). Formation mechanism for Fe-saponite is not completely understood for this system. There are two possible scenarios for Fe-saponite formation: 1) direct crystallization in a Fe- and Si-rich solution as a result from bulk mineralogy influences or 2) Fe + montmorillonite interactions breaking down montmorillonite and producing Fe-saponite. The latter mechanism would be a deleterious reaction to the overall repository as montmorillonite is primary mineral in the barrier.

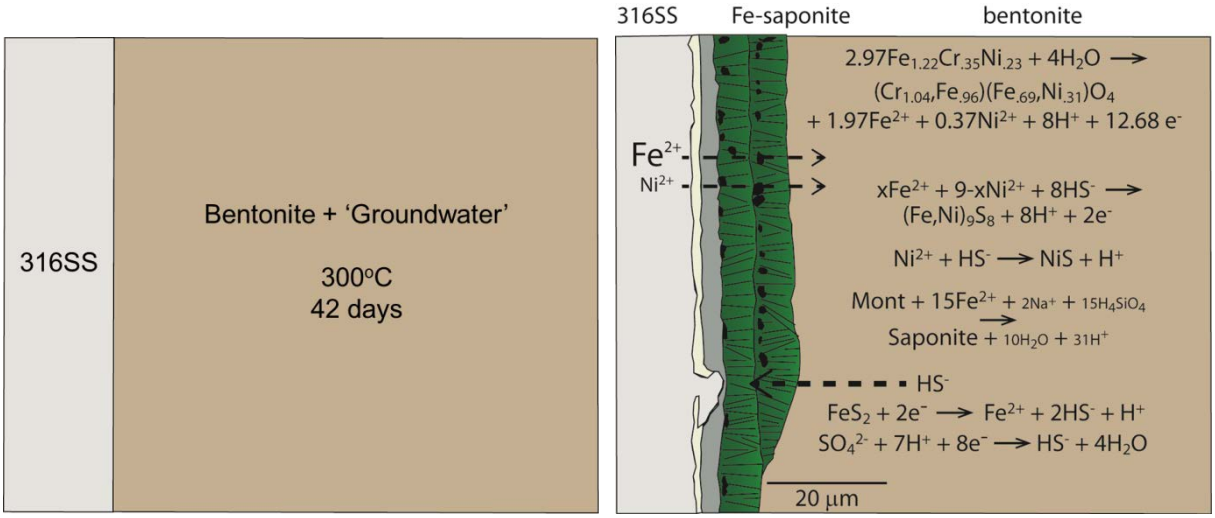

Figure 28. Cartoon of corrosion processes related to EBS experiments containing 316SS.

Fe-phyllosilicates tend to have strong sorption properties towards actinides and other radioactive materials; therefore, they have the potential to provide added barrier properties for actinide containment. The dynamics and reactivity of actinide adsorption need to be incorporated into the long term repository performance evaluation models. However, this work has never been

addressed in repository studies. Inclusion of a reactive, high surface-area canister into used-fuel repositories performance assessments should help provide a viable repository evaluation.

4.2 Opalinus Clay

There are very limited cation exchange reactions associated with the Opalinus Clay and solution chemistry due to no significant amount of smectite. Opalinus Clay is dominated with clay phases (i.e., illite, I-S, kaolinite, and chlorite) that typically do not freely exchange cations.

4.2.1 Zeolite formation. The primary authigenic zeolite in experiments with Opalinus Clay alone differs from the Opalinus Clay experiments with bentonite. These differences appear to be strongly related to the solution chemistry. Bentonite-barring experiments most likely exchanged Ca into the montmorillonite interlayer producing a Ca depleted solution compared to the Opalinus Clay experiments. Solution chemistry associated with the Opalinus clay will remain fairly unchanged unless mineral alteration occurs. The changing of solution chemistry as function of the types of clays in the system appears to indirectly control zeolite stability.

The analcime-wairakite series typically forms through dissolution-precipitation mechanisms through an intermediate mineral or glass phase. In the other EBS experiments, it appears that analcime formed from a direct dissolution-precipitation at the expense of precursor clinoptilolite and volcanic glass. This paragenetic sequence has been previously observed by many other researchers (Smyth, 1982; Masuda et al., 1996; Wilkin and Barnes, 1998). Natural paragenetic sequences suggest that clinoptilolite to analcime may progress at temperatures as low as 75 - 90° C (Smyth 1982; Masuda et al. 1996). Alternatively, work from Wilkin and Barnes (1998; 2000) shows analcime formation kinetics are significantly increased at alkaline pH's (9 - 10), whereas, experiments with circum-neutral pH's showed limited to no analcime formation even at with temperatures > 100° C lasting up to 26 days. It is evident that onset temperatures associated with mineral alterations that pH, along with many other solution chemistry parameters, are important to understand.

Wairakite primarily forms when excess silica is present and typically crystallizes through either an intermediate Ca-mordenite ($CaAl_2Si_{10}O_{24}{\cdot}7H_2O$) or laumontite ($CaAl_2Si_4O_{12}{\cdot}4H_2O$) phase (Ames and Sands, 1958; Jové and Hacker, 1997). In their experimental works, wairakite

lower limit of formation is around 315°C, with an upper limit of 450°C. However, the inclusion of small amount of Na-substitution lowers the formational conditions for wairakite. Additionally, there are limited isomorphous substitutions between analcime and wairakite making Na- or Ca-enriched end members, as opposed of a true intermediate analcime-wairakite (Steiner, 1955; Coombs, 1955; Ames and Sands, 1958). Na-mordenite has an experimental stability range between 190 to 300°C, whereas, Ca-mordenite ranges from 340 to 380°C (Ames and Sand, 1958).

The possible presence of mordenite and laumontite combined with information from Ames and Sand (1958) and Jové and Hacker (1997) strongly suggests that wairakite in this system is probably from the decomposition of mordenite and/or laumontite. Mordenite and laumontite, therefore, appears to have crystallized from the decomposition of kaolinite in the silica and Na/Ca-rich fluids. This reaction would have progressed either until the reaction was quenched or when one of the reactants was depleted and in this case, kaolinite appears to be the limiting resource as it has been completely removed. The presence of Na in our system appears to have lowered the formation temperatures to below 300°C for Na-enriched wairakite.

However, when bentonite is included into Opalinus Clay experiments, the solution chemistry changes significantly forcing the formation of a high-silicon, Ca-enriched analcime. The analcime composition from this experiment is similar to analcime from EBS experiments with bentonite as the only clay. However, it is evident that the reaction mechanisms are very different. In bentonite only reactions, high-silicon analcime crystallized from clinoptilolite and unaltered glass with in the high Na and $SiO_{2(aq)}$ fluids. EBS experiments with 20 wt. % Opalinus Clay much of the original clinoptilolite is preserved, but kaolinite is completely removed. When kaolinite and clinoptilolite are present in a Na/Ca-rich fluid, kaolinite is preferentially recrystallized into either Na/Ca-mordenite and laumontite or analcime.

4.2.2 Clay mineralogy. Following the clay mineral evolution within Opalinus materials is complicated due to the variety of clay minerals present in the Opalinus experimental systems. Two systems were tested: (1) Opalinus Clay and (2) bentonite with 20 wt. % Opalinus Clay. The latter experiment was setup to represent mixing between a repository host rock with a bentonite backfill to determine what effects (if any) the host rock has on the backfill material.

After thermal processing in brine, the Opalinus Clay appears to have an increase in the I-S distribution. The original Opalinus material appeared to have an R3 illite (0.8-0.9)-smectite, but after 300°C for 6 week in an Opalinus brine an R3 illite (0.9)/smectite and a R1 illite (0.7)/smectite was produced. However, illitization in the host rock may not be a major concern as Opalinus Clay is primarily a low-permeable barrier with very limited swelling capacity due to the low amounts of swelling smectite within the Opalinus Clay. The major concern is the reactivity of Opalinus Clay with the bentonite causing alteration to the bentonite constituents. There was negligible illitization within the bentonite fraction in the mixed reaction (EBS-15). This is consistent with the capsule experiments containing a bentonite with a secondary rock phase. It is important to note that these experiments do not preclude the possibility of host rock – bentonite interaction at these temperatures because kinetics may not allow the observation of mineral alterations under the current experimental duration. With any of these experiments representing repository system, kinetics is always an issue that has to be taken into account when interpreting data.

4.2.3 *pH effects*. Many of the reactions described above are strongly influence by the pH of the system. Most mineral reaction rates that are of concern to a repository are increased under high pH systems. Chermak (1992) showed that under pH conditions of 11-13, Na-rectorite was formed at 150 – 200°C within 17 days. Fully formed Na-mica (paragonite) developed after 32 days. Work from Eberl and Hower (1977) and Eberl (1978) do not show illitization until 260 – 400°C at quenched pH's ranging from 4 – 5. These observations are consistent with the current research. The Opalinus Clay experiment starts with a 7.5 – 7.8 solution pH, but during the reaction the pH drops to 4 – 5. The reactions experience significant zeolite reactions, but it appears illitization does not occur under the Na-dominated environment. These high pH dependent reactions will play a major factor within the bentonite backfill near the concrete liners, especially if the concrete used contains significant K^+ concentrations. However, these same reactions should have a minor impact on the bentonite backfill near the waste package because steel and copper corrosion tend to lower the pH.

5. Conclusions

There have been a large number of investigations on bentonite stability under various repository conditions (Madsen 1998; Meunier et al. 1998; Guillaume et al. 2003; Guillaume et al. 2004; Mosser-Ruck et al. 2010; Ferrage et al. 2011). Yet, there remain questions regarding bentonite's overall stability and more importantly whether montmorillonite will remain relatively unaltered through the repository life-time. After initial used-fuel emplacement there will be a pulse of heat flowing into the bentonite buffer producing an environment in which montmorillonite is typically not stable. It would be expected during the early stages of canister emplacement that silica saturation and exchange reactions will take place. However, the relatively dry environment would significantly restrict the mineral reactions due to the limited ion mobility and early saturation. As temperatures increase to peak temperature (currently unknown and will be determine during repository design), various possible zeolite reactions (mordenite, laumontite, analcime, wairakite formation) have the potential to occur if repository conditions shift to the zeolite metamorphic facies (typically starts at 50 - 150 °C; 100 – 500 bars). These zeolite reactions, along with silica saturation reactions, will control the porewater solution chemistry and determine any further mineral alteration. Illite formation can still progress, if a K-source is available, but, K-source stability with respect to the repository conditions will determine the illitization rates. It is expected that the initial heat pulse should start to decay after about 100 to 1,000 years (Wersin et al. 2007). After the high temperature pulse passes and temperatures begin to decrease, retrograde reaction have the potential to further change the high temperature mineralogy. As observed in current work, no significant retrograde reactions took place, but as with any experimental work slow kinetics of such reactions make them difficult to show experimentally. It would be expected silica saturation is maintained at continuing lower temperatures by releasing silica from solution, cementing the bentonite. Retrograde zeolite reactions are expected, but currently the extent of such reaction and types are unknown.

The repository is expected to remain "dry" during the initial 100 to 1,000 years (Wersin et al. 2007). Dry system kinetics and mineral solubility are highly restricted. Many of the chemical reactions observed in the wet system either do not take place or are restricted in the dry system. These conditions are more realistic to a repository at 300°C, because bentonite blocks or

pellets typically have 10 – 20 wt. % H_2O and would be compressed during the repository lifetime. It is evident that reaction kinetics are accelerated under water saturation due to increased ion mobility and minerals' saturation limits.

There have been a number of similar investigations on bentonite stability under various repository conditions and in contact with various metals replicating possible canister compositions (Guillaume et al. 2003; Guillaume et al. 2004; Wilson et al. 2006; Mosser-Ruck et al. 2010; Ferrage et al. 2011). Partial dissolution of the steel plates contributing ferrous iron into a fluid phase with silica and aluminum facilitates Fe-saponite (smectite) crystallization. Liberated Ni is preferentially is crystallized in the sulfide phases forming pentlandite ($(Fe,Ni)_9S_8$) and millerite (NiS). Oxidative leaching of Fe and Ni forms a chromite $(Cr_{1.04},Fe_{0.96})(Fe_{0.69},Ni_{0.31})O_4$ passivation layer on the outer surface of the 316SS plates, restricting corrosion rates (0.1 μm d^{-1} stainless steel) compared to non-alloyed metals (0.6 μm d^{-1} low-carbon steel and 0.8 μm d^{-1} copper). Bentonite not in contact with the steel waste container does not show the formation of these Fe-rich phyllosilicates. The occurrence of Fe-rich phyllosilicates most likely will not form in the bentonite away from the waste container because there is a low abundance of iron in the system. Formation mechanism for Fe-saponite is not completely understood for this system. There are two possible scenarios for Fe-saponite formation: 1) direct crystallization in a Fe- and Si-rich solution as a result from bulk mineralogy influences or 2) Fe + montmorillonite interactions breaking down montmorillonite and producing Fe-saponite. The latter mechanism would be a deleterious reaction to the overall repository as montmorillonite is primary mineral in the barrier.

In this work, we start to consider the impact host rock (i.e., Opalinus Clay from Switzerland) will have on the bentonite barrier. Several mineral alterations were observed in the heating of Opalinus clay. The primary mineral reactions are associated with zeolite formation (i.e., analcime-wairakite, laumontite, and mordenite) at the expense of kaolinite in the host rock. When bentonite is included into Opalinus Clay experiments, the solution chemistry changes significantly forcing the formation of a high-silicon, Ca-enriched analcime. Interpreting clay mineral evolution within Opalinus materials is complicated due to the variety of clay minerals present in the Opalinus experimental systems. However, it does appear that illitization does not occur within the bentonite fraction in the mixed reactions at the current experimental conditions.

It is important to note that these experiments do not preclude the possibility of host rock – bentonite interaction at these temperatures because kinetics may not allow the observation of mineral alterations under the current experimental duration. With any of these experiments representing repository system, kinetics is always an issue that has to be taken into account when interpreting data.

6. FY14 – FY15 Experimental program

Research objectives for the upcoming year will be a natural progression of experimental results obtained in FY13-FY14. For the remainder of FY14, an emphasis will be put on performing detailed geochemical modeling of the bentonite and Opalinus systems. Focus on reactive modeling between the three barrier segments (bentonite-metal, bentonite, and bentonite-host rock) will provide further information on our experimental systems. Additional work for FY14 will be to complete and submit two peer-reviewed publications on 1) the corrosion behavior of steel and copper in contact with bentonite and 2) alteration processes associated with Opalinus Clay at elevated temperatures.

For FY15 we expect to develop three research thrusts. First, we will run a series of high pressure, temperature experiments containing brine – bentonite – metal – host rock at the isothermal, 300°C and six-month cooling heating profiles. Completing our six-month experiments with different types of metals will provide valuable data on the long-term corrosion effects associated with bentonite. We will continue to examine the Opalinus Clay, but would also investigate granitic (i.e., Grimsel granodiorite) and mafic (e.g., basalt or amphibolite) materials if funding is appropriated from Granite EBS studies. Critical information would be gleaned from geochemical and petrographic information, which would allow us to trace mineral transitions through pressure, temperature, time (P, T, t) space. These experiments would be the first to duplicate the events occurring during a thermal pulse and will provide date on irreversible mineral transformations in correlation with various host rock compositions.

Our secondary approach will be to focus on the expanding the experimental geochemical parameters. First evaluating the possible interaction between the radiological elements and bentonite will provide data on the possible retention of radionuclides if a release is to occur. We

will use non-radiological proxies as a substitute for possible alkali earths (i.e., not radioactive Cs^{+}) and actinides present in the waste form (actinide proxies, e.g., Nd^{3+}, Tb^{3+}, or Eu^{3+} for Am^{3+}; Nd^{3+} or Hf^{4+} for Pu^{4+}). Expanding the solution chemistry properties to probe the conditions for illitization and other mineral reactions will provide reaction dynamics that were not considered and can provide kinetic data on important reactions (i.e., SiO_2 concentrations, H_2O content, series of more dilute systems or reactant limited series as to not saturate the system forcing illitization).

A third focus for FY14 – FY15 is the preparation for expected research on the FEBEX-DP international project. We will focus our efforts on designing our experimental program to investigate chemical and physical characteristics of bentonite blocks from the 18 years at 100°C full-scale heater test. We will perform routine mineralogical and geochemical characterizations, but will further test the thermal limits of the system. Sub-cores from each sample provided will be placed in Au-capsules for further heating to temperature ranging from 150 to 300°C to examine the thermal reactivity of the 18 year bentonite. We will examine bentonite-metal, bentonite, and bentonite-cement reactivities. Results from these heating experiments will provide valuable data associated increasing thermal repository limits and diffusional data related to cementitious materials and metals.

To complete all three research focus areas as described about, we would request a total funding of $600K for FY15.

Other research that will be ongoing include: (1) further investigation of Fe-saponite and chalcocite reaction surfaces on steel and copper, respectively, as potential passivating agents, (2) transmission electron microscopy (TEM) examination of the pre- and post-reaction montmorillonite particles to quantify if localized chemical zonation is present within discrete particles, and (3) perform solution calorimetry and differential scanning calorimetry of purified reaction products to produce accurate thermodynamic properties for our experimental system and thereby providing the most accurate thermodynamic and kinetic models.

The proposed lines of study are presented in bullet form below for easy reference.

- Provide information on complete repository thermal pulse event, using long term (6 month) experiments with and without host rocks.

- Performed detailed geochemical modeling of F13-FY15 experimental reaction
- International FEBEX-DP – hydrothermal treatment of FEBEX samples expanding the thermal range in addition to routine mineral/geochemical interrogations.
- Capsule experiments with Cs and proposed non-radioactive actinide proxies (e.g., Nd^{3+}, Tb^{3+}, or Eu^{3+} for Am^{3+}; Nd^{3+} or Hf^{4+} for Pu^{4+}) and expanded parameters (SiO_2 concentrations, longer reaction times, H2O content, series of more dilute systems or reactant limited series (not flood the system forcing illitization) .
- Perform transmission electron microscope (TEM) investigation looking at very local chemical changes in a single montmorillonite particle.
- Purify mineral phases for thermodynamic investigations using solution calorimetry

7. Acknowledgements

We would like to thank Emily Kluk and Diana Brown for XRF analyses. Scanning electron microscopy facilities were provided by Materials Science and Technology group at Los Alamos National Laboratory. Dr. George Mason at the University of Oklahoma was instrumental in the obtaining of EMP analyses. Funding was through the Department of Energy's Used Fuel Disposition Campaign.

8. References

Abercrombie, H.J., Hutcheon, I.E., Bloch, J.D., and de Caritat, P. (1994) Silica activity and the smectite-illite reaction. Geology, 22, 539-542.

Ames, L.L. and Sand, L.B. (1958) Hydrothermal synthesis of wairakite and calcium-mordentite. *The American Mineralogist*, 43, 476-480.

Bannister, R.A. (1943) Brammalite (sodium-illite) a new mineral from Llandebie, South Wales. Mineralogical Magazine, 26, 304-307.

Börjesson, L., Gunnarsson, D., Johannesson, L-E., and Jonsson, E. (2010) Design, production and initial state of the buffer. Svensk Kärnbränslehantering Technical Report, TR-10-15, pp. 89.

Burgess, J. (1978) Metal Ions in Solution. John Wiley & Sons, Inc. pp. 481.

Busenberg, E. and Clemency, C.V. (1973) Determination of the cation exchange capacity of clays and soils using an ammonia electrode. *Clays and Clay Minerals*, 21, 213-217.

Caporuscio, F.A., Cheshire, M.C., Rearick, M.S., Jove-Colon, C., and McCarney, M.K. (2013). EBS Report - LANL Experimental update of buffer/backfill at elevated P,T. FCRD-USED-2013-000207.

Chermak, J.A. (1992) Low temperature experimental investigation of the effect of high pH NaOH solutions on the Opalinus Shale, Switzerland. *Clays and Clay Minerals*, 40, 650-658.

Cheshire, M.C., Caporuscio, F.A., Jové-Colón, C., and McCarney, M.K. (2013) Alteration of clinoptilolite into high-silica analcime within a bentonite barrier system under used nuclear fuel repository conditions. *Proceeding from the 14th International High-Level Radioactive Waste Management Conference*, 410-415.

Cheshire, M.C., Caporuscio, F.A., Jove-Colon, C., and McCarney, M.K. (2014a) Bentonite Clay Evolution at Elevated Pressures and Temperatures: An experimental study for generic nuclear repositories. *In Press, American Mineralogist*.

Cheshire, M.C., Hardin, E., Caporuscio, F.A., Jove-Colon, C., and McCarney, M.K. (2014b) Geochemical Investigation in an Effort to Increase Bentonite Barrier's Thermal Load Capacity to Accommodate 32-PWR Dual Purpose Canisters. *Proceedings from the International Conference on the Performance of Engineered Barriers*, 185-190.

Chipera, S.J. and Bish, D.L. (2002) FULLPAT: a full-pattern quantitative analysis program for X-ray powder diffraction using measured and calculated patterns. *Journal of Applied Crystallography*, 35, 744–749.

Chung, F.H. (1974) Quantitative interpretations of X-ray diffraction patterns of mixtures. I. Matrix flushing method for quantitative multicomponent analysis. *Journal of Applied Crystallography*, 7, 519-525.

Coombs, D.S. (1955) X-ray observations on wairakite and non-cubic analcime. *Mineralogical Magazine*, 30, 699-708.

Couture, R.A. (1985) Steam rapidly reduces the swelling capacity of bentonite. *Nature*, 318, 50-52.

Crerar, D.A., Susak, N.J., Borcsik, M., and Schwartz, S. (1978) Solubility of the buffer assemblage pyrite + pyrrhotite + magnetite in NaCl solution from 200 to 350°C. Geochimica et Cosmochimica Acta, 42, 1427-1437.

Dong, H. (2005) Interstratified illite-smectite: A review of contributions of TEM data to crystal chemical relation and reaction mechanisms. Clay Science, 12, Supplement 1, 6-12.

Eberl, D. and Hower, J. (1977) The hydrothermal transformation of sodium and potassium smectite into mixed-layer clay. *Clays and Clay Minerals*, 25, 215-227.

Eberl, D. (1978) Reaction series for dioctahedral smectites. *Clays and Clay Minerals*, 26, 327-340.

Eberl, D., Whitney, G., and Khourym, H. (1978) Hydrothermal reactivity of smectite. *American Mineralogist*, 63, 401-409.

Eberl, D.D., Velde, B., and McCormick, T. (1993) Synthesis of illite-smecite from smectite at Earth surface temperatures and high pH. *Clay Minerals*, 28, 49-60.

Ferrage, E., Vidal, O., Mosser-Ruck, R., Cathelineau, M., and Cuadros, J. (2011) A reinvestigation of smectite illitization in experimental hydrothermal conditions: Results

from X-ray diffraction and transmission electron microscopy. *American Mineralogist*, 96, 207-223.

Frape, S.K., Blyth, A., Blomqvist, R., McNutt, R.H., and Gascoyne, M. (2003) Deep Fluids in the Continents: II. Crystalline Rocks, Treatise on Geochemistry, 5, J. I. Drever, ed., 541-580.

Frey, M. (1969) A mixed-layer paragonite/phengite of low-grade metamorphic origin. Contribution to Mineralogy and Petrology, 24, 63-65.

Greenburg, H.R. and Wen, J. (2013) Repository layout and host rock thermal gradient trade study for large waste packages in clay/shale: Using the DSEF thermal analytical model. LLNL-TR-639869-DRAFT, pp. 38.

Guillaume, D., Neaman, A., Cathelineau, M., Mosser-Ruck, R., Peiffert, C., Abdelmoula, M., Dubessy, J., Villieras, F., Baronnet, A., and Michau, N., (2003) Experimental synthesis of chlorite from smectite at 300 °C in the presence of metallic Fe. *Clay Minerals*, 38, 281-302.

Guillaume, D., Neaman, A., Cathelineau, M., Mosser-Ruck, R., Peiffert, C., Abdelmoula, M., Dubessy, J., Villieras, F., and Michau, N., (2004) Experimental study of the transformation of smectite at 80 to 300 ^{o}C in the presence of Fe oxides. *Clay Minerals*, 39, 17-34.

Güven, N. (2001) Mica structure and fibrous growth of illite. Clays and Clay Minerals, 49, 189-196.

International Atomic Energy Agency (IAEA) (2000) Multi-purpose container technologies for spent fuel management. IAEA Technical Document, IAEA-TECDOC-1192, pp. 56.

Jové, C. and Hacker, B.R. (1997) Experimental investigation of laumontite → wairakite + H2O: A model diagenetic reaction. *American Mineralogist*, 82, 781-789.

Jové-Colón, C. F., Caporuscio, F. A., Levy, S. S., Sutton, M., Blink, J., Greenberg, H. R., Fratoni, M., Halsey, W. G., Wolery, T. J., Rutqvist, J., et al. (2011) Disposal Systems Evaluations and Tool Development - Engineered Barrier System (EBS) Evaluation (Fuel Cycle Research and Development). Sandia National Laboratory, FCRD-USED-2011-000132, 1-192.

Kohyama, N., Shimoda, S., and Sudo, T. (1973) Iron-rich saponite (ferrous and ferric forms). Clays and Clay Minerals, 21, 229-237.

Lahann, R.W. and Roberson, H.E. (1980) Dissolution of silica from montmorillonite: effect of solution chemistry. Geochimica et Cosmochimica Acta, 44, 1937-1943.

Laird, D.A. (1996) Model for crystalline swelling of 2:1 phyllosilicates. *Clays and Clay Minerals*, 44, 553-559.

Laird, D.A. (2006) Influence of layer charge on swelling of smectites. *Applied Clay Science*, 34, 74-87.

Madsen, F.T. (1998) Clay mineralogical investigations related to nuclear waste disposal. *Clay Minerals*, 33, 109-129.

Masuda, H., O'Neil, J.R., Jiang, W-T, and Peacor, D.R. (1996) Relation between interlayer composition of authigenic smectite, mineral assemblages, I/S reaction rate and fluid composition in silicic ash of the Nankai Trough. *Clays and Clay Minerals*, **44**, 443-459.

Meunier, A., Velde, B., and Griffault, L. (1998) The Reactivity of Bentonites: a Review. An Application to Clay Barrier Stability for Nuclear Waste Storage. *Clay Minerals*, 33, 187-196.

Moore, D. M. and Reynolds, R.C. (1997) X-ray Diffraction and the Identification and Analysis of Clay Minerals. Oxford University Press, New York, New York, pp. 377.

Mosser-Ruck, R., Cathelineau, M., Baronnet, A., and Trouiller, A. (1999) Hydrothermal reactivity of K-smectite at 300 °C and 100 bar: dissolution-crystallization process and non-expandable dehydrated smectite formation. *Clay Minerals*, 34, 275-290.

Mosser-Ruck, R., Cathelineau, M., Guillaume, D., Charpentier, D., Rousset, D., Barres, O., and Michau, N. (2010) Effects of Temperature, pH, and Iron/Clay and Liquid/Clay Ratios on Experimental Conversion of Dioctahedral Smectite to Berthierine, Chlorite, Vermiculite, or Saponite. *Clays and Clay Minerals*, 58, 280-291

Nutt, M. Voegele, M., Jové-Colón, C.F., Wang, Y., Howard, R., Blink, J., Liu, H.H., Hardin, E., and Jenni, K. (2011) Used fuel disposition campaign disposal research and development road map (Fuel cycle research and development). Sandia National Laboratory, FCRD-USED-2011-000065, 1-121.

Ohmoto, H., Hayashi, K-I, and Kajisa, Y. (1994) Experimental study of the solubilities of pyrite in NaCl-bearing aqueous solutions at 250-350°C. Geochimica et Cosmochimica Acta, 58, 2169-2185.

Pearson, F.J., Arcos, D., Bath, A., Boisson, J.-Y., Fernandez, A.M., Gabler, H.-E., Gaucher, E., Gautschi, A., Griffault, L., Hernan, P., and Waber, H.N. (2003) Mont Terri Project-Geochemistry of water in the Opalinus Clay Formation at the Mont Terri Rock Laboratory. – Reports of the Federal Office for Water and Geology (FOWG), Geology Series No. 5.

Pouchou, J.L. and Pichoir, F. (1985) "PAP" $\phi(\rho z)$ correction procedure for improved quantitative microanalysis. Microbeam Analysis. Ed. Armstrong, J.T. San Francisco Press, pp. 104-106.

Pusch, R. (1979) Highly compacted sodium bentonite for isolating rock-deposited radioactive waste products. Nuclear Technology, 45, 153-157.

Pusch, R (2008) Geological Storage of Radioactive Waste. Springer-Verlag, Berlin, Germany, pp. 379.

Roberson, H.E. and Lahann, R.W (1981) Smectite to illite conversion rates: Effects of solution chemistry. Clays and Clay Minerals, 29, 129-135.

Seyfried, J.R., Janecky, D.R., and Berndt, M.E. (1987) Rocking autoclaves for hydrothermal experiments II. The flexible reaction-cell system. Hydrothermal Experimental Techniques. Eds. Ulmer, G.C. and Barnes, H.L. John Wiley & Sons, pp. 216 – 239.

Small, J.S., Hamilton, D.L., and Habesch, S. (1992) Experimental simulation of clay precipitation within reservoir sandstones 2: Mechanism of illite formation and controls on morphology. Journal of Sedimentary Petrology, 62, 520-529.

Small, J.S. (1993) Experimental determination of the rates of precipitation of authigenic illite and kaolinite in the presence of aqueous oxalate and comparison to the K/Ar ages of authigenic illite in reservoir sandstones. Clays and Clay Minerals, 41, 191-208.

Smyth, J.R. (1982) Zeolite stability constraints on radioactive waste isolation in zeolite-bearing volcanic rocks. *Journal of Geology*, 90, 195-201.

Środoń, J. (1980) Precise identification of illite/smectite interstratifications by X-ray powder diffraction. *Clays and Clay Minerals*, 28, 401-411.

Środoń, J. (1999) Nature of mixed-layer clays and mechanisms of their formation and alteration. Annual Review of Earth and Planetary Sciences, 27, 19-53.

Steiner, A. (1955) Wairakite, the calcium analogue of analcime, a new zeolite mineral. *Mineralogical Magazine*, 30, 691-698.

Wersin, P., Johnson, L.H., and McKinley, I.G. (2007) Performance of the bentonite barrier at temperatures beyond 100°C: A critical review. *Physics and Chemistry of the Earth*, 32, 780-788.

Whitney, G. and Velde, B. (1993) Changes in particle morphology during illitization: An experimental study. Clays and Clay Minerals, 41, 209-218.

Wilkin, R.T. and Barnes, H.L. (1998) Solubility and stability of zeolites in aqueous solution: I. Analcime, Na-, and K-clinoptilolite. *American Mineralogist*, 83, 746-761.

Wilkin, R.T. and Barnes, H.L. (2000) Nucleation and growth kinetics of analcime from precursor Na-clinoptilolite. *American Mineralogist*, 85, 1329-1341.

Zhang G., Kim, J., Dong, H., and Sommer, A. (2007) Microbial effects in promoting the smectite to illite reaction: Role of organic matter intercalated in the interlayer. American Mineralogist, 92, 1401-1410.

Appendix A

EMP standards and oxide detection limits for silicate analyses

Phlogopite (Synthetic): MgO = 0.02 wt.% , F = 0.11 wt.%
Albite (Amelia, NC, U.S.A, Rutherford mine): Na_2O = 0.02 wt.%
Labrodorite (Chihuahua, Mexico): Al_2O_3 = 0.02 wt.%, SiO_2 = 0.02 wt.%, CaO = 0.01 wt.%
Tugtupite (Greenland): Cl = 0.01 wt.%
Adularia (St. Gotthard, Switzerland): K_2O = 0.01 wt.%
Titanite glass (Penn State): TiO_2 = 0.02 wt.%
MagnesioChromite (Synthetic): Cr_2O_3 = 0.04 wt.%
Rhodonite (unknown locality): MnO = 0.02 wt.%
Augite (unknown locality): FeO = 0.02 wt.%
Liebenbergite (synthetic): NiO = 0.06 wt.%
Gahnite: ZnO = 0.05 wt.%

Appendix B:
Electron Microprobe Mineral Data

All data are presented as wt. % of the oxide.

	SiO_2	TiO_2	Al_2O_3	Cr_2O_3	FeO*	MnO	MgO	NiO	ZnO	CaO	Na_2O	K_2O	F	Cl	Total
Clinoptilolite															
EBS4-Cpt1-1	69.54	0.06	14.91	0.02	2.68	0.00	0.85	0.00	0.00	0.68	1.60	0.84	0.00	0.04	91.21
EBS4-Cpt2-1	74.50	0.00	13.08	0.00	0.16	0.00	0.13	0.00	0.00	1.55	0.32	0.48	0.00	0.01	90.24
AVE	**72.02**	**0.03**	**13.99**	**0.01**	1.42	**0.00**	**0.49**	**0.00**	**0.00**	**1.12**	**0.96**	**0.66**	**0.00**	**0.03**	**90.73**
EBS9-Cpt1-1	70.04	0.05	15.11	0.00	0.99	0.01	0.57	0.00	0.01	1.94	1.11	0.31	0.00	0.03	90.17
Unknown Species															
EBS4-Anl1-1	54.03	0.04	13.53	0.00	2.21	0.01	0.81	0.01	0.00	11.41	1.47	0.66	0.26	0.02	84.34
EBS4-unk1-1	37.85	0.05	10.63	0.00	2.02	0.00	0.91	0.00	0.00	24.04	0.62	0.52	0.00	0.40	76.98
EBS7-Cpt1-1	59.65	0.11	15.71	0.00	3.52	0.03	1.58	0.02	0.01	4.26	1.54	0.17	0.13	0.03	86.68
Glass (altered)															
EBS9-gls1-1	75.05	0.01	12.30	0.00	0.15	0.01	0.16	0.00	0.00	1.38	1.89	0.01	0.00	0.02	90.98
EBS11-gls1	72.53	0.00	11.99	0.00	0.19	0.01	0.10	0.00	0.02	1.70	2.29	0.22	0.00	0.00	89.05
EBS12-Gls-1	73.04	0.02	12.58	0.00	0.11	0.00	0.13	0.01	0.00	1.29	2.84	0.15	0.00	0.01	90.16
EBS12-Gls-2	74.83	0.02	12.23	0.00	0.10	0.00	0.15	0.00	0.00	1.31	2.90	0.14	0.00	0.00	91.66
EBS12-Gls-2	72.88	0.01	10.19	0.00	0.08	0.00	0.18	0.00	0.02	1.76	2.12	0.07	0.02	0.01	87.32
EBS12-Gls-3	73.58	0.02	12.40	0.00	0.08	0.00	0.15	0.01	0.04	1.73	3.16	0.17	0.09	0.00	91.39
AVE	**73.58**	**0.02**	**11.85**	**0.00**	0.09	**0.00**	**0.15**	**0.01**	**0.01**	**1.52**	**2.75**	**0.13**	**0.03**	**0.01**	**90.13**

Table B1. Clinoptilolite, unknown phases, and glasses EMP data.

	SiO_2	TiO_2	Al_2O_3	Cr_2O_3	FeO*	MnO	MgO	NiO	ZnO	CaO	Na_2O	K_2O	F	Cl	Total
EBS4-Bt1-1	35.21	5.25	12.93	0.00	28.20	0.21	6.41	0.02	0.09	0.00	0.45	8.48	0.63	0.30	97.84
EBS4-Bt1-2	34.88	5.15	12.91	0.00	28.21	0.20	6.42	0.01	0.08	0.03	0.55	8.39	0.71	0.26	97.46
Ave.	**35.05**	**5.20**	**12.92**	**0.00**	**28.21**	**0.20**	**6.41**	**0.02**	**0.08**	**0.02**	**0.50**	**8.44**	**0.67**	**0.28**	**97.65**
EBS7-Bt1-1	35.36	5.10	13.26	0.00	27.84	0.19	6.38	0.02	0.02	0.03	0.57	8.40	0.82	0.27	97.85
EBS7-Bt1-2	36.03	4.89	13.21	0.01	27.31	0.20	6.24	0.00	0.06	0.02	0.65	8.16	0.82	0.27	97.47
Ave.	**35.69**	**4.99**	**13.23**	**0.00**	**27.58**	**0.20**	**6.31**	**0.01**	**0.04**	**0.03**	**0.61**	**8.28**	**0.82**	**0.27**	**97.66**
EBS9-Bt1-1	38.58	3.92	14.64	0.00	22.65	0.19	7.50	0.00	0.04	0.07	0.59	7.12	0.49	0.23	95.77
EBS9-Bt1-2	37.07	4.22	13.78	0.01	23.81	0.22	7.44	0.01	0.10	0.13	0.38	7.54	0.45	0.23	95.15
Ave.	**37.82**	**4.07**	**14.21**	**0.00**	**23.23**	**0.21**	**7.47**	**0.00**	**0.07**	**0.10**	**0.49**	**7.33**	**0.47**	**0.23**	**95.46**
EBS10-Bt-1	34.81	5.20	12.85	0.00	28.07	0.20	6.46	0.00	0.07	0.03	0.57	8.47	0.68	0.26	97.33
EBS10-Bt-2	34.99	5.06	12.97	0.00	28.08	0.21	6.51	0.00	0.05	0.03	0.61	8.43	0.60	0.27	97.49
EBS10-Bt2-1	35.60	5.03	12.92	0.00	27.56	0.21	6.48	0.01	0.07	0.01	0.48	8.47	0.61	0.25	97.38
EBS10-Bt2-2	34.69	4.93	12.82	0.01	27.01	0.18	6.43	0.00	0.07	0.04	0.57	8.08	0.60	0.25	95.36
Ave.	**35.02**	**5.05**	**12.89**	**0.00**	**27.68**	**0.20**	**6.47**	**0.00**	**0.06**	**0.03**	**0.56**	**8.36**	**0.62**	**0.26**	**96.89**
EBS11-Bt-1	36.65	4.17	13.43	0.00	25.16	0.22	7.36	0.01	0.10	0.04	0.49	8.17	0.70	0.23	96.38
EBS11-Bt-2	36.52	4.24	13.52	0.00	25.63	0.26	7.40	0.01	0.05	0.03	0.56	8.25	0.60	0.24	97.01
Ave.	**36.59**	**4.20**	**13.47**	**0.00**	**25.39**	**0.24**	**7.38**	**0.01**	**0.07**	**0.04**	**0.52**	**8.21**	**0.65**	**0.23**	**96.70**
EBS12-Bt1-1	35.65	4.44	12.72	0.01	25.85	0.29	7.99	0.00	0.06	0.04	0.39	8.57	0.71	0.22	96.58
EBS12-Bt1-2	35.56	4.38	13.12	0.00	25.35	0.28	8.14	0.00	0.07	0.06	0.38	8.29	0.74	0.24	96.24
Ave.	**35.61**	**4.41**	**12.92**	**0.01**	**25.60**	**0.28**	**8.06**	**0.00**	**0.07**	**0.05**	**0.38**	**8.43**	**0.72**	**0.23**	**96.41**

Table B2. Biotite samples from EBS reaction products.

	SiO_2	TiO_2	Al_2O_3	Cr_2O_3	FeO*	MnO	MgO	NiO	ZnO	CaO	Na_2O	K_2O	F	Cl	Total
EBS10-Anl1-1	69.67	0.00	19.12	0.00	0.18	0.00	0.03	0.02	0.00	1.53	4.44	0.06	0.00	0.00	95.05
EBS10-Anl-2	69.83	0.03	18.98	0.00	0.21	0.01	0.05	0.01	0.02	1.13	4.04	0.02	0.03	0.00	94.34
EBS10-Anl-3	69.08	0.01	18.98	0.01	0.23	0.02	0.10	0.00	0.00	1.37	4.37	0.06	0.00	0.00	94.22
EBS10-Anl-4	68.65	0.01	18.89	0.00	0.18	0.03	0.04	0.00	0.01	1.14	5.29	0.01	0.09	0.00	94.28
EBS10-Anl-5	69.37	0.00	18.92	0.00	0.23	0.00	0.05	0.00	0.00	1.15	3.17	0.01	0.00	0.00	92.91
EBS10-Anl-7	69.74	0.00	18.54	0.00	0.16	0.00	0.04	0.00	0.00	1.44	4.56	0.02	0.08	0.02	94.58
EBS10-Anl-8	69.81	0.01	19.96	0.00	0.20	0.00	0.05	0.01	0.00	1.06	3.57	0.02	0.00	0.01	94.69
EBS10-Anl-9	70.03	0.00	19.77	0.00	0.20	0.00	0.04	0.00	0.00	1.35	4.04	0.02	0.12	0.00	95.52
EBS10-Anl-10	71.44	0.13	19.86	0.00	0.60	0.02	0.22	0.01	0.01	0.88	4.42	0.20	0.03	0.01	97.83
EBS10-Anl-11	68.93	0.00	18.98	0.00	0.20	0.00	0.04	0.00	0.00	1.55	3.58	0.05	0.00	0.01	93.34
AVE	**69.66**	**0.02**	**19.20**	**0.00**	**0.24**	**0.01**	**0.06**	**0.01**	**0.00**	**1.26**	**4.15**	**0.05**	**0.03**	**0.01**	**94.68**
Std Dev	**0.77**	**0.04**	**0.48**	**0.00**	**0.13**	**0.01**	**0.06**	**0.01**	**0.01**	**0.22**	**0.61**	**0.06**	**0.05**	**0.01**	**1.34**
EBS11-Anl-1	68.03	0.02	18.52	0.00	0.14	0.00	0.04	0.00	0.01	1.37	4.68	0.04	0.00	0.01	92.85
EBS11-Anl-2	68.06	0.00	18.23	0.02	0.12	0.02	0.04	0.00	0.00	1.34	4.46	0.05	0.00	0.02	92.35
EBS11-Anl-3	68.82	0.00	18.44	0.00	0.16	0.01	0.04	0.00	0.01	1.52	4.49	0.09	0.00	0.00	93.60
EBS11-Anl-4	69.10	0.02	18.79	0.01	0.17	0.00	0.04	0.00	0.00	1.38	3.79	0.04	0.00	0.02	93.35
EBS11-Anl-5	69.10	0.02	18.33	0.00	0.19	0.00	0.06	0.01	0.02	1.33	3.72	0.04	0.05	0.02	92.87
EBS11-Anl-6	70.07	0.03	18.50	0.00	0.17	0.01	0.04	0.01	0.02	1.53	4.28	0.08	0.00	0.01	94.73
EBS11-Anl-7	69.71	0.00	18.86	0.00	0.18	0.01	0.04	0.01	0.02	1.33	4.29	0.04	0.09	0.01	94.56
EBS11-Anl-10	70.21	0.00	18.40	0.00	0.15	0.00	0.02	0.01	0.00	1.55	3.77	0.08	0.00	0.00	94.21
EBS11-Anl-11	68.95	0.04	19.53	0.00	0.43	0.00	0.23	0.00	0.00	0.81	3.74	0.08	0.01	0.02	93.84
EBS11-Anl-13	67.06	0.07	19.47	0.00	0.47	0.01	0.26	0.00	0.02	0.93	3.79	0.13	0.07	0.01	92.26
AVE	**68.91**	**0.02**	**18.71**	**0.00**	**0.22**	**0.01**	**0.08**	**0.00**	**0.01**	**1.31**	**4.10**	**0.07**	**0.02**	**0.01**	**93.46**
Std Dev	**0.98**	**0.02**	**0.46**	**0.01**	**0.12**	**0.01**	**0.09**	**0.00**	**0.01**	**0.25**	**0.38**	**0.03**	**0.03**	**0.01**	**0.88**

Table B3. EMP analyses from analcime.

	SiO_2	TiO_2	Al_2O_3	Cr_2O_3	FeO*	MnO	MgO	NiO	ZnO	CaO	Na_2O	K_2O	F	Cl	Total
EBS11-Anl-8 20u	64.05	0.00	17.76	0.00	0.10	0.00	0.02	0.01	0.00	1.51	8.50	0.10	0.10	0.00	92.11
EBS11-Anl-9 20u	64.70	0.00	17.76	0.00	0.08	0.01	0.01	0.01	0.00	1.46	7.64	0.09	0.00	0.01	91.76
AVE	**64.37**	**0.00**	**17.76**	**0.00**	**0.09**	**0.00**	**0.02**	**0.01**	**0.00**	**1.49**	**8.07**	**0.09**	**0.05**	**0.00**	**91.93**
EBS12-Anl?-1	71.17	0.00	18.61	0.00	0.33	0.01	0.20	0.00	0.00	0.55	1.83	0.05	0.02	0.01	92.76
EBS12-Anl?-2	70.45	0.03	18.66	0.00	0.27	0.01	0.14	0.00	0.00	0.45	4.02	0.04	0.00	0.01	94.08
EBS12-Anl?-3	70.62	0.01	18.97	0.02	0.38	0.02	0.17	0.01	0.00	0.50	3.90	0.02	0.06	0.01	94.66
EBS12-Anl?-4	70.39	0.04	18.69	0.00	0.33	0.01	0.23	0.00	0.03	0.43	3.91	0.12	0.03	0.02	94.21
AVE	**70.66**	**0.02**	**18.73**	**0.01**	**0.33**	**0.01**	**0.18**	**0.00**	**0.01**	**0.48**	**3.41**	**0.06**	**0.03**	**0.01**	**93.93**
Std Dev	**0.35**	**0.02**	**0.16**	**0.01**	**0.04**	**0.00**	**0.04**	**0.01**	**0.01**	**0.05**	**1.06**	**0.05**	**0.03**	**0.01**	**0.82**

Table B4. EMP analyses from analcime.

	SiO_2	TiO_2	Al_2O_3	Cr_2O_3	FeO*	MnO	MgO	NiO	ZnO	CaO	Na_2O	K_2O	F	Cl	Total
EBS7-Afs1-1	65.63	0.01	18.84	0.01	0.16	0.00	0.00	0.02	0.05	0.16	3.39	11.58	0.10	0.00	99.90
EBS9-Afs1-1	65.39	0.01	18.74	0.00	0.18	0.02	0.01	0.01	0.00	0.17	3.46	11.56	0.12	0.00	99.62
EBS10-Afs-1	63.28	0.02	18.43	0.00	0.17	0.00	0.02	0.01	0.00	0.25	2.99	11.19	0.06	0.00	96.40
EBS10-Afs-2	63.71	0.00	18.58	0.00	0.19	0.00	0.00	0.00	0.00	0.27	3.68	10.38	0.00	0.00	96.80
EBS10-Afs3-1	64.91	0.02	18.82	0.01	0.15	0.00	0.00	0.01	0.00	0.19	3.22	11.39	0.03	0.00	98.74
EBS10-Afs-4	65.49	0.00	18.99	0.00	0.18	0.00	0.00	0.03	0.02	0.19	3.24	11.22	0.07	0.00	99.40
AVE	**64.35**	**0.01**	**18.70**	**0.00**	**0.17**	**0.00**	**0.00**	**0.01**	**0.01**	**0.23**	**3.28**	**11.04**	**0.04**	**0.00**	**97.83**
STD DEV	**1.03**	**0.01**	**0.25**	**0.00**	**0.02**	**0.00**	**0.00**	**0.01**	**0.01**	**0.04**	**0.29**	**0.45**	**0.03**	**0.00**	**1.46**
EBS11-Afs-1	65.58	0.01	18.37	0.00	0.14	0.00	0.00	0.00	0.01	0.24	3.71	10.40	0.20	0.00	98.58
EBS11-Afs-2	65.36	0.00	18.52	0.01	0.11	0.01	0.01	0.00	0.00	0.17	3.41	11.39	0.00	0.00	98.97
EBS11-Afs-4	66.72	0.00	18.76	0.00	0.18	0.00	0.01	0.00	0.01	0.17	4.18	10.34	0.03	0.00	100.39
AVE	**65.89**	**0.00**	**18.55**	**0.00**	**0.14**	**0.00**	**0.00**	**0.00**	**0.01**	**0.20**	**3.77**	**10.71**	**0.08**	**0.00**	**99.31**
STD DEV	**0.73**	**0.01**	**0.20**	**0.00**	**0.04**	**0.00**	**0.00**	**0.00**	**0.01**	**0.04**	**0.39**	**0.59**	**0.11**	**0.00**	**0.95**
EBS12-Afs-1	62.89	0.02	18.55	0.02	0.17	0.00	0.00	0.00	0.00	0.17	3.28	11.07	0.00	0.00	96.17
EBS12-Afs-1	63.58	0.01	18.66	0.00	0.19	0.00	0.00	0.00	0.00	0.18	3.26	10.96	0.00	0.01	96.87
EBS12-Afs-2	61.36	0.00	18.67	0.00	0.18	0.00	0.00	0.02	0.00	0.20	3.19	10.03	0.00	0.00	93.64
EBS12-Afs-3	64.53	0.03	18.48	0.01	0.11	0.00	0.00	0.00	0.00	0.15	3.27	11.42	0.00	0.00	98.01
AVE	**63.09**	**0.01**	**18.59**	**0.01**	**0.16**	**0.00**	**0.00**	**0.00**	**0.00**	**0.18**	**3.25**	**10.87**	**0.00**	**0.00**	**96.17**
STD DEV	**1.34**	**0.01**	**0.09**	**0.01**	**0.04**	**0.00**	**0.00**	**0.01**	**0.00**	**0.02**	**0.04**	**0.59**	**0.00**	**0.00**	**1.85**

Table B5. EMP analyses from K-feldspars. Samples with low totals probably had significant Ba contributions.

	SiO_2	TiO_2	Al_2O_3	Cr_2O_3	FeO*	MnO	MgO	NiO	ZnO	CaO	Na_2O	K_2O	F	Cl	Total
EBS4-AltPlag1-1	68.44	0.22	19.26	0.00	1.22	0.02	0.35	0.02	0.00	1.64	3.98	6.92	0.02	0.02	102.10
EBS4-AltPlag1-2	61.37	0.34	24.68	0.00	1.18	0.01	0.40	0.00	0.02	3.49	4.31	3.94	0.00	0.03	99.78
AVE	**64.90**	**0.28**	**21.97**	**0.00**	**1.20**	**0.01**	**0.37**	**0.01**	**0.01**	**2.57**	**4.15**	**5.43**	**0.01**	**0.03**	**100.94**
EBS9-Ab1 (vfg)	68.43	0.05	20.33	0.00	0.36	0.00	0.06	0.00	0.00	0.11	11.19	0.11	0.06	0.01	100.68
EBS9-Pl1-1	61.98	0.00	23.57	0.00	0.28	0.00	0.01	0.00	0.00	5.27	8.01	0.99	0.00	0.00	100.12
AVE	**65.20**	**0.03**	**21.95**	**0.00**	**0.32**	**0.00**	**0.04**	**0.00**	**0.00**	**2.69**	**9.60**	**0.55**	**0.03**	**0.01**	**100.40**
EBS10-Pl-1	63.53	0.02	22.85	0.00	0.26	0.02	0.00	0.00	0.01	4.46	8.36	1.00	0.00	0.00	100.51
EBS10-Pl-2	60.50	0.00	24.31	0.00	0.30	0.02	0.00	0.00	0.00	6.22	7.41	0.77	0.00	0.00	99.53
EBS10-Pl2-1	60.52	0.03	24.57	0.01	0.26	0.00	0.01	0.02	0.02	6.00	7.44	0.86	0.00	0.00	99.74
EBS10-Pl-4	64.03	0.00	22.66	0.01	0.27	0.02	0.00	0.00	0.00	3.53	7.95	1.17	0.09	0.00	99.70
AVE	**62.15**	**0.01**	**23.60**	**0.00**	**0.27**	**0.02**	**0.01**	**0.00**	**0.01**	**5.05**	**7.79**	**0.95**	**0.02**	**0.00**	**99.87**
STD DEV	**1.90**	**0.01**	**0.98**	**0.01**	**0.02**	**0.01**	**0.00**	**0.01**	**0.01**	**1.28**	**0.46**	**0.18**	**0.04**	**0.00**	**0.44**
EBS11-Pl-1	60.70	0.02	24.40	0.00	0.23	0.00	0.01	0.00	0.02	6.79	7.44	0.74	0.00	0.00	100.35
EBS11-Pl-2	62.65	0.02	22.87	0.00	0.22	0.01	0.00	0.01	0.02	4.45	8.37	1.00	0.00	0.00	99.62
AVE	**61.68**	**0.02**	**23.63**	**0.00**	**0.23**	**0.00**	**0.01**	**0.01**	**0.02**	**5.62**	**7.90**	**0.87**	**0.00**	**0.00**	**99.98**
STD DEV	**1.38**	**0.00**	**1.08**	**0.00**	**0.01**	**0.00**	**0.00**	**0.01**	**0.01**	**1.65**	**0.66**	**0.18**	**0.00**	**0.00**	**0.51**
EBS12-Pl-1	59.53	0.00	26.09	0.00	0.24	0.00	0.00	0.00	0.03	8.05	6.90	0.57	0.01	0.00	101.42
EBS12-Pl-1	60.59	0.00	26.57	0.00	0.27	0.00	0.01	0.02	0.00	7.92	7.16	0.59	0.07	0.01	103.18
EBS12-Pl-2	62.17	0.00	23.18	0.02	0.23	0.00	0.00	0.01	0.01	4.88	8.04	1.01	0.02	0.01	99.57
AVE	**60.76**	**0.00**	**25.28**	**0.01**	**0.25**	**0.00**	**0.00**	**0.01**	**0.01**	**6.95**	**7.37**	**0.72**	**0.03**	**0.00**	**101.39**
STD DEV	**1.33**	**0.00**	**1.83**	**0.01**	**0.02**	**0.00**	**0.00**	**0.01**	**0.02**	**1.79**	**0.60**	**0.25**	**0.03**	**0.00**	**1.80**

Table B6. EMP analyses from plagioclase.

	SiO_2	TiO_2	Al_2O_3	Cr_2O_3	FeO*	MnO	MgO	NiO	ZnO	CaO	Na_2O	K_2O	F	Cl	Total
EBS7-Chl1-1	34.88	0.05	15.55	0.00	33.78	0.12	1.62	0.01	0.05	0.08	0.82	0.02	0.00	0.06	87.02
EBS7-Chl1-2	34.32	0.07	15.08	0.02	33.58	0.11	1.64	0.00	0.00	0.07	0.50	0.01	0.00	0.11	85.48
EBS7-Chl1-3	32.39	0.05	14.80	0.00	37.47	0.13	1.60	0.00	0.01	0.07	1.01	0.04	0.00	0.05	87.60
AVE	**33.86**	**0.05**	**15.14**	**0.01**	**34.94**	**0.12**	**1.62**	**0.01**	**0.02**	**0.07**	**0.77**	**0.02**	**0.00**	**0.07**	**86.70**
STD DEV	**1.30**	**0.01**	**0.38**	**0.01**	**2.19**	**0.01**	**0.02**	**0.01**	**0.03**	**0.00**	**0.26**	**0.02**	**0.00**	**0.03**	**1.09**
EBS9-Chl1-1	35.06	0.05	14.06	0.00	32.78	0.08	1.73	0.00	0.00	0.55	3.14	0.09	0.00	0.01	87.56
EBS9-Chl2-1	37.02	0.06	15.10	0.00	33.26	0.13	1.78	0.00	0.01	0.64	1.50	0.13	0.00	0.00	89.62
EBS9-Chl2-2	36.83	0.02	15.08	0.00	33.31	0.10	1.84	0.00	0.06	0.69	0.98	0.08	0.04	0.00	89.01
AVE	**36.30**	**0.04**	**14.75**	**0.00**	**33.11**	**0.10**	**1.78**	**0.00**	**0.02**	**0.63**	**1.87**	**0.10**	**0.01**	**0.01**	**88.73**
STD DEV	**1.08**	**0.02**	**0.59**	**0.00**	**0.29**	**0.02**	**0.05**	**0.00**	**0.03**	**0.07**	**1.12**	**0.03**	**0.02**	**0.00**	**1.06**
EBS11-Chl1	38.39	0.08	13.56	0.01	31.34	0.11	3.40	0.02	0.01	1.18	2.30	0.13	0.00	0.01	90.55
EBS11-Chl2	36.96	0.02	12.60	0.00	30.04	0.06	3.35	0.02	0.03	1.07	2.22	0.14	0.00	0.09	86.58
AVE	**37.68**	**0.05**	**13.08**	**0.01**	**30.69**	**0.09**	**3.37**	**0.02**	**0.02**	**1.13**	**2.26**	**0.13**	**0.00**	**0.05**	**88.57**

Table B7. EMP data on chlorite associated with ZVI from redox buffer.

Wt. %	Si	P	V	Cr	Mn	Fe	Co	Ni	Cu	Mo	Total
Transect 1a, inward from upper edge: 20 mm spacing											
EBS10-T1-1	0.36	0.05	0.05	16.37	1.81	65.30	0.18	11.17	0.57	2.26	98.13
EBS10-T1-2	0.37	0.04	0.08	16.97	1.81	65.45	0.17	11.29	0.50	2.23	98.90
EBS10-T1-3	0.38	0.04	0.08	16.96	1.81	65.34	0.18	11.73	0.58	2.17	99.26
EBS10-T1-4	0.38	0.04	0.07	16.82	1.75	65.40	0.20	11.72	0.61	2.20	99.18
EBS10-T1-5	0.37	0.03	0.05	16.89	1.69	65.24	0.18	11.39	0.53	2.13	98.49
AVE	**0.37**	**0.04**	**0.07**	**16.80**	**1.77**	**65.34**	**0.18**	**11.46**	**0.56**	**2.20**	**98.79**
STD DEV	**0.01**	**0.01**	**0.01**	**0.25**	**0.05**	**0.08**	**0.01**	**0.25**	**0.05**	**0.05**	**0.48**
Transect 1b, inward from lower edge: 20 mm spacing											
EBS10-T1b-1	0.36	0.04	0.07	16.85	1.81	65.69	0.17	11.32	0.57	2.23	99.11
EBS10-T1b-2	0.37	0.06	0.08	16.87	1.71	66.15	0.15	11.34	0.55	2.08	99.35
EBS10-T1b-3	0.37	0.06	0.10	17.00	1.82	65.87	0.17	11.36	0.54	1.98	99.26
EBS10-T1b-4	0.35	0.03	0.09	16.98	1.76	66.07	0.20	11.39	0.55	2.07	99.49
EBS10-T1b-5	0.35	0.04	0.06	16.83	1.73	65.82	0.21	11.51	0.54	2.13	99.23
AVE	**0.36**	**0.05**	**0.08**	**16.90**	**1.77**	**65.92**	**0.18**	**11.38**	**0.55**	**2.10**	**99.29**
Std Dev	**0.01**	**0.01**	**0.02**	**0.08**	**0.05**	**0.19**	**0.02**	**0.07**	**0.01**	**0.09**	**0.14**

Table B8. EMP data from 316SS associated with EBS-10.

	Si	P	V	Cr	Mn	Fe	Co	Ni	Cu	Mo	Total
Transect 2a, inward from upper edge: 20 mm spacing											
EBS10-T2-1	0.38	0.02	0.10	16.69	1.69	65.66	0.17	11.51	0.55	2.24	99.00
EBS10-T2-2	0.36	0.01	0.10	17.19	1.79	66.63	0.21	11.25	0.53	1.95	100.02
EBS10-T2-3	0.37	0.06	0.07	16.97	1.67	66.18	0.19	11.75	0.52	2.03	99.82
EBS10-T2-4	0.38	0.07	0.08	17.08	1.91	65.61	0.21	11.37	0.62	2.00	99.32
EBS10-T2-5	0.39	0.04	0.05	17.40	1.77	66.33	0.22	11.48	0.48	2.04	100.21
AVE	**0.38**	**0.04**	**0.08**	**17.07**	**1.77**	**66.08**	**0.20**	**11.47**	**0.54**	**2.05**	**99.67**
Std Dev	**0.01**	**0.03**	**0.02**	**0.27**	**0.09**	**0.44**	**0.02**	**0.18**	**0.05**	**0.11**	**0.50**
Transect 2b, inward from lower edge: 20 mm spacing											
EBS10-T2b-1	0.37	0.02	0.06	17.25	2.11	65.79	0.21	11.53	0.52	2.04	99.90
EBS10-T2b-2	0.37	0.02	0.06	17.22	1.72	65.87	0.20	11.72	0.58	1.97	99.73
EBS10-T2b-3	0.39	0.04	0.07	17.22	1.84	66.07	0.18	11.53	0.55	2.29	100.18
EBS10-T2b-4	0.38	0.02	0.10	17.59	1.79	66.33	0.19	11.27	0.53	2.29	100.49
EBS10-T2b-5	0.36	0.03	0.07	17.13	1.85	65.94	0.20	11.43	0.50	2.11	99.60
AVE	**0.37**	**0.03**	**0.07**	**17.28**	**1.86**	**66.00**	**0.20**	**11.50**	**0.54**	**2.14**	**99.98**
Std Dev	**0.01**	**0.01**	**0.02**	**0.18**	**0.15**	**0.21**	**0.01**	**0.16**	**0.03**	**0.14**	**0.36**

Table B9. EMP data from 316SS associated with EBS-10.

	Si	P	V	Cr	Mn	Fe	Co	Ni	Cu	Mo	Total
Transect 3a, inward from upper edge: 20 mm spacing											
EBS10-T3-1	0.43	0.05	0.09	17.34	1.70	63.24	0.21	11.26	0.52	2.26	97.11
EBS10-T3-2	0.38	0.05	0.09	17.86	1.87	65.62	0.20	11.45	0.47	2.24	100.24
EBS10-T3-3	0.37	0.03	0.08	17.96	1.95	66.06	0.21	11.28	0.50	2.11	100.55
EBS10-T3-4	0.38	0.04	0.06	17.70	1.81	65.69	0.19	11.59	0.52	2.17	100.14
EBS10-T3-5	0.37	0.03	0.08	17.68	1.81	65.74	0.17	11.79	0.59	2.10	100.37
EBS10-T3-6	0.37	0.03	0.06	17.73	1.76	66.33	0.21	11.51	0.56	2.16	100.73
EBS10-T3-7	0.39	0.05	0.08	17.96	1.86	65.71	0.24	11.30	0.52	2.21	100.31
EBS10-T3-8	0.37	0.02	0.09	17.65	1.82	66.20	0.18	11.69	0.58	2.09	100.70
EBS10-T3-9	0.37	0.03	0.05	18.30	1.76	66.27	0.19	11.04	0.45	2.28	100.76
EBS10-T3-10	0.39	0.01	0.11	17.86	1.86	66.14	0.20	11.76	0.54	2.26	101.13
AVE	**0.38**	**0.04**	**0.08**	**17.80**	**1.82**	**65.70**	**0.20**	**11.47**	**0.53**	**2.19**	**100.20**
Std Dev	**0.02**	**0.01**	**0.02**	**0.25**	**0.07**	**0.91**	**0.02**	**0.25**	**0.04**	**0.07**	**1.13**
Transect 3b, inward from lower edge: 20 mm spacing											
EBS10-T3b-1	0.37	0.04	0.09	18.36	1.83	66.33	0.19	11.21	0.59	2.23	101.24
EBS10-T3b-2	0.37	0.02	0.11	18.14	1.78	66.12	0.14	11.59	0.62	1.97	100.85
EBS10-T3b-3	0.37	0.03	0.09	18.08	1.82	66.06	0.20	11.61	0.56	2.23	101.06
EBS10-T3b-4	0.37	0.04	0.08	17.97	1.83	65.46	0.19	11.92	0.50	2.21	100.57
EBS10-T3b-5	0.37	0.05	0.09	18.03	1.88	65.76	0.18	11.89	0.56	2.15	100.95
EBS10-T3b-6	0.37	0.03	0.07	17.82	1.79	65.69	0.19	11.75	0.52	2.15	100.37
EBS10-T3b-7	0.37	0.02	0.06	18.20	1.77	66.14	0.21	11.32	0.62	2.06	100.77
EBS10-T3b-8	0.38	0.03	0.07	18.04	1.83	66.13	0.18	11.64	0.54	2.17	101.02
EBS10-T3b-9	0.39	0.05	0.10	17.95	1.75	65.60	0.22	11.83	0.57	2.19	100.66
EBS10-T3b-10	0.37	0.03	0.06	17.93	1.64	65.87	0.20	11.54	0.58	2.26	100.48
AVE	**0.37**	**0.03**	**0.08**	**18.05**	**1.79**	**65.92**	**0.19**	**11.63**	**0.57**	**2.16**	**100.80**
Std Dev	**0.01**	**0.01**	**0.02**	**0.15**	**0.07**	**0.28**	**0.02**	**0.23**	**0.04**	**0.09**	**0.28**

Table B10. EMP data from 316SS associated with EBS-10.

	Si	P	V	Cr	Mn	Fe	Co	Ni	Cu	Mo	Total
Points along center line of metals											
EBS10-Cent1-1	0.34	0.04	0.04	16.63	1.67	66.44	0.18	11.11	0.56	2.09	99.09
EBS10-Cent1-2	0.34	0.05	0.07	16.75	1.68	66.74	0.20	11.00	0.52	2.13	99.49
EBS10-Cent1-3	0.35	0.02	0.05	16.81	1.63	66.59	0.25	11.02	0.50	1.99	99.22
EBS10-Cent1-4	0.35	0.04	0.11	17.23	1.63	66.91	0.22	10.57	0.48	2.25	99.78
EBS10-Cent1-5	0.35	0.05	0.08	17.00	1.62	66.75	0.15	10.59	0.49	2.17	99.24
EBS10-Cent2-1	0.35	0.05	0.10	17.08	1.74	66.28	0.19	11.26	0.49	1.88	99.42
EBS10-Cent2-2	0.35	0.05	0.06	17.70	1.70	66.19	0.20	10.48	0.47	2.23	99.42
EBS10-Cent2-3	0.36	0.06	0.09	16.90	1.86	66.19	0.20	11.14	0.44	1.93	99.17
EBS10-Cent2-4	0.38	0.06	0.11	17.37	1.82	65.80	0.19	11.82	0.61	2.09	100.24
EBS10-Cent2-5	0.36	0.03	0.08	17.28	1.89	65.67	0.20	11.68	0.55	2.10	99.84
EBS10-Cent3-1	0.41	0.05	0.08	18.14	1.99	63.88	0.22	12.61	0.54	2.46	100.38
EBS10-Cent3-2	0.42	0.04	0.09	18.46	2.02	64.02	0.20	12.16	0.65	2.40	100.46
EBS10-Cent3-3	0.38	0.03	0.08	18.15	1.82	64.87	0.24	11.94	0.61	2.08	100.20
EBS10-Cent3-4	0.97	0.05	0.10	17.71	2.31	64.23	0.16	12.13	0.59	2.34	100.60
EBS10-Cent3-5	0.41	0.06	0.05	18.21	1.81	65.40	0.20	12.00	0.59	2.39	101.12
Average	**0.41**	**0.04**	**0.08**	**17.43**	**1.81**	**65.73**	**0.20**	**11.43**	**0.54**	**2.17**	**99.84**
Std Dev	**0.16**	**0.01**	**0.02**	**0.60**	**0.19**	**1.03**	**0.03**	**0.66**	**0.06**	**0.17**	**0.62**

Table B11. EMP data from 316SS associated with EBS-10.

	Si	P	V	Cr	Mn	Fe	Co	Ni	Cu	Mo	Total
Transect 1a, inward from upper edge: 20 mm spacing											
EBS5-T1-1	0.49	0.02	0.02	18.80	1.79	69.89	0.16	8.76	0.21	0.16	100.32
EBS5-T1-2	0.50	0.02	0.04	19.28	1.86	69.86	0.13	8.48	0.24	0.14	100.55
EBS5-T1-3	0.50	0.02	0.07	19.19	1.82	69.92	0.11	8.40	0.26	0.11	100.39
EBS5-T1-4	0.51	0.02	0.07	19.16	1.79	69.97	0.11	8.61	0.23	0.05	100.52
EBS5-T1-5	0.49	0.04	0.07	19.32	1.88	70.26	0.10	8.46	0.20	0.19	101.00
AVE	**0.50**	**0.02**	**0.05**	**19.15**	**1.83**	**69.98**	**0.12**	**8.54**	**0.23**	**0.13**	**100.56**
Std Dev	**0.01**	**0.01**	**0.02**	**0.21**	**0.04**	**0.16**	**0.02**	**0.14**	**0.02**	**0.05**	**0.27**
Transect 1b, inward from lower edge: 20 mm spacing											
EBS5-T1b-1	0.49	0.04	0.05	19.33	1.98	69.96	0.11	8.60	0.24	0.12	100.92
EBS5-T1b-2	0.50	0.03	0.03	19.27	1.90	70.28	0.17	8.57	0.24	0.12	101.11
EBS5-T1b-3	0.50	0.04	0.05	19.25	1.80	70.45	0.13	8.26	0.27	0.12	100.89
EBS5-T1b-4	0.51	0.04	0.07	19.24	1.84	70.13	0.12	8.74	0.26	0.12	101.07
EBS5-T1b-5	0.51	0.02	0.04	18.99	1.89	70.00	0.12	8.54	0.26	0.12	100.49
AVE	**0.50**	**0.03**	**0.05**	**19.22**	**1.88**	**70.16**	**0.13**	**8.54**	**0.25**	**0.12**	**100.90**
Std Dev	**0.01**	**0.01**	**0.02**	**0.13**	**0.07**	**0.20**	**0.02**	**0.17**	**0.02**	**0.00**	**0.25**

Table B12. EMP data from 304SS associated with EBS-5.

	Si	P	V	Cr	Mn	Fe	Co	Ni	Cu	Mo	Total
Transect 2a, inward from upper edge: 20 mm spacing											
EBS5-T2-1	0.51	0.04	0.06	19.27	1.84	70.17	0.12	8.26	0.24	0.07	100.56
EBS5-T2-2	0.50	0.01	0.07	19.61	2.06	69.63	0.17	8.80	0.24	0.15	101.23
EBS5-T2-3	0.51	0.02	0.03	19.24	1.80	70.77	0.13	8.57	0.22	0.17	101.47
EBS5-T2-4	0.52	0.02	0.04	19.45	1.94	70.51	0.13	8.35	0.25	0.17	101.37
EBS5-T2-5	0.51	0.04	0.07	19.34	1.87	70.45	0.11	8.68	0.25	0.12	101.43
AVE	**0.51**	**0.03**	**0.05**	**19.38**	**1.90**	**70.30**	**0.13**	**8.53**	**0.24**	**0.13**	**101.21**
Std Dev	**0.01**	**0.01**	**0.02**	**0.15**	**0.10**	**0.44**	**0.02**	**0.23**	**0.01**	**0.04**	**0.38**
Transect 2b, inward from lower edge: 20 mm spacing											
EBS10-T3-1	0.43	0.05	0.09	17.34	1.70	63.24	0.21	11.26	0.52	2.26	97.11
EBS10-T3-2	0.38	0.05	0.09	17.86	1.87	65.62	0.20	11.45	0.47	2.24	100.24
EBS10-T3-3	0.37	0.03	0.08	17.96	1.95	66.06	0.21	11.28	0.50	2.11	100.55
EBS10-T3-4	0.38	0.04	0.06	17.70	1.81	65.69	0.19	11.59	0.52	2.17	100.14
EBS10-T3-5	0.37	0.03	0.08	17.68	1.81	65.74	0.17	11.79	0.59	2.10	100.37
EBS10-T3-6	0.37	0.03	0.06	17.73	1.76	66.33	0.21	11.51	0.56	2.16	100.73
EBS10-T3-7	0.39	0.05	0.08	17.96	1.86	65.71	0.24	11.30	0.52	2.21	100.31
EBS10-T3-8	0.37	0.02	0.09	17.65	1.82	66.20	0.18	11.69	0.58	2.09	100.70
EBS10-T3-9	0.37	0.03	0.05	18.30	1.76	66.27	0.19	11.04	0.45	2.28	100.76
EBS10-T3-10	0.39	0.01	0.11	17.86	1.86	66.14	0.20	11.76	0.54	2.26	101.13
AVE	**0.38**	**0.04**	**0.08**	**17.80**	**1.82**	**65.70**	**0.20**	**11.47**	**0.53**	**2.19**	**100.20**
Std Dev	**0.02**	**0.01**	**0.02**	**0.25**	**0.07**	**0.91**	**0.02**	**0.25**	**0.04**	**0.07**	**1.13**

Table B13. EMP data from 304SS associated with EBS-5.

	Si	P	V	Cr	Mn	Fe	Co	Ni	Cu	Mo	Total
Transect 3a, inward from upper edge: 20 mm spacing											
EBS5-T3-1	0.46	0.05	0.02	18.43	1.79	68.49	0.12	8.38	0.26	0.17	98.17
EBS5-T3-2	0.50	0.02	0.05	19.05	1.85	69.04	0.12	8.65	0.21	0.23	99.71
EBS5-T3-3	0.50	0.01	0.03	18.92	1.90	68.87	0.11	8.33	0.24	0.20	99.11
EBS5-T3-4	0.49	0.02	0.02	18.97	1.84	69.16	0.12	8.50	0.21	0.24	99.57
EBS5-T3-5	0.49	0.04	0.01	19.12	1.77	69.07	0.15	8.32	0.22	0.11	99.30
EBS5-T3-6	0.51	0.02	0.05	19.21	1.95	69.81	0.15	8.45	0.23	0.21	100.59
EBS5-T3-7	0.50	0.02	0.07	18.80	1.84	69.16	0.13	8.60	0.25	0.11	99.48
EBS5-T3-8	0.49	0.02	0.06	18.63	1.82	69.11	0.13	8.42	0.22	0.20	99.09
EBS5-T3-9	0.49	0.03	0.07	18.83	1.79	68.78	0.15	8.43	0.23	0.12	98.92
EBS5-T3-10	0.49	0.02	0.00	18.83	1.86	68.65	0.13	8.53	0.26	0.22	99.00
AVE	**0.49**	**0.03**	**0.04**	**18.88**	**1.84**	**69.01**	**0.13**	**8.46**	**0.23**	**0.18**	**99.30**
Std Dev	**0.01**	**0.01**	**0.02**	**0.23**	**0.05**	**0.36**	**0.01**	**0.11**	**0.02**	**0.05**	**0.63**
Transect 3b, inward from lower edge: 20 mm spacing											
EBS5-T3b-1	0.50	0.02	0.04	19.14	1.82	69.66	0.13	8.33	0.26	0.19	100.09
EBS5-T3b-2	0.50	0.02	0.04	19.14	1.89	69.01	0.16	8.52	0.28	0.11	99.67
EBS5-T3b-3	0.49	0.03	0.04	19.25	1.89	68.82	0.13	8.23	0.23	0.13	99.23
EBS5-T3b-4	0.49	0.02	0.07	18.89	2.02	68.90	0.09	8.32	0.20	0.10	99.11
EBS5-T3b-5	0.50	0.02	0.02	18.84	1.87	69.28	0.13	8.49	0.21	0.12	99.47
EBS5-T3b-6	0.49	0.03	0.04	19.01	1.86	69.40	0.09	8.49	0.26	0.15	99.81
EBS5-T3b-7	0.48	0.01	0.03	18.98	1.81	69.47	0.11	8.39	0.23	0.17	99.68
EBS5-T3b-8	0.49	0.03	0.05	18.88	1.81	69.04	0.17	8.67	0.24	0.08	99.46
EBS5-T3b-9	0.49	0.04	0.06	18.76	1.96	69.55	0.07	8.47	0.18	0.11	99.69
EBS5-T3b-10	0.51	0.00	0.04	18.89	1.88	69.82	0.14	8.60	0.28	0.11	100.26
AVE	**0.49**	**0.02**	**0.04**	**18.98**	**1.88**	**69.29**	**0.12**	**8.45**	**0.24**	**0.13**	**99.65**
Std Dev	**0.01**	**0.01**	**0.02**	**0.16**	**0.07**	**0.34**	**0.03**	**0.13**	**0.03**	**0.04**	**0.35**

Table B14. EMP data from 304SS associated with EBS-5.

	Si	P	V	Cr	Mn	Fe	Co	Ni	Cu	Mo	Total
Points along center line of metals											
EBS5-Cent1-1	0.50	0.04	0.07	19.31	1.84	70.08	0.09	8.50	0.21	0.16	100.82
EBS5-Cent1-2	0.50	0.04	0.04	19.23	1.83	70.22	0.11	8.50	0.27	0.08	100.82
EBS5-Cent1-3	0.54	0.01	0.03	19.11	1.90	69.24	0.13	9.25	0.26	0.10	100.59
EBS5-Cent1-4	0.50	0.04	0.05	19.35	1.80	70.03	0.13	8.57	0.26	0.17	100.90
EBS5-Cent1-5	0.52	0.01	0.05	19.26	1.86	69.59	0.07	8.84	0.24	0.07	100.52
EBS5-Cent2-1	0.52	0.03	0.05	19.46	2.05	69.49	0.11	8.92	0.24	0.16	101.03
EBS5-Cent2-2	0.52	0.01	0.04	19.37	2.00	69.89	0.10	9.05	0.28	0.16	101.41
EBS5-Cent2-3	0.54	0.04	0.07	19.32	1.86	70.42	0.11	8.98	0.30	0.13	101.75
EBS5-Cent2-4	0.53	0.03	0.05	19.37	1.97	69.86	0.09	9.30	0.29	0.13	101.62
EBS5-Cent2-5	0.53	0.06	0.05	19.30	1.98	70.39	0.12	8.98	0.25	0.16	101.83
EBS5-Cent3-1	0.49	0.02	0.06	19.04	1.74	68.96	0.13	8.57	0.26	0.10	99.37
EBS5-Cent3-2	0.51	0.00	0.07	18.91	1.81	68.45	0.10	8.90	0.23	0.22	99.20
EBS5-Cent3-3	0.50	0.03	0.05	19.25	1.94	70.58	0.16	8.65	0.24	0.23	101.62
EBS5-Cent3-4	0.49	0.01	0.02	18.75	1.85	68.61	0.11	8.64	0.23	0.15	98.86
EBS5-Cent3-5	0.51	0.04	0.05	19.00	1.85	68.43	0.14	8.61	0.20	0.17	99.00
Average	**0.51**	**0.03**	**0.05**	**19.20**	**1.88**	**69.62**	**0.11**	**8.82**	**0.25**	**0.15**	**100.62**
Std Dev	0.02	0.02	0.01	0.20	0.08	0.73	0.02	0.26	0.03	0.05	1.04

Table B15. EMP data from 304SS associated with EBS-5.

	SiO_2	TiO_2	Al_2O_3	Cr_2O_3	FeO*	MnO	MgO	NiO	ZnO	CaO	Na_2O	K_2O	F	Cl	O=F	O=Cl	Total
Low-Iron Phase (Montmorillonite)																	
EBS10-Sil-29	50.80	0.08	19.64	0.11	4.21	0.04	1.17	0.05	0.00	0.60	0.36	0.52	0.09	0.18	-0.04	-0.04	77.78
EBS10-Sil-30	45.77	0.12	17.38	0.14	4.67	0.06	1.04	0.05	0.00	0.69	0.47	0.51	0.12	0.22	-0.05	-0.05	71.14
EBS10-Sil-32	61.29	0.01	11.76	0.35	3.26	0.05	0.46	0.03	0.00	1.89	0.63	0.22	0.06	0.13	-0.03	-0.03	80.08
EBS10-Sil-33	64.44	0.00	17.54	0.30	2.29	0.04	0.24	0.01	0.00	1.05	3.23	0.01	0.12	0.06	-0.05	-0.01	89.28
Average	**55.57**	**0.05**	**16.58**	**0.23**	**3.61**	**0.05**	**0.73**	**0.04**	**0.00**	**1.06**	**1.17**	**0.31**	**0.10**	**0.15**	**-0.04**	**-0.03**	**79.57**
Std Dev	**8.76**	**0.06**	**3.37**	**0.12**	**1.05**	**0.01**	**0.45**	**0.02**	**0.00**	**0.59**	**1.38**	**0.25**	**0.03**	**0.07**	**0.01**	**0.02**	**7.50**
High-Iron Phase (Saponite)																	
EBS10-Sil-7	28.30	0.07	17.74	1.08	28.06	0.37	3.45	0.38	0.02	1.08	0.70	0.04	0.12	0.27	-0.05	-0.06	81.57
EBS10-Sil-8	22.52	0.08	18.01	1.20	26.78	0.35	3.18	1.42	0.00	0.84	0.47	0.06	0.11	0.22	-0.05	-0.05	75.14
EBS10-Sil-9	28.14	0.08	17.39	1.06	27.03	0.40	3.22	0.37	0.02	1.17	0.82	0.06	0.23	0.32	-0.10	-0.07	80.12
EBS10-Sil-10	28.50	0.07	17.73	0.98	27.89	0.38	3.18	1.25	0.00	1.17	0.85	0.05	0.08	0.25	-0.03	-0.06	82.31
EBS10-Sil-11	27.97	0.08	15.26	0.94	27.38	0.35	2.67	0.99	0.00	1.11	0.92	0.07	0.00	0.29	0.00	-0.06	77.97
EBS10-Sil-12	27.07	0.06	17.20	1.24	28.48	0.41	3.09	0.66	0.01	1.01	0.69	0.04	0.15	0.19	-0.06	-0.04	80.20
EBS10-Sil-13	31.92	0.09	16.29	1.15	28.96	0.37	3.20	0.61	0.00	1.24	1.05	0.06	0.08	0.27	-0.03	-0.06	85.20
EBS10-Sil-14	29.67	0.07	16.67	0.73	27.98	0.39	3.18	0.31	0.00	1.04	0.92	0.07	0.00	0.25	0.00	-0.06	81.23
EBS10-Sil-15	26.88	0.07	16.79	1.06	28.35	0.37	3.15	0.66	0.00	0.83	0.85	0.06	0.00	0.17	0.00	-0.04	79.20
EBS10-Sil-17	28.70	0.06	16.82	1.17	28.65	0.40	3.09	0.40	0.01	1.08	0.77	0.06	0.01	0.20	0.00	-0.04	81.38
EBS10-Sil-18	28.75	0.09	16.84	0.92	28.76	0.40	3.20	2.80	0.02	1.34	0.72	0.06	0.10	0.28	-0.04	-0.06	84.18
EBS10-Sil-19	29.98	0.08	17.63	0.92	27.90	0.43	3.03	0.70	0.02	1.03	0.90	0.06	0.07	0.26	-0.03	-0.06	82.92
EBS10-Sil-20	29.53	0.08	16.24	0.73	28.06	0.43	2.82	0.58	0.00	1.21	0.88	0.08	0.15	0.28	-0.06	-0.06	80.95
EBS10-Sil-25	32.89	0.09	15.65	0.38	23.31	0.30	3.23	0.23	0.00	1.28	1.10	0.23	0.14	0.40	-0.06	-0.09	79.10
EBS10-Sil-26	38.06	0.08	15.69	0.22	22.63	0.34	2.66	0.25	0.00	1.29	0.59	0.66	0.06	0.15	-0.02	-0.03	82.64
Average	**29.26**	**0.08**	**16.80**	**0.92**	**27.35**	**0.38**	**3.09**	**0.77**	**0.01**	**1.12**	**0.81**	**0.11**	**0.09**	**0.25**	**-0.04**	**-0.06**	**80.94**
Std Dev	**3.37**	**0.01**	**0.84**	**0.30**	**1.88**	**0.03**	**0.22**	**0.66**	**0.01**	**0.15**	**0.17**	**0.16**	**0.07**	**0.06**	**0.03**	**0.01**	**2.51**

Table B16. Fine-grained coatings on 316SS associated with EBS-10. Starting montmorillonite is residual from the surrounding bentonite material. Saponite is the corrosion product associated with the 316SS.

Label	SiO_2	TiO_2	Al_2O_3	Cr_2O_3	FeO*	MnO	MgO	NiO	ZnO	CaO	Na_2O	K_2O	F	Cl	O=F	O=Cl	Total
Low-Iron Phase (starting montmorillonite)																	
EBS5-Sil-1	53.24	0.12	16.53	0.09	5.64	0.04	2.00	0.14	0.01	1.11	0.34	0.59	0.13	0.04	-0.06	-0.01	79.95
EBS5-Sil-2	52.91	0.13	17.43	0.07	3.66	0.04	1.62	0.15	0.00	0.77	0.29	0.59	0.27	0.04	-0.11	-0.01	77.83
EBS5-Sil-3	54.33	0.08	17.14	0.09	3.63	0.03	1.68	0.15	0.03	0.68	0.36	0.61	0.02	0.04	-0.01	-0.01	78.85
EBS5-Sil-4	57.69	0.13	16.16	0.13	4.12	0.01	1.62	0.06	0.01	0.62	0.63	0.63	0.18	0.05	-0.08	-0.01	81.96
EBS5-Sil-5	60.13	0.12	14.90	0.12	3.25	0.02	1.45	0.06	0.00	0.69	0.71	0.82	0.05	0.05	-0.02	-0.01	82.32
EBS5-Sil-7	58.44	0.11	13.70	0.13	3.67	0.05	1.49	0.14	0.00	0.65	0.56	0.68	0.26	0.04	-0.11	-0.01	79.80
EBS5-Sil-8	63.84	0.00	7.32	0.54	7.70	0.12	1.48	0.33	0.02	0.66	0.33	0.15	0.19	0.03	-0.08	-0.01	82.63
EBS5-Sil-12	52.70	0.08	14.94	0.09	5.38	0.06	2.19	0.10	0.00	0.96	0.40	0.33	0.24	0.10	-0.10	-0.02	77.44
EBS5-Sil-14	62.14	0.08	14.63	0.38	5.85	0.03	2.11	0.12	0.00	0.84	0.63	0.40	0.25	0.14	-0.10	-0.03	87.46
EBS5-Sil-18	59.26	0.06	14.23	0.13	4.44	0.03	1.88	0.10	0.01	0.84	0.49	0.35	0.12	0.11	-0.05	-0.02	81.95
EBS5-Sil-19	62.40	0.06	12.58	0.16	3.19	0.02	1.39	0.10	0.03	0.71	0.42	0.42	0.08	0.08	-0.03	-0.02	81.61
EBS5-Sil-20	58.20	0.08	15.70	0.13	4.21	0.02	1.87	0.07	0.03	0.81	0.49	0.35	0.13	0.07	-0.06	-0.02	82.10
EBS5-Sil-22	63.02	0.05	14.42	0.20	4.75	0.04	1.35	0.11	0.00	0.64	0.76	1.21	0.12	0.03	-0.05	-0.01	86.66
EBS5-Sil-26	57.53	0.08	19.43	0.24	5.29	0.02	1.92	0.16	0.00	0.97	0.51	0.44	0.24	0.06	-0.10	-0.01	86.76
EBS5-Sil-30	65.94	0.05	10.02	0.07	2.34	0.00	1.21	0.05	0.00	0.54	0.53	0.33	0.19	0.11	-0.08	-0.02	81.26
Average	**59.16**	**0.08**	**13.98**	**0.15**	**4.23**	**0.03**	**1.63**	**0.11**	**0.01**	**0.72**	**0.51**	**0.49**	**0.15**	**0.07**	**-0.06**	**-0.02**	**81.25**
Std Dev	3.71	0.03	2.78	0.12	1.42	0.03	0.28	0.06	0.01	0.16	0.15	0.23	0.09	0.03	0.04	0.01	2.93
High-Iron Phase: Saponite																	
EBS5-Sil-23	46.02	0.08	12.59	0.08	18.93	0.20	2.87	0.23	0.00	1.14	0.90	0.15	0.10	0.04	-0.04	-0.01	83.26
EBS5-Sil-28	32.53	0.08	12.45	0.84	26.74	0.22	4.33	0.48	0.01	0.46	0.18	0.02	0.00	0.00	0.00	0.00	78.34
Average	**39.27**	**0.08**	**12.52**	**0.46**	**22.83**	**0.21**	**3.60**	**0.35**	**0.00**	**0.80**	**0.54**	**0.08**	**0.05**	**0.02**	**-0.02**	**0.00**	**80.80**

Table B17. Fine-grained coatings on 304SS associated with EBS-5. Starting montmorillonite is residual from the surrounding bentonite material. Saponite is the corrosion product associated with the 304SS.

	O	S	Cu	Total
High-Density Oxides				
EBS4-Ox1	10.02	0.00	89.63	99.65
EBS4-Ox2	10.25	0.01	89.75	100.01
EBS4-Ox3	10.07	0.00	89.70	99.77
EBS4-Ox4	10.30	0.02	89.87	100.19
EBS4-Ox5	10.16	0.00	89.51	99.67
EBS4-Ox6	11.21	0.00	90.21	101.42
EBS4-Ox11	11.24	0.01	89.61	100.86
EBS4-Ox12	10.47	0.00	90.22	100.69
EBS4-Ox13	10.51	0.00	90.41	100.92
Average	**10.47**	**0.01**	**89.88**	**100.35**
Std Dev	**0.46**	**0.01**	**0.32**	**0.64**
Low-Density Oxides				
EBS4-Ox7	22.57	0.03	69.61	92.21
EBS4-Ox8	21.63	0.02	70.62	92.27
EBS4-Ox9	19.54	0.08	72.34	91.95
EBS4-Ox10	19.01	0.09	73.89	92.99
Average	**20.69**	**0.05**	**71.62**	**92.36**
Std Dev	**1.69**	**0.03**	**1.89**	**0.45**
Sulfides				
EBS4-Sulf1	0.01	20.96	79.70	100.67
EBS4-Sulf2	0.00	20.49	80.02	100.51
EBS4-Sulf3	0.03	20.53	79.93	100.48
EBS4-Sulf4	0.01	20.76	79.61	100.38
EBS4-Sulf5	0.05	21.25	79.35	100.65
EBS4-Sulf6	0.08	22.47	77.44	99.99
EBS4-Sulf7	0.00	21.87	77.72	99.59
EBS4-Sulf8	0.00	21.41	78.75	100.16
EBS4-Sulf9	0.00	21.32	78.32	99.64
EBS4-Sulf10	0.00	22.59	76.98	99.57
Average	**0.02**	**21.36**	**78.78**	**100.16**
Std Dev	**0.03**	**0.74**	**1.11**	**0.44**

Table B18. EMP data from Cu corrosion products associated with EBS-4. Oxides are mostly likely related to oxidation of primary sulfide corrosion products between experiment end and analyses.

	O	S	Cu	Total
EBS11-sulf1	0.06	20.88	81.06	102.00
EBS11-sulf2	0.00	20.68	81.37	102.05
EBS11-sulf3	0.02	20.68	81.05	101.75
EBS11-sulf4	0.02	20.49	80.15	100.66
EBS11-sulf5	0.04	20.47	80.44	100.96
EBS11-sulf6	0.00	20.68	80.90	101.58
EBS11-sulf7	0.05	20.63	80.51	101.19
EBS11-sulf8	0.00	20.74	80.60	101.34
EBS11-sulf9	0.00	20.80	80.22	101.02
EBS11-sulf10	0.09	20.94	80.56	101.58
EBS11-sulf11	0.05	20.69	79.81	100.54
EBS11-sulf12	0.03	20.81	80.54	101.38
EBS11-sulf13	0.06	20.79	81.38	102.23
EBS11-sulf14	0.00	20.70	80.73	101.42
EBS11-sulf15	0.10	20.32	80.64	101.06
EBS11-sulf16	0.00	20.86	80.63	101.49
EBS11-sulf17	0.00	20.68	80.86	101.54
EBS11-sulf18	0.06	20.71	80.91	101.68
EBS11-sulf19	0.07	20.74	80.89	101.69
EBS11-sulf20	0.07	20.78	81.13	101.98
Average	**0.04**	**20.70**	**80.72**	**101.46**
Std Dev	**0.03**	**0.15**	**0.40**	**0.45**

Table B19. EMP data from Cu corrosion products associated with EBS-11.

Appendix C:
Solution Chemistry

All data are presented as mg/L, unless otherwise as noted.

Lab ID	13/00 UF	13/01 UF	13/02 UF	13/03 UF	13/04 UF	13/05 UF	13/06 UF	13/07 UF	13/08 UF	13/09 UF	13/10 UF	13/11 UF	13/12 UF
Date Sampled	9/17/2013	9/18/2013	10/3/2013	10/24/2013	11/14/2013	12/5/2013	12/18/2013	1/6/2014	2/3/2014	2/14/2014	2/24/2014	3/13/2014	3/20/2014
Time, hours	0	24	386	864	1369	1872	2184	2644	3319	3576	3816	4224	4392
Temperature, °C	25	300	299	300	300	300	300	300	221	221	221	114	114
pH	11	6.06	5.91	5.97	5.83	5.90	5.75	5.78	5.99	5.92	5.96	6.48	6.56
Al	<0.02	0.51(0)	0.27(1)	0.78(1)	0.41(0)	0.02(0)	0.02(0)	0.09(0)	0.29(0)	0.36(0)	0.33(0)	0.08(0)	0.07(0)
B	0.28(1)	4(0)	7(0)	7(0)	7(0)	10(0)	10(0)	7(0)	7(0)	7(0)	7(0)	6(0)	6(0)
Ba	0.04(0)	<0.02	0.04(0)	0.03(0)	0.06(0)	<0.02	<0.02	<0.02	0.02(0)	0.03(0)	0.03(0)	0.06(0)	0.06(0)
Ca	61(1)	0.8(1)	2.1(1)	2.6(1)	2.5(1)	5.7(1)	2.6(1)	1.3(1)	4.6(1)	4.3(1)	4.0(1)	3.4(2)	3.6(2)
Cl	882	895	867	905	859	851	840	830	717	702	682	605	612
Cr	<0.02	<0.02	<0.02	<0.02	<0.02	<0.02	<0.02	<0.02	<0.02	<0.02	<0.02	<0.02	<0.02
Fe	<0.2	<0.2	<0.2	<0.2	<0.2	<0.2	<0.2	<0.2	<0.2	<0.2	<0.2	<0.2	<0.2
K	559(8)	275(3)	57(1)	55(1)	56(1)	68(1)	68(0)	45(0)	51(0)	48(0)	51(0)	45(0)	47(1)
Li	<0.02	0.13(0)	0.24(2)	0.28(1)	0.32(1)	0.37(2)	0.39(1)	0.28(0)	0.44(1)	0.46(1)	0.48(1)	0.45(0)	0.50(2)
Mg	<0.2	<0.2	<0.2	<0.2	0.25(2)	<0.2	<0.2	<0.2	<0.2	0.39(4)	0.39(3)	<0.2	0.43(4)
Mn	<0.02	<0.02	<0.02	<0.02	<0.02	<0.02	<0.02	<0.02	<0.02	<0.02	<0.02	0.02	0.02
Na	201(4)	430(4)	497(9)	564(6)	549(5)	670(6)	671(3)	475(4)	537(5)	497(2)	527(1)	506(2)	506(5)
Si	1(0)	190(2)	69(2)	47(1)	46(1)	51(0)	73(0)	72(1)	306(3)	296(5)	297(4)	192(1)	177(1)
SiO2	3(0)	407(4)	149(4)	101(2)	99(1)	109(1)	156(1)	155(2)	654(6)	634(11)	635(8)	411(2)	378(2)
SO4	53	20	68	81	75	70	65	60	156	151	142	129	123
Sr	0.06(0)	<0.02	<0.02	<0.02	0.02(0)	0.03(0)	0.02(0)	<0.02	0.06(0)	0.07(0)	0.07(0)	0.08(0)	0.08(0)
Ti	<0.04	<0.04	<0.04	<0.04	<0.04	<0.04	<0.04	<0.04	<0.04	<0.04	<0.04	<0.04	<0.04
Zn	<0.02	<0.02	0.03(1)	0.06(0)	0.10(0)	0.03(1)	0.03(1)	<0.02	<0.02	<0.02	<0.02	<0.02	<0.02
TDS	1759	2032	1647	1717	1649	1784	1813	1574	2128	2044	2049	1706	1677
Cation	26	26	23	26	26	31	31	22	25	23	25	23	23
Anion	26	26	26	28	26	26	25	25	24	23	22	20	20
Balance	0.00	0.00	-0.06	-0.02	-0.01	0.09	0.10	-0.06	0.02	0.00	0.04	0.08	0.08

Table C1. Unfiltered solution chemistry from EBS-13.

Lab ID	13/00 F	13/01 F	13/02 F	13/03 F	13/04 F	13/05 F	13/06 F	13/07 F	13/08 F	13/09 F	13/10 F	13/11 F	13/12 F
Date Sampled	9/18/2013	9/18/2013	10/3/2013	10/24/2013	11/14/2013	12/5/2013	12/18/2013	1/6/2014	2/3/2014	2/14/2014	2/24/2014	3/13/2014	3/20/2014
Time, hours	0	24	386	864	1369	1872	2184	2644	3319	3576	3816	4224	4392
Temperature, °C	25	300	299	300	300	300	300	300	221	221	221	114	114
pH	11	6.06	5.91	5.97	5.83	5.90	5.75	5.78	5.99	5.92	5.96	6.48	6.56
Al	<0.02	0.18(0)	<0.02	0.42(0)	0.45(1)	0.03(0)	0.42(0)	0.39(1)	0.28(0)	0.35(1)	0.34(0)	0.05(2)	0.04(0)
B	<0.04	4(0)	8(0)	7(0)	8(0)	11(0)	10(0)	7(0)	7(0)	7(0)	6(0)	6(0)	6(0)
Ba	<0.02	0.03(0)	0.05(0)	0.03(0)	<0.02	0.04(0)	0.04(0)	<0.02	0.02(0)	0.03(0)	0.03(0)	0.06(0)	0.07(0)
Ca	62(1)	2.0(1)	4.1(2)	2.5(1)	2.4(2)	3.7(1)	2.9(2)	1.8(0)	4.6(1)	4.2(1)	4.0(1)	3.9(2)	3.6(2)
Cr	<0.02	<0.02	<0.02	<0.02	<0.02	<0.02	<0.02	<0.02	<0.02	<0.02	<0.02	<0.02	<0.02
Fe	<0.2	<0.2	<0.2	<0.2	<0.2	<0.2	<0.2	<0.2	<0.2	<0.2	<0.2	<0.2	<0.2
K	926(3)	281(6)	66(0)	56(0)	56(0)	75(1)	69(0)	81(1)	67(1)	48(1)	49(0)	44(0)	46(0)
Li	0.04(0)	0.16(1)	0.28(1)	0.28(1)	0.30(1)	0.41(1)	0.40(0)	0.59(1)	0.61(2)	0.44(0)	0.44(1)	0.44(1)	0.47(0)
Mg	<0.2	0.32(1)	<0.2	<0.2	<0.2	<0.2	<0.2	<0.2	<0.2	<0.2	<0.2	<0.2	<0.2
Mn	<0.02	<0.02	<0.02	<0.02	<0.02	<0.02	<0.02	<0.02	<0.02	<0.02	<0.02	0.02	0.02
Na	234(3)	451(6)	578(2)	552(7)	555(6)	721(6)	666(3)	638(3)	598(5)	494(7)	531(2)	504(5)	510(0)
Si	<0.2	110(2)	32(0)	38(1)	33(0)	55(0)	68(0)	78(2)	382(3)	303(3)	308(2)	191(1)	179(1)
SiO2	<0.4	235(4)	68(0)	80(2)	70(0)	118(1)	145(1)	166(4)	818(7)	649(7)	659(5)	409(3)	383(3)
Sr	0.08(0)	0.02(0)	0.02(0)	<0.02	<0.02	0.04(0)	0.02(0)	0.03(0)	0.08(0)	0.06(0)	0.06(0)	0.08(0)	0.08(0)
Ti	<0.04	<0.04	<0.04	<0.04	<0.04	<0.04	<0.04	<0.04	<0.04	<0.04	<0.04	<0.04	<0.04
Zn	<0.02	<0.02	0.03(2)	0.07(0)	<0.02	0.02(0)	0.06(1)	<0.02	<0.02	<0.02	<0.02	<0.02	<0.02
TDS	1222	974	724	698	692	929	894	895	1495	1203	1251	967	949
Cation	37	27	27	26	26	34	31	30	28	23	25	23	24
Anion	0	0	0	0	0	0	0	0	0	0	0	0	0
Balance	1.00	0.99	0.97	0.97	0.97	0.97	0.97	0.98	0.98	0.97	0.98	0.98	0.98

Table C2. Filtered solution chemistry from EBS-13.

Lab ID	14/00 UF	14/01 UF	14/02 UF	14/03 UF	14/04 UF
Date Sampled	11/26/2013	11/27/2013	12/6/2013	12/18/2013	1/6/2014
Time, hours	0	24	240	528	988
Temperature, °C	25	299	299	300	300
pH	7.50	4.59	5.39	4.88	4.96
Al	<0.05	<0.05	<0.05	<0.05	<0.05
B	0.1(0)	5(0)	6(0)	6(0)	7(0)
Ba	<0.05	0.18(0)	0.17(2)	0.16(0)	0.28(1)
Ca	426(6)	317(4)	496(6)	564(8)	546(4)
Cl	6470	6484	6538	6497	6518
Cr	<0.05	<0.05	<0.05	<0.05	<0.05
Fe	<0.5	<0.5	<0.5	<0.5	<0.5
K	225(3)	174(2)	106(1)	232(6)	202(1)
Li	<0.05	2(0)	6(0)	12(0)	7(0)
Mg	194(2)	8(0)	1(0)	1(0)	0.9(0)
Mn	<0.05	0.09(0)	0.17(0)	0.23(0)	0.29(0)
Na	3846(32)	3831(40)	3571(54)	3971(39)	3473(8)
Si	1(0)	84(2)	78(1)	63(2)	56(1)
SiO2	2(0)	181(5)	167(3)	135(4)	120(1)
SO4	988	<1	<1	<1	<1
Sr	0.16(0)	2.5(0)	1.5(0)	2.3(0)	2.1(0)
Ti	<0.1	<0.1	<0.1	<0.1	<0.1
Zn	<0.05	0.06(1)	0.08(0)	0.09(1)	0.09(1)
TDS	12153	11006	10892	11420	10877
Cation	208	186	182	206	183
Anion	201	181	183	181	182
Balance	0.02	0.01	0.00	0.06	0.00

Table C3. Unfiltered solution chemistry from EBS-14.

Lab ID	14/00 F	14/01 F	14/02 F	14/03 F	14/04 F
Date Sampled	11/27/2013	11/27/2013	12/6/2013	12/18/2013	1/6/2014
Reaction time, hours	17	24	233	521	977
Temperature	25	300	300	300	300
pH	7.50	4.59	5.39	4.88	4.96
Al	<0.05	<0.05	<0.05	<0.05	<0.05
B	0.2(0)	5(0)	6(0)	6(0)	6(0)
Ba	<0.05	0.21(2)	0.12(0)	0.23(1)	0.29(1)
Ca	441(4)	319(3)	507(7)	573(5)	590(17)
Cr	<0.05	<0.05	<0.05	<0.05	<0.05
Fe	<0.5	<0.5	<0.5	<0.5	<0.5
K	223(2)	176(0)	106(1)	225(4)	334(6)
Li	<0.05	2(0)	6(0)	11(0)	13(0)
Mg	193(3)	8(0)	1(0)	1(0)	1.3(1)
Mn	<0.05	0.09(0)	0.16(0)	0.22(0)	0.24(0)
Na	3781(17)	3835(11)	3581(36)	4056(19)	4065(28)
Si	1(0)	36(0)	41(1)	51(1)	47(1)
SiO2	1(0)	78(0)	87(1)	108(2)	100(3)
Sr	0.17(0)	2.5(0)	1.5(0)	2.4(0)	2.8(1)
Ti	<0.1	<0.1	<0.1	<0.1	<0.1
Zn	<0.05	0.11(1)	0.06(1)	0.08(1)	0.15(1)
TDS	4640	4426	4296	4984	5113
Cation	207	187	184	212	216
Anion	0	0	0	0	0
Balance	1.00	1.00	1.00	1.00	1.00

Table C4. Filtered solution chemistry from EBS-14.